Nonlinear dynamics and neural systems: synchronization and modeling

by

Mark Alan Kramer

BA (Oberlin College) 2001

A dissertation submitted in partial satisfaction of the

requirements for the degree of

Doctor of Philosophy

in

Applied Science and Technology

in the

GRADUATE DIVISION

of the

UNIVERSITY OF CALIFORNIA, BERKELEY

Committee in charge:
Professor Andrew J. Szeri, Chair
Professor Edgar Knobloch
Professor Robert T. Knight

Fall 2005

The dissertation of Mark Alan Kramer is approved:

Chair Date

Date

Date

University of California, Berkeley

Fall 2005

Nonlinear dynamics and neural systems: synchronization and modeling

Abstract

Nonlinear dynamics and neural systems: synchronization and modeling

by

Mark Alan Kramer

Doctor of Philosophy in Applied Science and Technology

University of California, Berkeley

Professor Andrew J. Szeri, Chair

We study the electrical activity of the human cortex in two ways. First, we state seven coupling measures to analyze electroencephalogram and electrocortiogram time series. We apply these measures to simulated and observed data, and we use the measures to deduce changes in coupling induced by auditory stimuli and produced by dementia. Second, we define a mathematical model of the spatially averaged, mean-field cortical electrical activity recorded by the electroencephalograph and electrocortiograph. We compare the model results with ictal electrocortical data collected from four human subjects, and we show that the observed and simulated results agree in two important ways. We use the model to develop three methods for controlling seizures through electrical stimulation and to suggest the physiological mechanisms — and points of leverage for therapies — of epilepsy.

Professor Andrew J. Szeri
Dissertation Committee Chair

Contents

Acknowledgments

Thank you to:

Andrew Szeri, Robert Knight, Edgar Knobloch, Donna Hudson, Maurice Cohen, Fen-Lei Chang, Heidi Kirsch, and Tom Ferree for their guidance, advice, and collaborations.

and to:

Erik Edwards, Maryam Soltani, Ryan Canolty, Joseph Brooks, Mike Kurylo, Beth Lopour, Brian Spears, Michael Calvisi, Russel Cole, Ben Gallup, Jon Iloreta, Su Chan Park, Jean Toilliez, Aaron Weiss, and Zachary Zibrat for many useful discussions and collaborations.

and to:

Cindy Moon for her careful reading of this manuscript.

Chapter 1

Introduction

The human cerebral cortex — the outer few millimeters of the brain — is thought to control behaviors unique to humans (such as language and abstract thinking.) It consists of over 10^{10} neurons and receives over 10^{14} synaptic connections [1]. These synaptic connections allow an important type of communication between neurons. Both local connections between two neighboring neurons (e.g., intracortical connections) and nonlocal connections between two distant neurons (e.g., corticocortical connections) occur. In each case the communication occurs through the transmission of electrical signals.

There exist many techniques for investigating this neuronal communication. A crude division of such studies separates the presynaptic and postsynaptic neurons. In considering the former, one may investigate how a presynaptic neuron generates an action potential, the propagation of this action potential along an axon, or the effect of the action potential on a synapse. In considering the postsynaptic neuron, one may determine the importance of dendritic spines, the geometry of the dendritic tree, or the integration of dendritic input. Additionally, one may study the interface between two neurons (e.g., the dynamics of neurotransmitters within the synaptic cleft.) These investigations may involve optical, chemical, magnetic, and nuclear imaging techniques. Here we consider electric potential recordings.

Electric potential recordings may be taken at the microscopic spatial scale between two synaptically connected neurons. Many such recordings have been performed to reveal important aspects of cortical communication [2]. Yet, such recordings from single neurons cannot capture the complete behavior of cortical electrical activity. To study the electrical activity of the entire cortex, one would need to record from every neuron. Clearly, such recordings — from over 10^{10} individual neurons — are infeasible.

The electroencephalograph and electrocortiograph provide two techniques for observing *mesoscopic* cortical elec-

trical activity. In these two methods an electrode on the scalp and cortical surface results in the electroencephalogram (EEG) and electrocortiogram (ECoG) time series, respectively. The advantages of recording this mesoscopic data, rather than microscopic single neuron recordings, are twofold. First, the EEG and ECoG recordings are noninvasive. To record from a single neuron, one might pierce the cortex *in vivo* with a microelectrode, thereby damaging cortical tissue. Electrodes for EEG or ECoG observations rest passively on the scalp or cortical surface, respectively, and do not penetrate the cortex. Second, the EEG and ECoG time series represent the summed electrical activity from millions of individual neurons [3]. Some researchers believe that neural populations (e.g., groups of 10^5 neighboring neurons organized into cortical macrocolumns) form the functional units of the cortex [4, 5]. The EEG and ECoG recordings — not the single unit recordings — can capture the electrical activity of these functional units.

Because the techniques are less invasive, recordings of mesoscopic cortical electrical activity are more common in humans than single-unit recordings. Yet, the analysis of the resulting EEG or ECoG data can be more difficult. To illustrate this, we first consider the example of cortical communication or coupling. At the microscopic spatial scale, one might hypothesize that two neurons communicate through a synaptic connection. To test this hypothesis one may stimulate the first neuron (with an current pulse, say) and record the resulting electrical activity of the second neuron. If the second neuron emits an action potential, then one may conclude that the two neurons are coupled. This coupling may not occur directly; the stimulation of the first neuron may excite an intermediate neuron (or group of neurons) that in turn excites the observed neuron. Moreover difficulties might arise in isolating and recording from individual neurons. Yet the analysis required to test whether two neurons are synaptically coupled is quite simple.

At the mesoscopic spatial scale one might hypothesize that two cortical regions — not individual neurons — communicate. As a hypothetical example, we consider two regions of the temporal lobe that communicate when a subject hears a particular sound (e.g., an auditory tone [6].) To investigate this we place two electrodes on the subject's scalp — one above each cortical region — and record the EEG as we present the subject with different images. An analysis of the resulting EEG time series may reveal that the data recorded at the two electrodes correlate whenever the subject hears a particular tone, say a chirp. To determine this correlation, we may employ a variety of different measures. For example, in the time domain, we may compute the cross-correlation, synchronization, or average mutual information between the two time series. In the frequency domain, we may compute the coherence, phase consistency, or Granger causality between the the two time series. Complications can arise in determining the measure appropriate for the data of interest. For example, in the analysis of the hypothetical EEG data, we may first decide that a frequency domain approach is appropriate. We must then determine how to perform the time domain to frequency domain conversion (e.g., should we use a Fourier transform or a Hilbert transform? [7]) and whether to window the data (e.g., should we use no windowing, a Hanning window, or a multitaper window? [8])

Having decided upon and calculated a particular frequency domain measure, we then interpret the results. Perhaps we hypothesize that the increased coupling occurs in the γ frequency band ($\sim$ 40 Hz to $\sim$ 80 Hz.) Because we record scalp EEG data, we expect to detect only weak power in the γ-band. Therefore, to enhance the γ-band effect, we might average the frequency domain result that follows stimulus onset (i.e., the auditory chirp) over multiple trials. Or, we might compare the γ-band effect to a baseline of γ-band activity recorded following another (or no) stimulus. In any case, the interpretation of the coupling result is rarely simple. Moreover increased coupling between two EEG time series is only suggestive of increased communication between two cortical regions. For example, in the hypothetical EEG experiment, the two cortical regions may form no synaptic connections yet show increased coupling if each becomes activated by the same (perhaps subcortical) region. For these reasons, we find the analysis of coupling in EEG (and ECoG) data more difficult than between single neurons. Yet, coupling between mesoscopic cortical regions is of often interest and such analyses are frequently performed.

The difficulties of interpreting mesoscopic data are not limited to the coupling measures. Perhaps even more challenging is a physiological interpretation of EEG and ECoG data. For example, in the hypothetical EEG experiment, we may find an increased coupling between the two regions of the frontal lobe. We may also know (from anatomical evidence, say) that the two cortical regions communicate directly and not through an intermediate source. We may then ask: what physiological changes result in the increased coupling? Perhaps an increase occurs in the synaptic transmission between the cortical regions due to a more robust propagation of action potentials. Or, perhaps the cortical regions both become more excitable and more susceptible to synaptic input. To determine what physiological changes result in increased coupling, we may consider performing invasive experiments, for example injecting chemicals into the cortex or removing a transmission pathway. Of course such experiments are not permissible in human subjects. Instead, we construct a mathematical model to relate observed EEG and ECoG data with cortical physiology.

At the microscopic spatial scale, accurate mathematical models exist that describe the electrical activity of individual neurons (e.g., for CA3 hippocampal pyramidal neurons [9].) To describe the mesoscopic electrical activity recorded at a scalp or cortical electrode, we might attempt to simulate the behavior of these individual neurons. To implement this model, we would have to define (at least) the characteristics of each neuron (e.g., pyramidal or stellate, extent of dendritic branching, locations), the connections between neurons, and the connections from other brain regions. Unfortunately, a complete description of human cortical physiology does not exist. Even if we approximate this complicated physiology, we must simulate $\sim 10^5$ cortical neurons, and computational limits would still make this detailed simulation infeasible (although see [10, 11]). To model mesoscopic cortical electrical activity, we must utilize a different approach.

Here we will implement a model of mesoscopic cortical electrical activity. To construct such a model, researchers

have considered the spatially averaged electrical activity from neural populations [12, 13]. Although crude, these models have allowed researchers to make quantitative predictions for EEG and ECoG data. Perhaps more importantly, researchers have used these models to connect observed EEG data with cortical physiology.

In what follows, we consider the coupling and modeling of mesoscopic cortical electrical activity. We begin in Chapter 2 with a discussion of seven coupling measures. In Sections 2.1.2 - 2.1.3 we define the coupling measures, and in Sections 2.2 - 2.4 we apply the measures to simulated data. We apply some of the coupling measures to ECoG data in Section 2.5 and to EEG data in Section 2.6, and we suggest how both measures reveal changes in cortical communications. In Chapter 3 we present a model of mesoscopic cortical electrical activity recorded during seizure. We first discuss clinical ECoG data collected from four human subjects in Section 3.2. We then define the model in Section 3.3. We compare the model results, presented in Sections 3.4 - 3.5, with the observational data in Section 3.6, and we show that the two results agree in two important ways. In Section 3.7 we suggest three controllers to halt and abort seizures, and in Section 3.8 we interpret the model results to suggest how seizures may occur.

Chapter 2

Coupling measures

In this chapter we describe seven coupling measures and apply them to simulated and observed (i.e., EEG and ECoG) data. We begin in Section 2.1.1 with a brief introduction to the data and measures. In Sections 2.1.2 and 2.1.3 we define the linear (windowed cross-correlation and windowed coherence) and nonlinear (synchronization) measures, respectively. To investigate the properties of these measures we apply them to simulated data generated from the coupled Henon map (Section 2.2), the coupled Rössler system (Section 2.3), and simulated data containing bursts of oscillatory activity (Section 2.4). We then apply these measures to EEG and ECoG data recorded from the human scalp and cortex. In Section 2.5 we apply the coupling measures to ECoG data recorded from three electrodes during an auditory evoked-response potential experiment. We show that the synchronization results suggest a crude model of cortical connectivity. In Section 2.6 we apply three synchronization measures to scalp EEG data collected from healthy subjects and subjects diagnosed with dementia. We show how the average synchronization results provide a concise measure to differentiate the healthy subjects from those diagnosed with Alzheimer's disease. We interpret these results in terms of changes in cortical connectivity.

2.1 Definitions

2.1.1 Introduction

To investigate the relationships between two time series (in this case, recorded simultaneously from different scalp or cortical electrodes), we can utilize many different techniques. These include traditional measures of linear interdependence, such as the cross-correlation [14] and coherence [15] [16]. These two measures are related by the Fourier transform, and both assume stationarity of the time series [17]. To compare two nonstationary time series (e.g., EEG or ECoG data), we compute the cross-correlation and coherence between small temporal intervals, or windows, of the data. We define two windowed, linear coupling measures — the windowed cross-correlation and the windowed-coherence — in Section 2.1.2. During the past twenty years, many new techniques to detect nonlinear interdependence have been developed. These synchronization measures include identical synchronization [18], generalized synchronization [19], phase synchronization [20], and synchronization techniques robust to noisy data [21] [22]. We define five measures of nonlinear coupling in Section 2.1.3.

In general, one applies synchronization and linear coupling measures to pairs of time series derived from a single simulation or experiment. But, for a data set of interest in this work, an ensemble formalism is particularly useful. In many neuroelectrophysiologic studies researchers record EEG and ECoG data in response to a specific stimulus, for example an auditory tone. Typically in these evoked-response potential (ERP) experiments, the response to the sensory stimulus is oscillatory, weak, and of short duration. Therefore, an ensemble of ERPs are recorded (with time referenced to the stimulus onset), and various measures are averaged over the ensemble to improve the signal to noise ratio. Physically, ensemble averaging assumes that repetitive applications of the stimulus activate similar pathways in the brain [23]. We therefore expect that the ERP will begin at approximately the same time — say 100 ms — after each stimulus presentation. We further assume that the response of the cortex will trace approximately the same trajectory with each stimulus presentation. In what follows we will show how this assumption is useful.

To develop coupling measures appropriate for two ensembles of measurements, we adopt the following notation. We denote the ensembles of scalar time series $s^k[n]$ and $r^k[n]$, where the time index $n = \{1 \ldots n'\}$ and the ensemble index $k = \{1 \ldots k'\}$. Specifically, we think of $s^k[n]$ and $r^k[n]$ as the value of the electric potential recorded simultaneously at two different electrodes as a function of discrete time n. The physical time t is related to the discrete time n by $t = n\Delta t + t_0$ where t_0 is the initial time and Δt is the sampling interval. Each ensemble member k represents a unique realization of the same experiment. In what follows, we apply most of the coupling measures to the ensembles $s^k[n]$ and $r^k[n]$ in an obvious way; we compute the coupling between $s^k[n]$ and $r^k[n]$ for each k and then average the coupling results over the ensemble. But for one synchronization measure, $T(\mathbf{x}[n]|\mathbf{y})$, we exploit the ensemble nature

of the data; we discuss this measure in Section 2.1.3.

2.1.2 Linear Measures

In this section we state two measures of linear coupling, the cross-correlation and the coherence, and define windowed versions of each. Both measures have been extensively studied, and many excellent references are available [17, 8]. Here we outline the application of these measures to two ensembles, $s^k[n]$ and $r^k[n]$, and leave the details to the references. The ensemble averaged cross correlation coefficient is defined as,

$$\rho[t] = \frac{1}{k'} \sum_{k=1}^{k'} \Big(\sum_{n=1}^{n'-t} \frac{(s^k[n+t] - \vec{s}^k)(r^k[n] - \vec{r}^k)}{\sqrt{\sum_{n=1}^{n'} s^k[n] - \vec{s}^k} \sqrt{\sum_{n=1}^{n'} r^k[n] - \vec{r}^k}} \Big), \tag{2.1}$$

where $t \geq 0$ is the lag time, and $\vec{s}^k$ and $\vec{r}^k$ are the mean values of ensemble member $s^k[n]$ and $r^k[n]$, respectively. The expression for $t < 0$ is similar. Note that (2.1) includes the ensemble average over k. Next, the ensemble averaged coherence is defined as,

$$\gamma[f] = \frac{1}{k'} \sum_{k=1}^{k'} \frac{| G[s^k[n], r^k[n]] |}{\sqrt{G[s^k[n], s^k[n]]} \sqrt{G[r^k[n], r^k[n]]}}. \tag{2.2}$$

Here $G[s^k[n], r^k[n]]$ is the cross spectral density function of ensemble members $s^k[n]$ and $r^k[n]$, $G[s^k[n], s^k[n]]$ and $G[r^k[n], r^k[n]]$ are the auto spectral density functions of $s^k[n]$ and $r^k[n]$, respectively, and f is the frequency. Again the expression is averaged over the k' ensemble members.

In (2.1) and (2.2) we implicitly assume that the linear coupling between $s^k[n]$ and $r^k[n]$ remains constant over the duration of each ensemble member (i.e., that the cross-correlation and coherence are independent of time.) For neurophysiological time series, this assumption of stationarity is rarely satisfied. Instead, we may choose an ensemble duration short enough so that the data segment is effectively stationary but long enough to yield stable results [24]. The windowed cross-correlation (WCC) and windowed coherence (WC) are generalizations of the cross-correlation and coherence, respectively, that include time dependence. To compute the WCC, we first partition the data $s^k[n]$ and $r^k[n]$ with fixed k into overlapping windows. For example, the first window may include data for $0 \leq n \leq 10$, the second $5 \leq n \leq 15$, the third $10 \leq n \leq 20$, and so on. Here the windows have a duration of 10 indices and an overlap of 5 indices. We then compute the cross-correlation between $s^k[n]$ and $r^k[n]$ within each window. The result is the cross-correlation as a function of the lag time and the center time of the windows for each ensemble member k. We average these results over the k ensembles to determine the WCC. The windowed coherence (WC) between $s^k[n]$ and $r^k[n]$ is computed in a similar manner. We partition the data into overlapping windows, compute the coherence between $s^k[n]$ and $r^k[n]$ in each window for k fixed, and then average the results over the k' ensembles to determine

the WC. We note that the WC is identical to the event-related coherence defined in [25]. The result of computing the WC is coherence as a function of frequency and the center time of each window. We illustrate these linear measures in Sections 2.2-2.4 when we apply them to simulated data.

2.1.3 Synchronization Measures

In this section we define five synchronization measures in current use. Four of the synchronization measures require that we first *embed* the data $s^k[n]$ and $r^k[n]$. The goal of this embedding procedure is to transform the scalar time series data into vector time series data and reconstruct the state space of the system. We define vectors $\mathbf{x}^k[n] = (s^k[n], s^k[n+\tau], \ldots, s^k[n+(d-1)\tau])$ and $\mathbf{y}^k[n] = (r^k[n], r^k[n+\tau], \ldots, r^k[n+(d-1)\tau])$ from $s^k[n]$ and $r^k[n]$, respectively [26]. Here τ denotes the delay time and d the embedding dimension, which we assume are the same for both ensembles and all ensemble members. The goal in choosing these two parameters is to eliminate self-intersections of the dynamics that result from projecting the trajectory to lower dimensional space. The standard procedures for determining τ and d are demanding; τ is often assigned to be the time of the first minimum of the average mutual information, and d is calculated through a false nearest neighbors algorithm [26]. We provide detailed descriptions and examples of these procedures for the simulated data in Sections 2.2 and 2.3. Unfortunately, for the EEG and ECoG data of interest in this work, we cannot compute τ and d in this way. These observational data typically consist of short, noisy data sets for which the average mutual information and false nearest neighbor calculations are inaccurate. In fact, we do not know if the electrical activity recorded from the human cortex is the result of a low-dimensional deterministic process. Therefore, the embedding dimension of the cortex is not well-defined. In this chapter, we study the synchronization phenomena in a comparative way and do not suggest that the dynamics of cortical electrical activity are accurately modeled as a d-dimensional deterministic system [27]. We show in Section 2.6 that we can use different values of τ and d to compute stable coupling results.

We start by considering two synchronization measures, $S(\mathbf{x}[n]|\mathbf{y})$ and $H(\mathbf{x}[n]|\mathbf{y})$, which follow from [21]. We denote as $n_{k,i}$, where $i \in \{1,\ldots,N\}$, the time indices of the N nearest neighbors to the element $\mathbf{x}^k[n]$ of the k-th member of the ensemble at time n. For all of the synchronization measures that follow we define neighborhoods in terms of distance calculated using a Euclidean metric. We note that $\mathbf{x}^k[n]$ and its nearest neighbors are all elements of the k-th member of the ensemble. Define the mean squared Euclidean distance from the element $\mathbf{x}^k[n]$ to its N nearest neighbors as

$$R(\mathbf{x}^k[n]) = \frac{1}{N}\sum_{i=1}^{N}(\mathbf{x}^k[n] - \mathbf{x}^k[n_{k,i}])^2. \tag{2.3}$$

Note that $R(\mathbf{x}^k[n])$ is a function of time n through $\mathbf{x}^k[n]$. Similarly, we denote the time indices of the nearest neighbors

to $\mathbf{y}^k[n]$ as $m_{k,i}$ and define

$$R(\mathbf{x}^k[n]|\mathbf{y}) = \frac{1}{N}\sum_{i=1}^{N}(\mathbf{x}^k[n] - \mathbf{x}^k[m_{k,i}])^2. \tag{2.4}$$

Here, we calculate the average squared distance from $\mathbf{x}^k[n]$ to elements in the same ensemble k using the time indices $(m_{k,i})$ from ensemble $\mathbf{y}^k[n]$. Then we define

$$S(\mathbf{x}^k[n]|\mathbf{y}) = \frac{R(\mathbf{x}^k[n])}{R(\mathbf{x}^k[n]|\mathbf{y})}, \tag{2.5}$$

for the k^{th} ensemble. We average (2.5) over the ensembles to get

$$S(\mathbf{x}[n]|\mathbf{y}) = \frac{1}{k'}\sum_{k=1}^{k'}\frac{R(\mathbf{x}^k[n])}{R(\mathbf{x}^k[n]|\mathbf{y})}. \tag{2.6}$$

If the ensembles $\mathbf{x}$ and $\mathbf{y}$ are synchronous at time n then $S(\mathbf{x}[n]|\mathbf{y}) \to 1$; if they are independent, then $S(\mathbf{x}[n]|\mathbf{y}) \sim 0$. $S(\mathbf{x}[n]|\mathbf{y})$ is the first synchronization measure we consider. We note that a variation of this measure, intended to account for noisy data, can be found in [22].

To define the second synchronization measure, we compute the mean squared distance from $\mathbf{x}^k[n]$ to every time point in the ensemble k:

$$\bar{R}(\mathbf{x}^k[n]) = \frac{1}{P-1}\sum_{p=1}^{P}(\mathbf{x}^k[n] - \mathbf{x}^k[p])^2, \tag{2.7}$$

where $P = n' - (d-1)\tau$. Then, from [21], define

$$H(\mathbf{x}^k[n]|\mathbf{y}) = \log\frac{\bar{R}(\mathbf{x}^k[n])}{R(\mathbf{x}^k[n]|\mathbf{y})}, \tag{2.8}$$

which we average over the ensembles to obtain

$$H(\mathbf{x}[n]|\mathbf{y}) = \frac{1}{k'}\sum_{k=1}^{k'}\log\frac{\bar{R}(\mathbf{x}^k[n])}{R(\mathbf{x}^k[n]|\mathbf{y})} \tag{2.9}$$

as the second synchronization measure. For the third synchronization measure, we follow [28] and define a (nearly) normalized synchronization measure. In our notation this measure becomes

$$N(\mathbf{x}[n]|\mathbf{y}) = \frac{1}{k'}\sum_{k=1}^{k'}\frac{\bar{R}(\mathbf{x}^k[n]) - R(\mathbf{x}^k[n]|\mathbf{y})}{R(\mathbf{x}^k[n])}. \tag{2.10}$$

Note that $N(\mathbf{x}[n]|\mathbf{y})$ is also ensemble averaged. Equations (2.6), (2.9), and (2.10) are three well known synchronization

measures. Here we augment each measure with a simple ensemble averaging scheme. We apply the three measures to simulated data in Sections 2.2 and 2.3.

Before introducing the synchronization measure $T(x|y)$, we illustrate how the nearest neighbors are chosen in the synchronization measures $S(\mathbf{x}[n]|\mathbf{y})$, $H(\mathbf{x}[n]|\mathbf{y})$, and $N(\mathbf{x}[n]|\mathbf{y})$. In Figure 2.1(a) we show a typical ensemble member $s^k[n]$ for the ECoG ERP data we discuss in detail in Section 2.5. The stimulus (an auditory tone) occurs at time $t = 0$ ms. We note that before the stimulus the measured voltage fluctuates between ± 20 mV, while after the stimulus an oscillatory burst occurs between $t = 30$ ms and $t = 160$ ms. After the oscillatory burst, the voltage returns to its pre-stimulus range.

We now discuss the procedure for finding nearest neighbors to a point within the oscillatory burst. For illustrative purposes, we embedded the ensemble member $s^k[n]$ using $d = 3$ and $\tau = 10$. We note that these embedding parameters do not eliminate self-intersections of the dynamics. We show this embedding, $\mathbf{x}^k[n]$, in Figure 2.1(b). The point marked with an asterisk in Figures 2.1(a) and 2.1(b) is the same and corresponds to a point in the oscillatory burst of $s^k[n]$. Denote the time index of this point as n^*. In Figure 2.1(c) we show the local neighborhood of $\mathbf{x}^k[n^*]$, and we mark the five nearest neighbors to $\mathbf{x}^k[n^*]$ with triangles. It is clear from Figures 2.1(b) and 2.1(c) that the nearest neighbors to $\mathbf{x}^k[n^*]$ lie immediately along the trajectory passing through $\mathbf{x}^k[n^*]$. By excluding nearest neighbors within a local temporal window near $\mathbf{x}^k[n^*]$, we only succeed in selecting neighbors further along this isolated trajectory. For this case, the trajectory of a single ensemble member does not cover anything like an attractor in the embedding space. Therefore neighbors along the oscillatory burst must be defined with care. We show in what follows that by considering neighbors across the ensemble of measurements, we can — in this case — construct a more representative picture of the underlying dynamics when the data are available only in short data sets.

The fourth synchronization measure we propose is similar to those discussed in [21] and [28]. But, for this synchronization measure, nearest neighbors are chosen from across the ensemble of measurements, rather than from within each individual ensemble member. To illustrate this idea, we show in Figure 2.2(a) ten ensembles — collected in the ECoG ERP experiment we discuss in Section 2.5 — embedded using $d = 3$ and $\tau = 10$. The darkest curve in the figure is the single ensemble member shown in Figure 2.1(b). Now the element of ensemble k at time $t = n^*$, $\mathbf{x}^k[n^*]$, has a nearest neighbor in each ensemble $l \neq k$. Notice we do not include the nearest neighbor to $\mathbf{x}^k[n^*]$ in ensemble k. Finding a single nearest neighbor to $\mathbf{x}^k[n^*]$ in each ensemble $l \neq k$, rather than throughout a single time series, avoids the complications associated with serial correlations of the data from short data sets. In general we denote the time index of the nearest neighbor to $\mathbf{x}^k[n]$ in ensemble l as $n_{k,l}$ and call this set of neighbors the *nearest ensemble neighbors* to $\mathbf{x}^k[n]$. In Figure 2.2(b), we show the local neighborhood of the point $\mathbf{x}^k[n^*]$; we mark the point $\mathbf{x}^k[n^*]$ with an asterisk and the ten nearest ensemble neighbors to this point with triangles. Here the neighbors are chosen

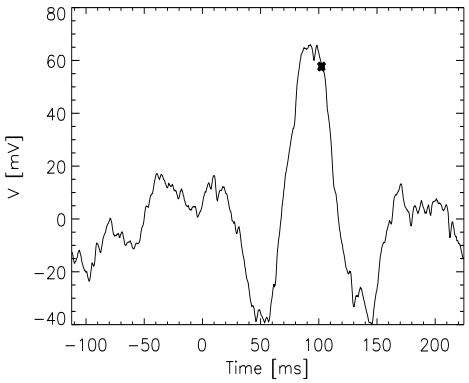

(a)

(b)

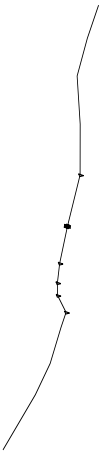

(c)

Figure 2.1: (a) The electric potential of one ensemble member recorded by one electrode in the ECoG ERP experiment we discuss in detail in Section 2.5. The stimulus occurs at $t = 0$ ms. Note the oscillatory burst between 30 ms and 160 ms. The asterisk marks a point on the oscillatory burst. (b) The embedding of the times series in (a). We chose $d = 3$ and $\tau = 10$ for illustrative purposes and project the 3-dimensional embedding onto the plane of the page. The asterisk in this figure corresponds to the asterisk in (a). (c) The local neighborhood of the point marked with an asterisk in (b). The five nearest neighbors to this point are marked by triangles. The nearest neighbors are temporally proximal to the fiducial point because the data set is short.

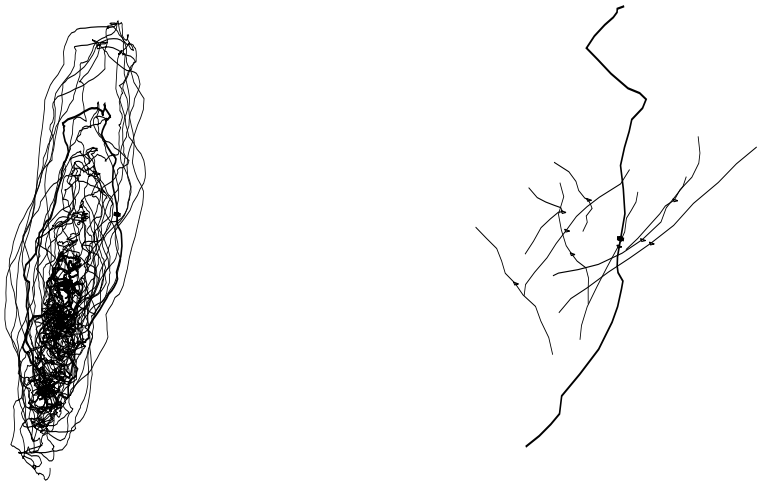

(a) (b)

Figure 2.2: (a) Ten ensemble members embedded using $d = 3$ and $\tau = 10$. The thickest curve is the ensemble member shown in Figures 2.1(a) and 2.1(b). The other nine ensemble members are difficult to distinguish. The point $\mathbf{x}^k[n^*]$ is marked with an asterisk. (b) The local neighborhood of the point $\mathbf{x}^k[n^*]$. The thickest curve is the the trajectory of $\mathbf{x}^k[n]$. The point $\mathbf{x}^k[n^*]$ is marked with an asterisk. The thin curves are trajectories of nine other ensemble members. The nearest ensemble neighbors are marked with triangles.

from across the ensemble of measurements, rather than within each individual ensemble member. Because we have assumed that the trajectory of each ensemble member follows similar dynamics, this method of determining neighbors is justified.

Now we define the new synchronization measure. As for the three synchronization measures already discussed, we reconstruct the state spaces of the time series $s^k[n]$ and $r^k[n]$ to create $\mathbf{x}^k[n]$ and $\mathbf{y}^k[n]$, respectively. For each time point n of every ensemble member k we calculate the mean Euclidean distance from $\mathbf{x}^k[n]$ to its $k' - 1$ nearest ensemble neighbors,

$$D(\mathbf{x}^k[n]) = \frac{1}{k'-1} \sum_{\substack{l=1 \\ l \neq k}}^{k'} \| \mathbf{x}^k[n] - \mathbf{x}^l[n_{k,l}] \| . \tag{2.11}$$

Here $\| \cdot \|$ denotes the Euclidean distance, and the $n_{k,l}$ are the time indices of the nearest ensemble neighbors to $\mathbf{x}^k[n]$. We also calculate the standard deviation $\sigma_D(\mathbf{x}^k[n])$ of the mean distance in (2.11). Similarly, we denote the time indices

of the nearest ensemble neighbors to $\mathbf{y}^k[n]$ as $m_{k,l}$, and then compute the following

$$T(\mathbf{x}^k[n]|\mathbf{y}) = \frac{1}{k'-1}\sum_{\substack{l=1\\ l\neq k}}^{k'} \Theta\big(D(\mathbf{x}^k[n]) + \sigma_D(\mathbf{x}^k[n]) - \parallel \mathbf{x}^k[n] - \mathbf{x}^l[m_{k,l}] \parallel \big), \tag{2.12}$$

where $\Theta(\cdot)$ is the Heaviside step function. In (2.12) we determine the distance from $\mathbf{x}^k[n]$ to each $\mathbf{x}^l[m_{k,l}]$. If this distance is less than $D(\mathbf{x}^k[n]) + \sigma_D(\mathbf{x}^k[n])$ (i.e. the average distance from $\mathbf{x}^k[n]$ to its nearest ensemble neighbors plus one standard deviation), then we define $\mathbf{x}^l[m_{k,l}]$ as a neighbor of $\mathbf{x}^k[n]$. Thus, a neighbor of $\mathbf{x}^k[n]$ and $\mathbf{y}^k[n]$ ($\mathbf{y}^l[m_{k,l}]$ and $\mathbf{x}^l[m_{k,l}]$, respectively) shares the same ensemble l and time index $m_{k,l}$. Call this neighbor a *shared neighbor* of $\mathbf{x}^k[n]$ and $\mathbf{y}^k[n]$. By summing the number of shared neighbors between $\mathbf{x}^k[n]$ and $\mathbf{y}^k[n]$, and dividing by the total number of possible neighbors — the number of ensemble members k' minus one — we measure the synchronization between the two time series at time n in (2.12). We average (2.12) over the ensemble of measurements to yield,

$$T(\mathbf{x}[n]|\mathbf{y}) = \frac{1}{k'}\sum_{k=1}^{k'} T(\mathbf{x}^k[n]|\mathbf{y}). \tag{2.13}$$

The fourth measure (2.13) differs from the three synchronization measures in (2.6), (2.9), and (2.10). In (2.13) we compute neighbors from across the ensemble of measurements and determine the fraction of shared neighbors between ensembles $\mathbf{y}$ and $\mathbf{x}$. If for some time index n this fraction approaches 1.0, then we say that the synchronization between the two ensembles is strong at time n. If this fraction approaches 0.0, then we say that the synchronization is weak. We include the standard deviation $\sigma_D(\mathbf{x}^k[n])$ in (2.12) to extend the radius of the neighborhood around $\mathbf{x}^k[n]$; a stricter measure of synchronization results if we exclude this term. The interpretation of (2.13) is somewhat clearer than the ratio of mean squared distances utilized in the synchronization methods $S(\mathbf{x}[n]|\mathbf{y})$, $H(\mathbf{x}[n]|\mathbf{y})$, and $N(\mathbf{x}[n]|\mathbf{y})$. We show in Section 2.4.1 that the ratio of mean squared distances can be misleading in certain types of examples.

All of the measures we have discussed determine the ensemble averaged synchronization between ensembles $\mathbf{x}$ and $\mathbf{y}$ at a specific time n. In some applications — ERP experiments, for example — it may be important to investigate time delayed synchronization. An idea along these lines was mentioned in [21]. In words, we would like to compare the synchronization between $\mathbf{x}^k[n]$ and $\mathbf{y}^k[m]$ when $n \neq m$; i.e. we would like to know whether $\mathbf{x}^k[n]$ at time n is related to $\mathbf{y}^k[m]$ at time m. To do so, we determine the time indices $m_{k,l}$ of the nearest ensemble neighbors to $\mathbf{y}^k[n]$. We then compute the distance between $\mathbf{x}^k[n]$ and $\mathbf{x}^l[m_{k,l}]$ for each $l \neq k$, and record the number of these points that lie close to $\mathbf{x}^k[n]$, as in (2.12). Now, we shift the time indices $m_{k,l}$ by an integer η. We then compute the distance between $\mathbf{x}^k[n+\eta]$ and $\mathbf{x}^l[m_{k,l}+\eta]$ for each $l \neq k$, and record the number of these points that lie close to $\mathbf{x}^k[n+\eta]$. Here we are comparing $\mathbf{x}^k[n+\eta]$ at time $(n+\eta)$ to the time shifted nearest ensemble neighbors of $\mathbf{y}^k[n]$ at time n. Equation (2.12)

is easily extended to include time shifted synchronization,

$$T(\mathbf{x}^k[n,\eta]|\mathbf{y}) = \frac{1}{k'-1}\sum_{\substack{l=1\\ l\neq k}}^{k'} \Theta\big(D(\mathbf{x}^k[n+\eta]) + \sigma_D(\mathbf{x}^k[n+\eta]) - \parallel \mathbf{x}^k[n+\eta] - \mathbf{x}^l[m_{k,l}+\eta] \parallel \big), \tag{2.14}$$

where η is an integer time shift. If the distance between $\mathbf{x}^k[n+\eta]$ and $\mathbf{x}^l[m_{k,l}+\eta]$ is less than $D(\mathbf{x}^k[n+\eta]) + \sigma_D(\mathbf{x}^k[n+\eta])$ for all $l \neq k$, then $T(\mathbf{x}^k[n,\eta]|\mathbf{y}) = 1.0$. It is important to keep in mind that the $m_{k,l}$ are still based on $\mathbf{y}^k[n]$, although this is lost in the notation of (2.14). We note that the time shifting scheme is essentially equivalent to delaying the ensembles before applying the measure defined in (2.13). We average (2.14) over the ensemble to obtain,

$$T(\mathbf{x}[n,\eta]|\mathbf{y}) = \frac{1}{k'}\sum_{k=1}^{k'} T(\mathbf{x}^k[n,\eta]|\mathbf{y}). \tag{2.15}$$

Equation (2.15) is the time shifted, ensemble averaged synchronization between ensembles $\mathbf{x}$ and $\mathbf{y}$. Any of the synchronization measures discussed above could have been modified to include time shifts, but we chose only to consider (2.15). We note that $T(\mathbf{x}^k[n,\eta]|\mathbf{y})$ and $T(\mathbf{y}^k[n,\eta]|\mathbf{x})$ measure different quantities; in the former neighborhoods of $\mathbf{y}$ are examined in $\mathbf{x}$, while in the latter neighborhoods in $\mathbf{x}$ are examined in $\mathbf{y}$. Determining the driver-response relationship from the asymmetry of these two synchronization measurements is not obvious. We refer the interested reader to [21] and [29].

The final synchronization measure that we consider is the phase synchronization $P(\theta)$. The phase synchronization differs from those synchronization measures already discussed in that we do not embed the scalar data $s^k[n]$ and $r^k[n]$. Instead, we first compute the Hilbert transforms of ensemble members $s^k[n]$ and $r^k[n]$ for k fixed. The Hilbert transform of the continuous time series $q[t]$ is,

$$Q[t] = \frac{1}{\pi}\int_{-\infty}^{\infty} \frac{q[\tau]}{t-\tau} d\tau. \tag{2.16}$$

We use (2.16) to construct the analytic signal $q[t] + \imath Q[t] = A[t]\exp^{\imath\theta[t]}$, which uniquely determines the amplitude $A[t]$ and phase $\theta[t]$ of $q[t]$. We apply this procedure to $s^k[n]$ and $r^k[n]$ (with k fixed) and extract the phase $\theta[n]$ from each as a function of index n. We then compute the phase difference between $s^k[n]$ and $r^k[n]$ at each n; this is identical to the $1:1$ phase locking in [30]. Finally, we define the phase synchronization between $s^k[n]$ and $r^k[n]$ as the probability that the phase difference between $s^k[n]$ and $r^k[n]$ assumes the value θ, where $0 \leq \theta < 2\pi$. We compute this phase synchronization between $s^k[n]$ and $r^k[n]$ for each ensemble member k and average the results over the ensemble. We define the fifth synchronization measure $P(\theta)$ as this ensemble averaged phase synchronization. We use a windowing procedure identical to that discussed for the linear measures in Section 2.1.2 to construct the windowed phase synchronization (WPS). The result of the WPS is phase synchronization as a function of phase θ and the center

time of each window.

Before we apply the seven coupling measures to experimental data, we investigate the properties of each. To do so, we apply each measure to simulated data in Sections 2.2 - 2.4. Following this analysis of simulated data, we apply some of the coupling measures to EEG and ECoG data in Sections 2.5 and 2.6. We use the results to suggest changes in cortical connectivity following an auditory stimulus and the effects of Alzheimer's disease.

2.2 Example: Henon map

To illustrate the linear and nonlinear coupling measures proposed in Sections 2.1.2 and 2.1.3, we apply each measure to simulated data. We start with the standard example of the unidirectionally coupled non-identical Henon map [22],

$$\begin{aligned} r^k[n] &= 1.4 - r^k[n-1]^2 + 0.3r^k[n-2] \\ s^k[n] &= 1.4 - \big(\kappa[n]r^k[n-1] + (1-\kappa[n])s^k[n-1]\big)s^k[n-1] + 0.1s^k[n-2]. \end{aligned} \tag{2.17}$$

Here, the ensemble members differ only in the initial values of $s^k[n]$ and $r^k[n]$, which are chosen randomly but avoid the fixed points of the system. We set the sampling interval $\Delta t = 1$ s, and assign the coupling strength $\kappa[n]$ the value 0.9 (strong coupling) when 100 s $< n <$ 150 s and 0.0 (no coupling) otherwise. Thus, we expect the coupling measures to detect interdependence between the ensemble members $s^k[n]$ and $r^k[n]$ only when the coupling is strong (i.e., when 100 s $< n <$ 150 s.) For this simulation we fix the number of ensemble members k' to forty, the duration of each ensemble member n' to 300, and scale each ensemble member to have zero mean.

In Figure 2.3(a) we show two typical ensemble members: $s^k[n]$ and $r^k[n]$ for $k = 1$. We note that the data possess no obvious structure and that the coupling for 100 s $< n <$ 150 s is not apparent. In what follows, we analyze the coupling between these two ensembles of data in the same way we analyze the observed ECoG and EEG data in Sections 2.5 - 2.6. Here we have the advantage of knowing the map (2.17) and coupling $\kappa[n]$ that determine the dynamics of $s^k[n]$ and $r^k[n]$.

Linear measures

We show in Figure 2.3(b) the WCC computed between the ensembles $s^k[n]$ and $r^k[n]$. To compute the WCC, we chose overlapping windows of duration 30 s and overlap 15 s. For example, in the first window we compute the cross-correlation between $s^k[n]$ and $r^k[n]$ for 0 s $< n <$ 30 s, in the second for 15 s $< n <$ 45 s, in the third for 30 s

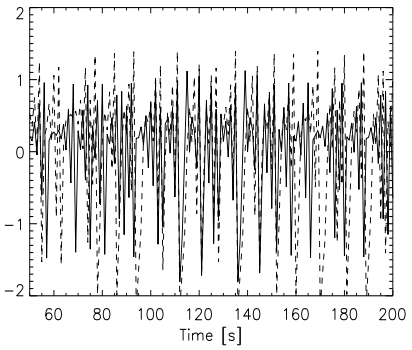

(a)

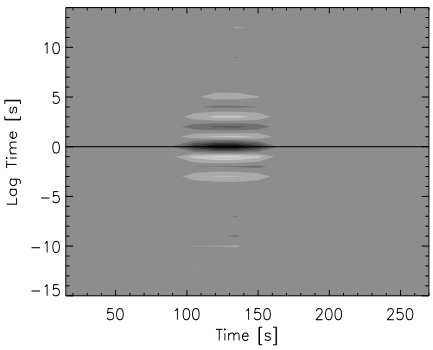

(b)

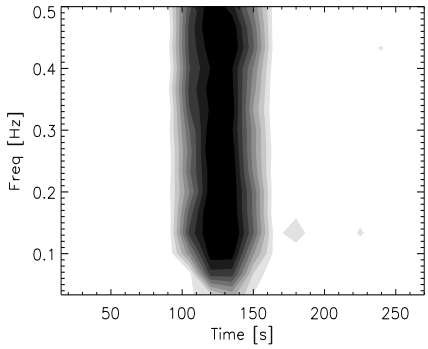

(c)

Figure 2.3: (a) The first ensemble members of $s^k[n]$ (solid line) and $r^k[n]$ (dashed line) generated from the unidirectionally coupled non-identical Henon map for 50 s $< n <$ 200 s. The coupling for 100 s $< n <$ 150 s is not obvious. (b) The windowed cross-correlation (WCC) between $s^k[n]$ and $r^k[n]$. We plot the center time of each window along the horizontal axis, the lag time along the vertical axis, and the value of the cross-correlation in linear greyscale with values greater than 0.8 in black, less than -0.8 in white, and near 0.0 in grey. All WCC figures follow this color scheme unless otherwise indicated. The WCC reveals a strong correlation between $s^k[n]$ and $r^k[n]$ at zero lag for 100 s $< n <$ 150 s. (c) The windowed coherence (WC) between $s^k[n]$ and $r^k[n]$. We plot the center time of each window along the horizontal axis, the frequency along the vertical axis, and the value of the coherence in linear greyscale with values greater than 0.8 in black and near 0.0 in white. The coherence between $s^k[n]$ and $r^k[n]$ is strong for all frequencies when 100 s $< n <$ 150 s.

$< n <$ 60 s, and so on. In Figure 2.3(b) we plot the WCC in linear greyscale with values greater than 0.8 in black, near 0.0 in grey, and less than -0.8 in white. The horizontal axis indicates the center time of each window, and the vertical axis the lag-time; we denote the location of zero lag with a horizontal line. We conclude from this figure that a region of strong correlation exists between $s^k[n]$ and $r^k[n]$ for 100 s $< n <$ 150 s, as expected. In this case, the linear WCC measure detects the nonlinear coupling between the two dynamical maps in (2.17).

We show in Figure 2.3(c) the WC computed between the ensembles $s^k[n]$ and $r^k[n]$. The windowing is the same as for the WCC. We plot the WC in linear greyscale with black and white representing coherence values greater the 0.8 and near 0.0, respectively. The horizontal axis indicates the center time of each window, and the vertical axis the frequency (up to the Nyquist frequency, in this case 0.5 Hz.) We find a region of strong coherence between $s^k[n]$ and $r^k[n]$ for nearly all frequencies. Here again, a linear measure — the WC — detects the nonlinear coupling between the two dynamical maps in (2.17).

Nonlinear measures

Before applying four of the synchronization measures to the data, we must first embed $s^k[n]$ and $r^k[n]$; therefore, we must chose the embedding dimension d and delay time τ. As mentioned in Section 2.1.3, specific algorithms exist to determine d and τ. Here we briefly describe these algorithms and apply them to the simulated data from (2.17).

In choosing τ, we determine the coordinates of the embedded vector. For example, given the scalar time series $q[n]$ we can construct the two-dimensional vector $\mathbf{x}[n] = \{q[n], q[n+\tau]\}$. The value of τ determines the second coordinate $q[n+\tau]$ of $\mathbf{x}[n]$. The goal is to chose τ such that each new coordinate of $\mathbf{x}[n]$ provides the maximum amount of new information about the dynamics. For example, consider the case in which $q[n]$ possesses strong serial correlations. If we choose $\tau = 1$ the second coordinate of $\mathbf{x}[n] = \{q[n], q[n+1]\}$ would provide little new information about the dynamics; knowing $q[n]$ we can accurately predict $q[n+1]$ due to the strong serial correlations in the data. In this case, we may choose $\tau \gg 1$.

For noise free data, a prescription exists for choosing τ. Typically, we chose τ to be the first minimum of the average mutual information (AMI) of the scalar time series (e.g., $q[n]$ or $s^k[n]$ with k fixed) with itself. In this way we insure that each new coordinate provides the most new information about the dynamics. The computation of the AMI requires a complete sampling of the attractor. For the simulated data from the Henon maps, this is not achieved by the individual ensemble members of $s^k[n]$ which contain only $n' = 300$ points. Therefore, we compute the AMI of $s^k[n]$ concatenated over all ensemble members (for a total of $300 \times 40 = 12000$ points.) We could have increased n' simply by continuing iteration of the map (2.17). But for the ECoG and EEG data we consider in Sections 2.5 and 2.6 a retrospective continuation of the observation is impossible. We therefore proceed with the analysis of $s^k[n]$ with

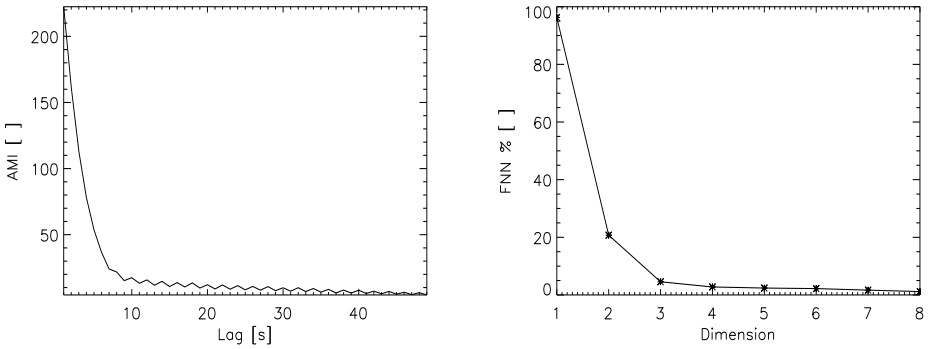

(a) (b)

Figure 2.4: Computation of the embedding parameters for the time series generated from the unidirectionally coupled non-identical Henon map. (a) The average mutual information (AMI) of the concatenated $s^k[n]$ as a function of time lag. No relative minimum exists for any lag. (b) The percentage of false nearest neighbors of the concatenated $s^k[n]$ as a function of the embedding dimension. The value asymptotes to a small, positive number for dimension 4 and greater. This is due to the random initial values of $s^k[n]$ for each ensemble member.

$n' = 300$ and $k' = 40$.

We show in Figure 2.4(a) the AMI computed for the concatenated version of $s^k[n]$. The AMI decreases rapidly from a maximum value at $\tau = 1$ s. In this case, no obvious minimum in the AMI exists, and we may choose τ to equal the time at which the AMI reaches 25% of its maximum value [26]. Here, we would chose $\tau = 5$ s. We note that this procedure for choosing τ is only prescriptive. Instead of using the AMI to compute τ, we could have chosen τ to be the first minimum of the auto-correlation of the concatenated $s^k[n]$. In general, an optimal choice for τ does not exist and a wide range of values is acceptable [26, 31]. Here we simply set $\tau = 2$ s. At this τ, the AMI plotted in Figure 2.4(a) achieves 75% of the maximum value. We find (but do not show) similar synchronization results for $\tau = 5$ s.

With τ fixed, we must now determine the embedding dimension d. To do so, we distinguish between the true dynamics of the system and the observed dynamics. We assume that the true dynamics of the system are governed by a n-dimensional system of differential or difference equations. For observational data, these equations typically are unknown and only a 1-dimensional time series (e.g., the voltage recorded at an electrode) is observed. Thus, although the true (and usually unknown) dynamics of the system occur in $\mathbf{R}^n$, we only observe a projection of the dynamics of $\mathbf{R}^1$. In this 1-dimensional space, a trajectory may cross itself, as evidenced in Figure 2.3(a). But in the original phase space of the dynamical system (i.e., in $\mathbf{R}^n$) a trajectory may not cross itself (due to the uniqueness of solutions.) Therefore, to choose d, we determine the dimension that eliminates false-crossings of the trajectory with

itself due to a projection of the dynamics onto a lower-dimensional space. This procedure requires that we determine the percentage of *false nearest neighbors* in each dimension. If two points are true nearest neighbors, then these points remain neighbors regardless of the embedding dimension. But, if two points are false nearest neighbors, then there exists a large enough dimension at which these points cease to be neighbors.

To choose d, we determine the dimension in which the percentage of false nearest neighbors approaches zero. The algorithm is simple, but computationally expensive. As for the AMI calculation, we first concatenate the ensemble members of $s^k[n]$ to establish a scalar time series of 12000 points that sample the entire attractor. We then embed the concatenated $s[n]$ in dimension d to create the vector $\mathbf{x}[n] = \{s[n], s[n+\tau], \ldots, s[n+(d-1)\tau]\}$. For each point in $\mathbf{x}[n]$ we determine its nearest neighbor which is labeled by a unique time m. Then, we embed $s[n]$ in dimension $d+1$. If the nearest neighbor to $\mathbf{x}[n]$ (now in $(d+1)$-dimensions) still occurs at time m, then these points are true nearest neighbors; otherwise, these points are false nearest neighbors. We continue this procedure until we determine the dimension d at which the percentage of false nearest neighbors approaches 0.0.

We show the result of the false nearest neighbor calculation in Figure 2.4(b). The percentage of false nearest neighbors for $d = 1$ is high, as expected, because the higher dimensional map is projected onto a lower dimensional space. At $d = 4$, the percentage of false nearest neighbors asymptotes to a positive value near zero. This result agrees with the known system in (2.17) which consists of two, coupled Henon maps (each with an embedding dimension of 2.) The reason that the percentage of false nearest neighbors asymptotically approaches a small positive value is that we analyzed a concatenated version of the dynamics $s^k[n]$. For each ensemble member k, the first point ($n = 0$) is a random number. Therefore, the concatenated dynamics contain a small percentage (0.33%) of random numbers. These random numbers are distributed uniformly throughout space of any dimension, and a small percentage of false nearest neighbors will exist for any d.

We have now determined the delay time $\tau = 2$ s and the embedding dimension $d = 4$ for $s^k[n]$ and can reconstruct the state space vector $\mathbf{x}^k[n]$. We use these same embedding parameters to define $\mathbf{y}^k[n]$ from $r^k[n]$. With the two state space vectors, we may now compute the measures of nonlinear coupling. In Figure 2.5(a) we show the synchronization measures $S(\mathbf{x}[n]|\mathbf{y})$ (dashed), $H(\mathbf{x}[n]|\mathbf{y})$ (dotted), and $N(\mathbf{x}[n]|\mathbf{y})$ (solid.) We find that all three measures increase during the interval of nonlinear coupling between the two ensembles: 100 s $< n <$ 150 s. In Figure 2.5(b) we show the time shifted synchronization measure $T(\mathbf{x}[n,\eta]|\mathbf{y})$. We plot the time along $r^k[n]$ and $s^k[n]$ in the horizontal and vertical directions, respectively, and the value of $T(\mathbf{x}[n,\eta]|\mathbf{y})$ in linear greyscale with values greater than 0.08 in black and near 0.0 in white. Again, the nonlinear coupling between the two ensembles is clear and appears as the thin diagonal band in the contour plot. From the location of the band in Figure 2.5(b) we conclude that ensembles $\mathbf{x}^k[n]$ and $\mathbf{y}^k[n]$ are synchronous when 100 s $< n <$ 150 s; i.e. the two are coupled with no time shift. The reader may wonder why

the values of $T(\mathbf{x}[n,\eta]|\mathbf{y})$ are so small. This follows from the rather tight definition we have adopted in (2.14) for the neighborhood of $\mathbf{x}^k[n]$; for this example, we set $\sigma_D = 0.0$ in (2.14). It may be profitable to relax this definition for noisy data.

Finally, in Figure 2.5(c) we show the windowed phase synchronization $P(\theta)$ between $s^k[n]$ and $r^k[n]$. We plot the center time of each window along the horizontal axis, the phase (in radians) along the vertical axis, and the value of the phase synchronization in linear greyscale, with values greater than 0.1 in black and near 0.0 in white. We find a region of strong phase synchronization at angles near 0.0 (or equivalently near 2π) for 100 s $< n <$ 150 s. This result reveals that the coupling between $s^k[n]$ and $r^k[n]$ is in phase with zero phase lag.

In summary we have applied seven coupling measures (the WCC, WC, and five synchronization measures) to the ensembles of data generated from (2.17). We have shown that each measure (both the linear and nonlinear) detects the coupling between $s^k[n]$ and $r^k[n]$. Because each measure detects this coupling, there is no need to apply all seven. In Sections 2.3 and 2.4 we show two examples in which some of the coupling measures provide erroneous results.

2.3 Example: coupled Rössler oscillators

In Section 2.2 we applied seven coupling measures to simulated data produced by two, coupled difference equations. Here we apply the coupling measures to data computed from a system of coupled differential equations. Specifically, we consider the coupled Rössler oscillators [32]:

$$\begin{aligned}
\dot{x}_1[t] &= -\omega_1 y_1[t] - z_1[t] + \gamma[t](x_2[t-2] - x_1[t]) \\
\dot{y}_1[t] &= -\omega_1 x_1[t] + A y_1[t] \\
\dot{z}_1[t] &= B + z_1[t](x_1[t] - \mu) \\
\dot{x}_2[t] &= -\omega_2 y_2[t] - z_2[t] \\
\dot{y}_2[t] &= -\omega_2 x_2[t] + A y_2[t] \\
\dot{z}_2[t] &= B + z_2[t](x_2[t] - \mu).
\end{aligned} \tag{2.18}$$

We denote the first and second subsystems with the subscripts 1 and 2, respectively. The parameters $A = 0.15$, $B = 0.2$, and $\mu = 6.8$ govern the dynamics of each subsystem, and $\omega_1 = 1.5$ and $\omega_2 = 0.5$ determine the basic frequencies of each subsystem. The parameter $\gamma[t]$ in the first equation of (2.18) controls the coupling of subsystem 2 with subsystem 1. We set $\gamma[t] = 0.5$ (moderate coupling) for 40 s $< t <$ 60 s, and $\gamma[t] = 0.0$ (no coupling), otherwise. The expression $x_2[t-2]$ denotes the value of x_2 at time $t-2$ s (i.e., the value of x_2 two seconds in the past.) Thus, the velocity of

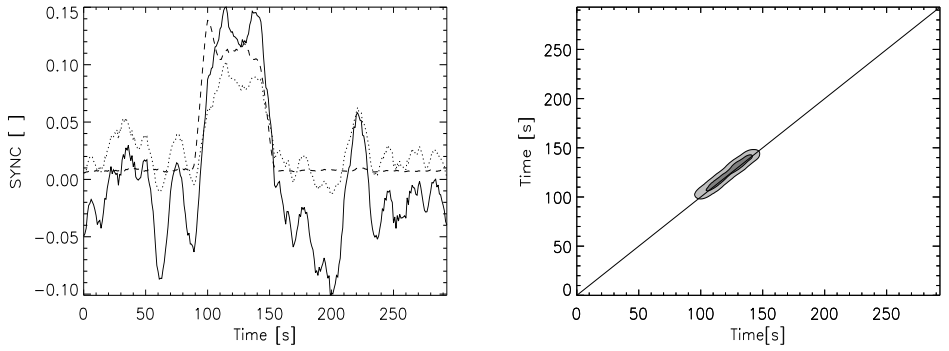

(a)

(b)

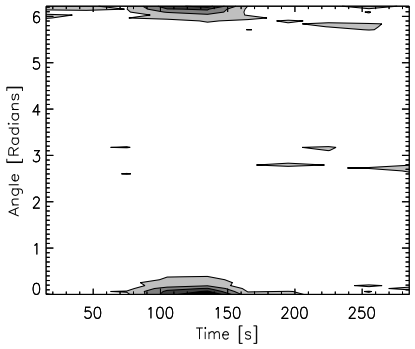

(c)

Figure 2.5: Synchronization measures applied to the unidirectionally coupled non-identical Henon map. (a) Three synchronization measures: $S(\mathbf{x}[n]|\mathbf{y})$ (dashed), $H(\mathbf{x}[n]|\mathbf{y})$ (dotted), $N(\mathbf{x}[n]|\mathbf{y})$ (solid). All of the measures are smoothed over a window of size 11 at each time point. All three measures increase during the interval of nonlinear coupling (100 s $< n <$ 150 s) between the chaotic time series. (b) The time shifted synchronization measure $T(\mathbf{x}[n,\eta]|\mathbf{y})$ smoothed over a two-dimensional window of size 11 at each time point. Note that the horizontal and vertical axes show time along ensembles $r^k[n]$ and $s^k[n]$, respectively. In the contour plot, there are five evenly spaced contour levels, ranging from 0.0 (white) to 0.08 (black). Unless defined otherwise, all $T(\mathbf{x}[n,\eta]|\mathbf{y})$ figures follow this grey-scale scheme. The diagonal line in the figure corresponds to the location of zero time lag. The contour plot shows synchronization occurs with time shift $\eta = 0$ during the time interval 100 s $< n <$ 150 s. (c) The windowed phase synchronization. We plot the center time of each window along the horizontal axis, the phase (in radians) along the vertical axis, and the value of the phase synchronization in linear greyscale, with values greater than 0.1 in black and near 0.0 in white. A region of strong phase synchronization occurs at angles near 0.0 (or equivalently near 2π) for 100 s $< n <$ 150 s.

x_1 at time t depends on the value of x_2 at time $t-2$ s. We note that the dynamics of subsystem 2 do not depend on subsystem 1.

In Figure 2.6(a) we plot an example of x_1 (solid line) and x_2 (dashed line) for 0 s $< t <$ 120 s. To calculate these time series, we solve (2.18) numerically using a forth-order Runge-Kutta method with time step $\Delta t = 0.2$ s and initial time $t_0 = -1880$ s. We choose random initial conditions for the trajectory and iterate the uncoupled differential equations so that, at $t = 0$ s, both subsystems evolve on their independent Rössler attractors. We note that the dynamics of x_1 appear to change for 40 s $< t <$ 60 s, but that the moderate coupling between x_1 and x_2 is not obvious through visual inspection.

We now apply the coupling measures of Sections 2.1.2 and 2.1.3 to the data from the coupled Rössler oscillators. To do so, we construct the ensembles $s^k[n]$ and $r^k[n]$ such that each ensemble member k is a numerical solution of (2.18) for x_1 and x_2, respectively, with random initial conditions. We calculate x_1 and x_2 following the procedure used to create the time series shown in Figure 2.6(a). We then scale x_1 and x_2 to have zero mean, and set $s^k[n]$ to x_1 and $r^k[n]$ to x_2 for 0 s $< t <$ 120 s. We repeat this procedure until the ensembles contain $k' = 30$ members.

We show the results of the linear coupling measures in Figures 2.6(b) and 2.6(c). The WCC, shown in Figure 2.6(b), achieves a small positive value at time lags between -2.0 s and 2.0 s for 40 s $< t <$ 60 s. From this result we might conclude that a weak correlation between $s^k[n]$ and $r^k[n]$ occurs although we cannot determine the lead/lag relationship from the WCC result. Similarly, from the WC result shown in Figure 2.6(c) we detect a weak interval of coupling (40 s $< t <$ 60 s) between the ensembles. For this example, the results of both linear measures suggest coupling occurs between $s^k[n]$ and $r^k[n]$. The measures correctly identify the time interval of this coupling, but neither reveals the lead/lag relationship between the ensembles.

Knowing that the linear measures detect a weak coupling between $s^k[n]$ and $r^k[n]$, we apply the nonlinear coupling measures. To compute four of the measures, we must first embed the time series. We follow the procedures described in Section 2.2 to compute the delay time τ and embedding dimension d. In Figure 2.7(a) we plot the AMI computed for the concatenated version of $s^k[n]$. The first relative minimum of the AMI occurs at a lag of 1 s; therefore we choose $\tau = 1$ s. In Figure 2.7(b) we plot the percentage of false nearest neighbors as a function of dimension. This percentage decreases rapidly and approaches a small, positive value for dimensions greater than five. Again, the percentage of false nearest neighbors does not reach zero due to the small number ($k' = 20$) of random initial conditions included in the concatenated $s^k[n]$. Therefore, we set $d = 6$, equal to twice the embedding dimension of the Rössler attractor.

Having determined $\tau = 1$ s and $d = 6$, we construct the state space vectors $\mathbf{x}^k[n]$ and $\mathbf{y}^k[n]$ from $s^k[n]$ and $r^k[n]$, respectively. We show in Figure 2.8(a) the synchronization measures $S(\mathbf{x}[n]|\mathbf{y})$ (dashed line), $H(\mathbf{x}[n]|\mathbf{y})$ (dotted line), and $N(\mathbf{x}[n]|\mathbf{y})$ (solid line) applied to this embedded Rössler data. Two of the measures, $H(\mathbf{x}[n]|\mathbf{y})$ and $N(\mathbf{x}[n]|\mathbf{y})$,

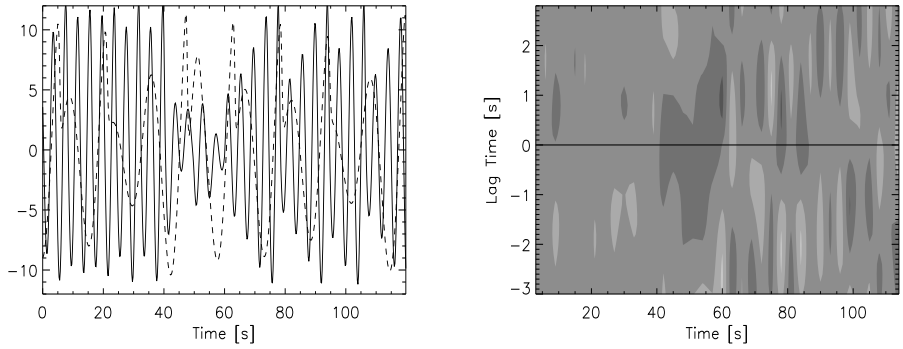

(a) (b)

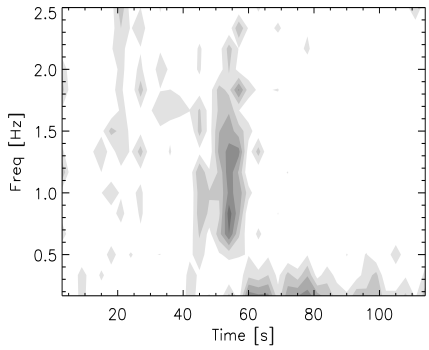

(c)

Figure 2.6: Example data and linear analysis for time series generated from the coupled Rössler oscillators system. (a) The first ensemble member ($k = 1$) pair $s^k[n]$ (solid line) and $r^k[n]$ (dashed line). The coupling for 40 s $< t <$ 60 s is not apparent. (b) The WCC between $s^k[n]$ and $r^k[n]$. The color scheme is the same as that used to create Figure 2.3(b). (c) The WC between $s^k[n]$ and $r^k[n]$. The color scheme is the same as that used to create Figure 2.3(c).

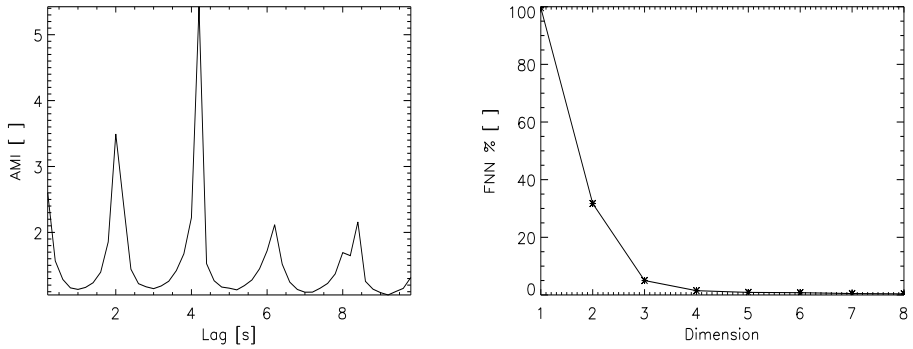

(a) (b)

Figure 2.7: Computation of the embedding parameters for the time series generated from the coupled Rössler oscillators. (a) The average mutual information (AMI) of the concatenated $s^k[n]$ as a function of time lag. The first relative minimum occurs at a lag of 1 s. (b) The percentage of false nearest neighbors of the concatenated $s^k[n]$ as a function of the embedding dimension. The value asymptotes to a small, positive number for dimensions greater than 5.

decrease during the coupling interval 45 s $< n <$ 70 s. Thus, using these measures, we incorrectly conclude that the coupling between $s^k[n]$ and $r^k[n]$ weakens during the interval of known coupling. The third measure $S(\mathbf{x}[n]|\mathbf{y})$ does increase during the know coupling interval (35 s $< n <$ 50 s) but we show in Section 2.4 that $S(\mathbf{x}[n]|\mathbf{y})$ can give spurious results for oscillatory data. In fact, we expect none of these measures to reveal the increased coupling for 40 s $< t <$ 60 s. These synchronization measures only detect simultaneous coupling between $s^k[n]$ and $r^k[n]$, and cannot detect the delayed effect of x_2 on x_1.

In Figure 2.8(b) we show the time shifted synchronization measure $T(\mathbf{x}[n,\eta]|\mathbf{y})$. The region of maximum $T(\mathbf{x}[n,\eta]|\mathbf{y})$ begins approximately 4 s above the diagonal (i.e., $\eta = 4$ s) and continues to larger values of η. This result indicates that $r^k[n]$ leads $s^k[n]$ during the interval of strongest coupling. Moreover, the largest values of $T(\mathbf{x}[n,\eta]|\mathbf{y})$ occur during the time intervals 35 s $< t <$ 50 s in $r^k[n]$ (along the horizontal axis) and 45 s $< t <$ 60 s in $s^k[n]$ (along the vertical axis). Thus we may use the synchronization measure $T(\mathbf{x}[n,\eta]|\mathbf{y})$ to detect the changes in coupling and lead/lag relationship between $s^k[n]$ and $r^k[n]$, although we do not determine the exact delay in coupling of 2 s.

Finally, we show the phase synchronization between $s^k[n]$ and $r^k[n]$ in Figure 2.8(c). The phase synchronization increases slightly for 40 s $< t <$ 60 s at angles less than 1.0 radian and near 2π radians. From this result, we conclude that weak phase coupling occurs between $s^k[n]$ and $r^k[n]$, but we cannot determine the lead/lag relationship of the ensembles from this measure.

We now summarize the results of this section. To determine the coupling between two times series generated from

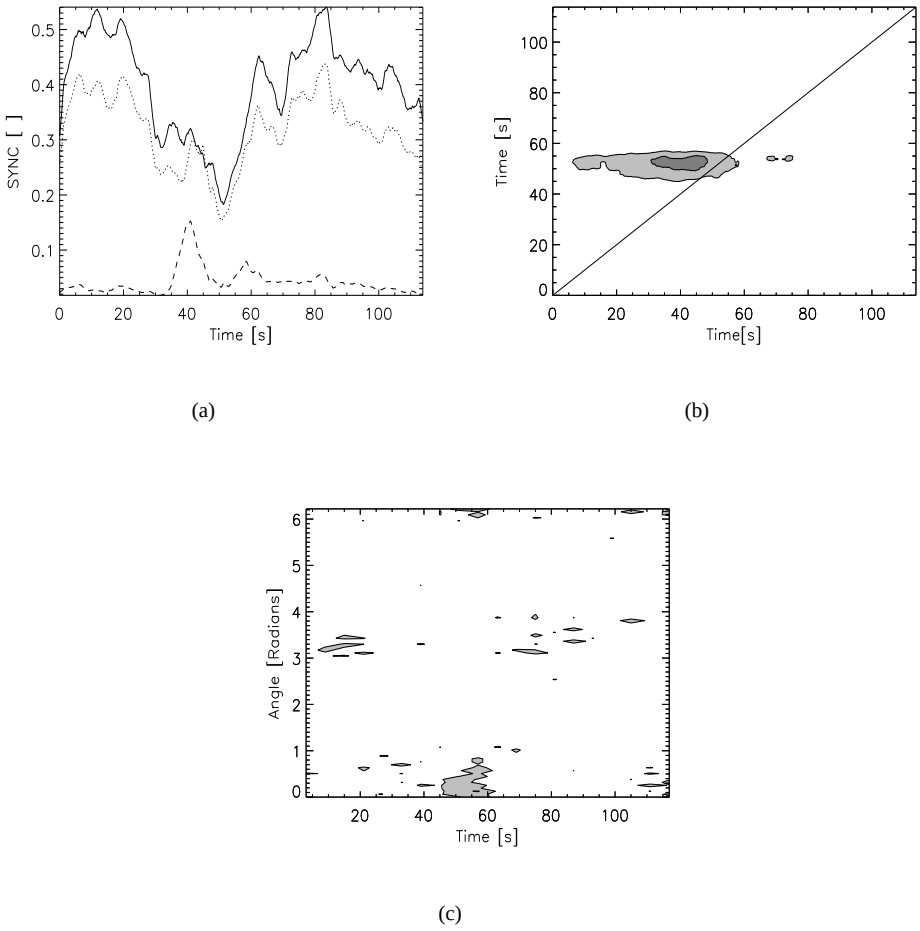

(a)

(b)

(c)

Figure 2.8: Synchronization measures applied to the coupled Rössler system. (a) Three synchronization measures: $S(\mathbf{x}[n]|\mathbf{y})$ (dashed), $H(\mathbf{x}[n]|\mathbf{y})$ (dotted), $N(\mathbf{x}[n]|\mathbf{y})$ (solid). All of the measures are smoothed over a window of size 11 at each time point. Two of the measures $H(\mathbf{x}[n]|\mathbf{y})$ and $N(\mathbf{x}[n]|\mathbf{y})$ decrease during the known interval of moderate coupling between $s^k[n]$ and $r^k[n]$. (b) The time shifted synchronization measure $T(\mathbf{x}[n,\eta]|\mathbf{y})$ smoothed over a two-dimensional window of size 11 at each time point. Note that the horizontal and vertical axes show time along ensembles $r^k[n]$ and $s^k[n]$, respectively. The color scheme is the same as in Figure 2.5(b). The diagonal line in the figure corresponds to the location of zero time lag. The region of maximum $T(\mathbf{x}[n,\eta]|\mathbf{y})$ begins approximately 4 s above the diagonal. (c) The windowed phase synchronization between $s^k[n]$ and $r^k[n]$. The color scheme is the same as that used to create Figure 2.5(c). An interval of weak phase synchronization occurs at angles less than 1.0 radian and near 2π radians for 40 s $< t <$ 60 s.

the coupled Rössler oscillators (2.18), we applied seven coupling measures. We showed that both linear measures (WCC and WC) detect weak coupling between the ensembles but fail to reveal that $r^k[n]$ leads $s^k[n]$. Of the five synchronization measures, two — $H(\mathbf{x}[n]|\mathbf{y})$ and $N(\mathbf{x}[n]|\mathbf{y})$ — failed to detect the coupling. Only the synchronization measures $S(\mathbf{x}[n]|\mathbf{y})$, $T(\mathbf{x}[n,\eta]|\mathbf{y})$, and $P(\theta)$ revealed the coupling between $s^k[n]$ and $r^k[n]$. (We show in the next section that, for ensembles of oscillatory time series, the measure $S(\mathbf{x}[n]|\mathbf{y})$ is unreliable.) The $T(\mathbf{x}[n,\eta]|\mathbf{y})$ result revealed not only the approximate time interval of the coupling, but also the approximate lead/lag relationship between $s^k[n]$ and $r^k[n]$.

2.4 Example: Oscillatory Bursts

In this last set of examples, we apply the linear and nonlinear coupling measures to simulated data motivated by voltage recordings from the human scalp and cortical surfaces during an ERP experiment. In typical EEG and ECoG ERP time series data, weak bursts of oscillatory activity occur. For example, an auditory stimulus may evoke a 10 Hz burst in one electrode, followed by a 40 Hz burst in another electrode [33]. Our goal in this section is to determine which of the coupling measures accurately detect this specific type of interdependence. We show that — of the synchronization measures — we may only use $T(\mathbf{x}[n,\eta]|\mathbf{y})$ to detect interdependent bursts of oscillatory activity occurring between the two ensembles. For the two examples in this section, we set the total number of ensemble members to twenty ($k' = 20$), the sampling interval $\Delta t = 1$ ms, and $\sigma_D = 1.0$ in (2.14) to extend the radius of local neighborhoods for noisy data.

2.4.1 Bursting data versus noise

We start by considering the case where the two ensembles of time series measurements $s^k[n]$ and $r^k[n]$ are unrelated. Specifically, we simulate the case where one electrode measures a response to a stimulus while the other electrode does not. We expect that all of the coupling measures will detect no interdependence between these two ensembles of measurements. However, we show that the measure $S(\mathbf{x}[n]|\mathbf{y})$ erroneously detects synchronization between the ensembles and explain why this occurs.

We construct $s^k[n]$ such that each ensemble member consists of identical, weak bursts of oscillatory behavior when 100 ms $< n <$ 150 ms. Each ensemble member is further constructed from 200 sinusoids, where each sinusoid is assigned a random uniformly-distributed frequency (from 0 to 100 Hz) and random uniformly-distributed phase (from $-\pi$ to π). We scale this sum of 200 sinusoids such that the ratio of the oscillatory burst amplitude to the amplitude of

the summed sinusoids is approximately 2. We denote this ratio of amplitudes as the signal-to-noise ratio (SNR). Here the oscillatory bursts represent evoked responses while the sinusoids act as noise. We shall refer to this type of noise as *sinusoidal noise*. In this example, the ensemble members of $r^k[n]$ consist only of sinusoidal noise (i.e., these ensemble members possess no evoked responses.) We show an example of the individual ensemble members in Figure 2.9(a). Here the weak evoked response of $s^k[n]$ (solid line) is mostly hidden by the noise. After averaging the time series over the ensembles, the evoked response in ensemble $s^k[n]$ and lack of response in ensemble $r^k[n]$ become apparent in Figure 2.9(b).

We show in Figures 2.9(c) and 2.9(d) the WCC and WC, respectively, computed between the ensembles. As expected, the values of both measures remain near zero for all times. Thus, from the linear measures, we correctly conclude that no coupling between $s^k[n]$ and $r^k[n]$ occurs. To calculate the synchronization between the two ensembles we chose $\tau = 1$ and $d = 10$ to reconstruct the state space vectors, $\mathbf{x}^k[n]$ and $\mathbf{y}^k[n]$ from $s^k[n]$ and $r^k[n]$, respectively. Unlike the analysis in Sections 2.2 and 2.3, we do not compute τ and d using the AMI and false nearest neighbor procedures, respectively. For noisy data — like those we use in this example — these procedures are inappropriate. Thus, we simply assign the values of τ and d. We illustrate in Section 2.4.2 how the synchronization results depend upon the choice of τ and d.

In Figure 2.10 we show the synchronization results for $s^k[n]$ and $r^k[n]$. We expect all of the measures to detect no synchronization between the two ensembles. In Figure 2.10(a) we plot the synchronization measures $S(\mathbf{x}[n]|\mathbf{y})$ (dashed line), $H(\mathbf{x}[n]|\mathbf{y})$ (dotted line), and $N(\mathbf{x}[n]|\mathbf{y})$ (solid line). Both $H(\mathbf{x}[n]|\mathbf{y})$ and $N(\mathbf{x}[n]|\mathbf{y})$ fluctuate between 0.15 and 0.45 but possess no obvious structure suggestive of a change in synchronization between the two ensembles. $S(\mathbf{x}[n]|\mathbf{y})$, though, suggests at least a doubling (~ 0.1 to ~ 0.25) in synchronization between the two ensembles during the time of the oscillatory burst in $s^k[n]$. This is caused by the numerator of (2.5), $R(\mathbf{x}^k[n])$, which increases during the oscillatory burst due to the increased distance from $\mathbf{x}^k[n]$ to its nearest neighbors during this interval. The denominator of (2.5) — $R(\mathbf{x}^k[n]|\mathbf{y})$ — also increases during the interval of oscillatory behavior, though not enough to compensate for the increase in $R(\mathbf{x}^k[n])$. Thus, for this example the increase in $S(\mathbf{x}[n]|\mathbf{y})$ is due to an increase in $R(\mathbf{x}^k[n])$, not an increase in the synchronization between the two ensembles. The synchronization measure $T(\mathbf{x}[n,\eta]|\mathbf{y})$ and the phase synchronization (shown in Figures 2.10(b) and 2.10(c), respectively) reveal no interdependence between the two ensembles, as expected. In the next example we will not consider $S(\mathbf{x}[n]|\mathbf{y})$.

2.4.2 Simultaneous Bursts

We now consider the case where both ensembles respond to a stimulus, but in different ways. In this example, a high frequency burst of oscillatory activity occurs in $s^k[n]$ and a simultaneous low frequency burst of oscillatory

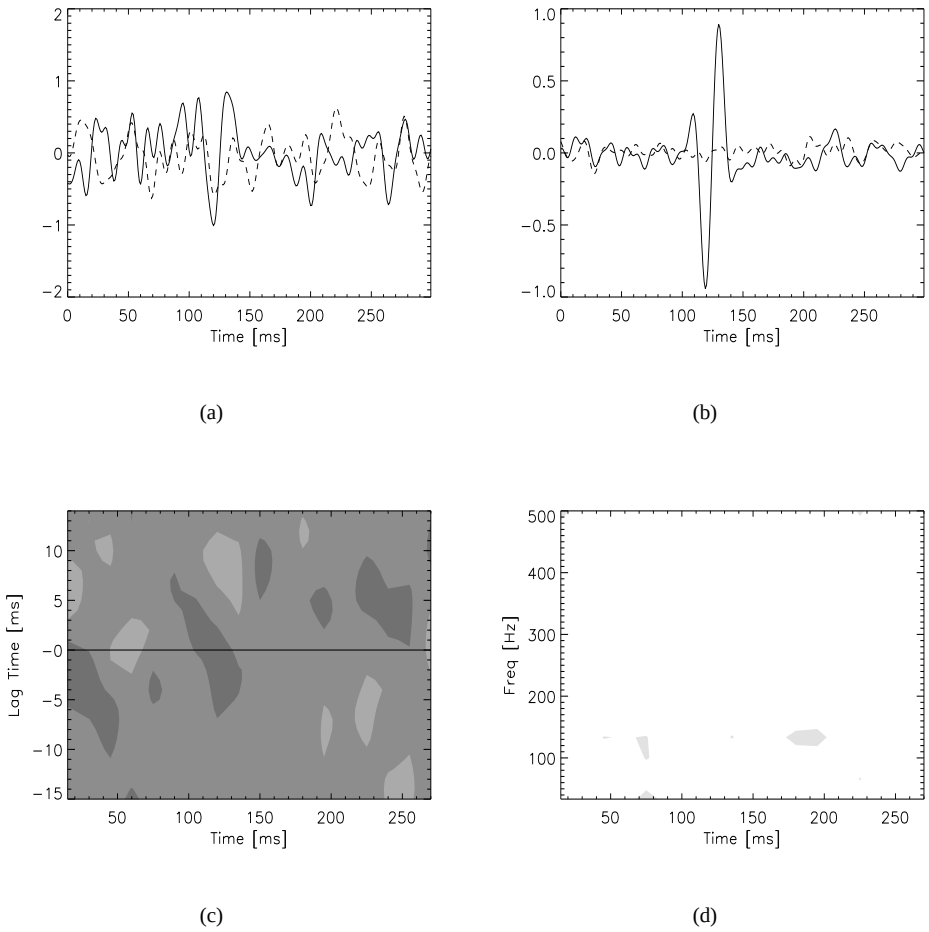

Figure 2.9: The ensembles of bursting data and noisy data, and the linear coupling measures. (a) A typical ensemble member from the oscillatory bursting data $s^k[n]$ (solid line) and the noisy data $r^k[n]$ (dashed line). The weak oscillatory response in $s^k[n]$ between 100 ms and 150 ms is hidden in the noise. (b) The ensemble averaged ERPs of ensemble s (solid line) and ensemble r (dashed line). The oscillatory response in ensemble s for 100 ms $< n <$ 150 ms is apparent. (c) The WCC between $s^k[n]$ and $r^k[n]$. The color scheme is the same as that used to create Figure 2.3(b). (d) The WC between $s^k[n]$ and $r^k[n]$. The color scheme is the same as that used to create Figure 2.3(c). We find the WC is near zero for all values of frequency and time. Both linear measures detect no coupling between the two ensembles.

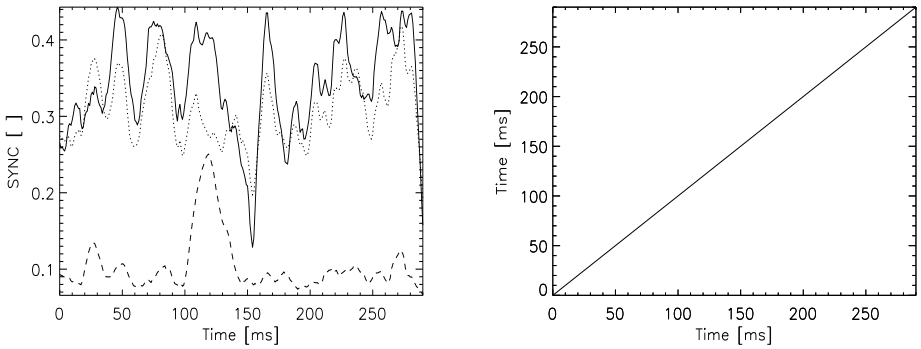

(a)

(b)

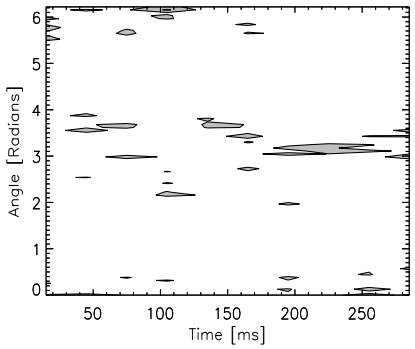

(c)

Figure 2.10: Synchronization measures applied to the burst versus noise system. (a) Three synchronization measures: $S(\mathbf{x}[n]|\mathbf{y})$ (dashed line), $H(\mathbf{x}[n]|\mathbf{y})$ (dotted line), and $N(\mathbf{x}[n]|\mathbf{y})$ (solid line). All three measures are smoothed over a window of size 11 ms at each time point. Both $H(\mathbf{x}[n]|\mathbf{y})$ and $N(\mathbf{x}[n]|\mathbf{y})$ fluctuate between 0.15 and 0.45 over the entire time interval and suggest no obvious synchronization between the ensembles, as expected. $S(\mathbf{x}[n]|\mathbf{y})$ increases during the interval 100 ms $< n <$ 140 ms, and therefore suggests an increased synchronization between the ensembles during this interval. This incorrect interpretation is a consequence of the increase in $R(\mathbf{x}^k[n])$ during the oscillatory burst, as explained in the text. (b) The time shifted synchronization measure $T(\mathbf{x}[n,\eta]|\mathbf{y})$. The plotting and color scheme are the same as that used to create Figure 2.5(b). The $T(\mathbf{x}[n,\eta]|\mathbf{y})$ result reveals no coupling between the ensembles. (c) The windowed phase synchronization. The plotting and color scheme are the same as that used to create Figure 2.5(c). This measure also reveals no coupling between the ensembles.

activity occurs in $r^k[n]$ for 100 ms $< n <$ 150 ms and each k. Sinusoidal noise is added to each $s^k[n]$ and $r^k[n]$ such that the SNR is approximately 2. A typical ensemble member pair ($s^k[n]$ solid line, $r^k[n]$ dashed line) is shown in Figure 2.11(a). The individual ensemble members in Figure 2.11(a) do not reveal the structure of the ERP, which is mostly hidden by the noise. Only after averaging an ensemble of these time series do the ERPs become apparent in Figure 2.11(b). From the ensemble averaged data, we conclude that both ensembles exhibit a nontrivial response. If this were observed ECoG data, we would conclude that both ensembles respond to the stimulus. We require that the coupling measures detect this type of relationship, in which both ensembles respond to a stimulus simultaneously, although at different frequencies.

We show in Figures 2.11(c) and 2.11(d) the WCC and WC, respectively. The WCC displays a moderate increase for 130 ms $< t <$ 140 ms and a time lag near -6 ms. From this result, we might conclude that the two ensembles are coupled and that $s^k[n]$ leads $r^k[n]$ by approximately 6 ms. This result is incorrect; we constructed $s^k[n]$ and $r^k[n]$ to oscillate simultaneously. We also note that other regions of moderate correlation exist in the figure (e.g., at 110 ms $< t <$ 130 ms and a time lag near 10 ms) and make the WCC results difficult to interpret. The second linear measure — the WC — exhibits two regions of strong coherence. Both occur for 100 ms $< t <$ 150 ms, one for low frequencies (less than 50 Hz) and the other for high frequencies (between 200 Hz and 500 Hz.)

To compute the synchronization between ensembles $s^k[n]$ and $r^k[n]$ we again choose $\tau = 1$ ms and $d = 10$ to reconstruct the state space vectors, $\mathbf{x}^k[n]$ and $\mathbf{y}^k[n]$ from $s^k[n]$ and $r^k[n]$, respectively. In Figure 2.12(a) we plot $H(\mathbf{x}[n]|\mathbf{y})$ (dotted line) and $N(\mathbf{x}[n]|\mathbf{y})$ (solid line). Both results fluctuate throughout the entire time interval and neither accurately captures the synchronization between the two ensembles. We show $T(\mathbf{x}[n,\eta]|\mathbf{y})$ for this example in Figure 2.12(b). The value of $T(\mathbf{x}[n,\eta]|\mathbf{y})$ is positive only for 100 ms $< n <$ 135 ms along both axes. Because the nonzero values of $T(\mathbf{x}[n,\eta]|\mathbf{y})$ lie near the diagonal, we correctly conclude that the time shift $\eta \approx 0$, and the coupling between $r^k[n]$ and $s^k[n]$ is simultaneous (i.e., the bursts in $r^k[n]$ and $s^k[n]$ occur simultaneously.) Finally, we show the phase synchronization in Figure 2.12(c). This measure displays no regions of strong coupling. Of the four synchronization measures applied in this example we may only use $T(\mathbf{x}[n,\eta]|\mathbf{y})$ to detect the interdependence between the two ensembles.

We note that, although the time intervals of synchronization displayed in Figure 2.12(b) are approximately correct, $T(\mathbf{x}[n,\eta]|\mathbf{y})$ is not large over the entire interval of the oscillatory bursts (i.e., for 100 ms $< t <$ 150 ms.) This is a consequence of the noise added to the time series. To illustrate this, we apply $T(\mathbf{x}[n,\eta]|\mathbf{y})$ to data identical to that analyzed in Figure 2.12(b) except that we set the SNR to approximately 100; here the data is nearly noiseless. We show the results in Figure 2.4.2. The rectangular region of synchronization measured by $T(\mathbf{x}[n,\eta]|\mathbf{y})$ occurs from 90 ms $< n <$ 150 ms in both $r^k[n]$ and $s^k[n]$. The reader may wonder why $T(\mathbf{x}[n,\eta]|\mathbf{y})$ detects synchronization beginning at 90 ms in $s^k[n]$ when the oscillatory burst in $s^k[n]$ starts at 100 ms. This is due to the phase space reconstruction

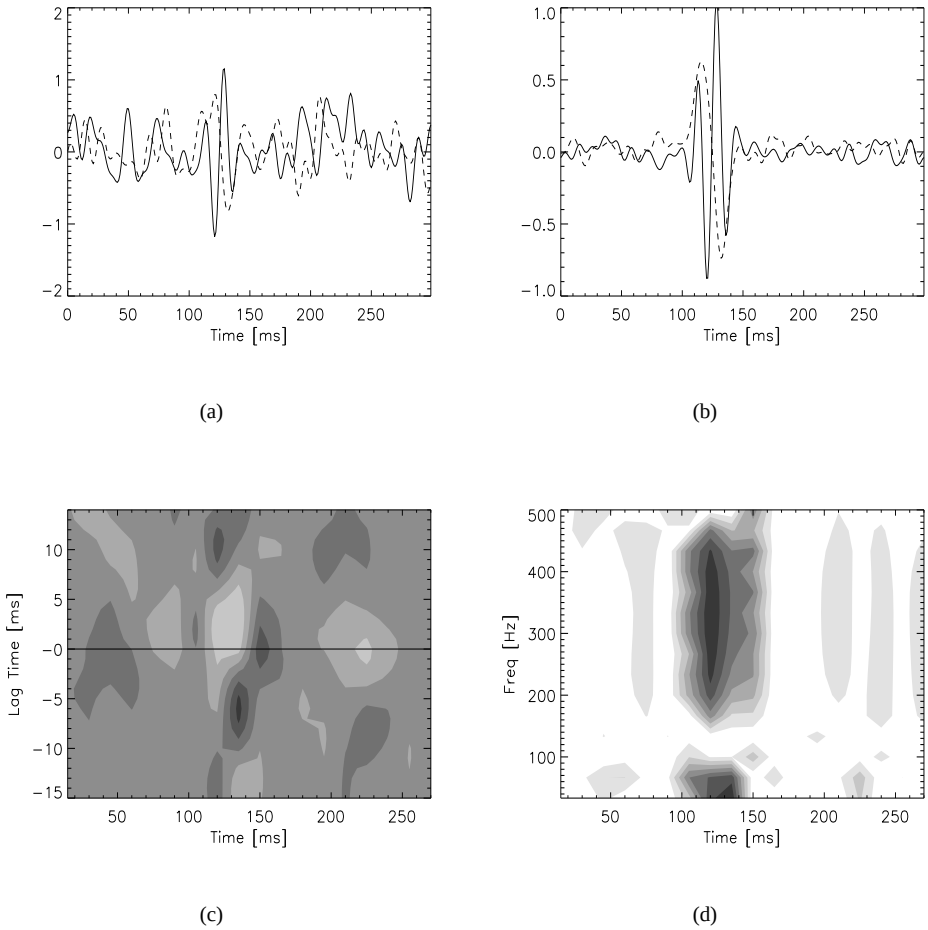

Figure 2.11: The ensembles of bursting data and the linear coupling measures. (a) A typical ensemble member pair from the oscillatory bursting data: $s^k[n]$ (solid line) and $r^k[n]$ (dashed line). The weak oscillatory responses of both time series are mostly hidden in the noise. (b) The ensemble averaged ERPs of $s^k[n]$ (solid line) and $r^k[n]$ (dashed line). The oscillatory bursts, hidden in the single ensemble member pair of (a), are revealed here in the ensemble averaged ERPs. (c) The WCC between $s^k[n]$ and $r^k[n]$. The color scheme is the same as that used to create Figure 2.3(b). The WCC detects moderate cross-correlation for 130 ms $< t <$ 140 ms and a time lag near -6 ms. (d) The WC between $s^k[n]$ and $r^k[n]$. The color scheme is the same as that used to create Figure 2.3(c). The WC detect strong coherence between $s^k[n]$ and $r^k[n]$ for 100 ms $< t <$ 150 ms.

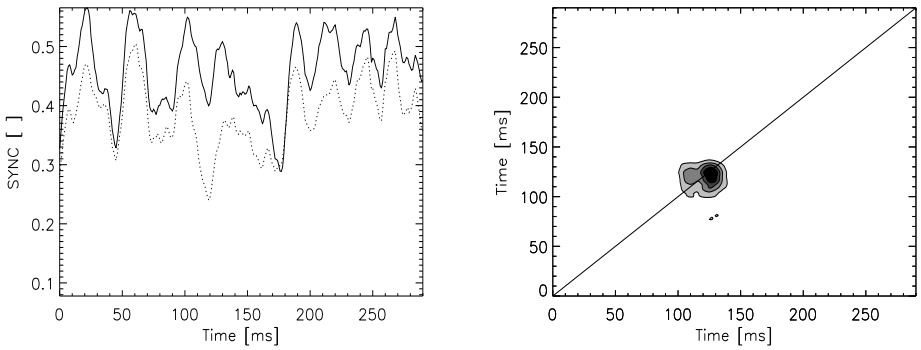

(a)

(b)

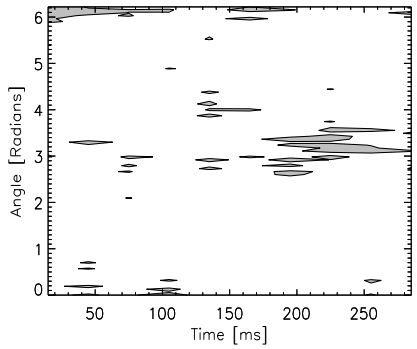

(c)

Figure 2.12: Synchronization measures applied to the ensembles of bursting data. (a) Two synchronization measures: $H(\mathbf{x}[n]|\mathbf{y})$ (dotted line), and $N(\mathbf{x}[n]|\mathbf{y})$ (solid line), smoothed over a window of size 11 ms at each time point. Neither $H(\mathbf{x}[n]|\mathbf{y})$ nor $N(\mathbf{x}[n]|\mathbf{y})$ accurately captures the synchronization between the two ensemble for 100 ms $< n <$ 160 ms. (b) The time shifted synchronization $T(\mathbf{x}[n,\eta]|\mathbf{y})$ applied to the ensemble of oscillatory bursting data of Figure 2.11(a). The plotting and color scheme are the same as that used to create Figure 2.5(b). This measure detects the synchronization between the two ensembles for 100 ms $< n <$ 135 ms in $s^k[n]$ (along the vertical axis) and for 100 ms $< n <$ 135 ms in $r^k[n]$ (along the horizontal axis). (c) The windowed phase synchronization. The plotting and color scheme are the same as that used to create Figure 2.5(c). This measure also reveals no coupling between the ensembles.

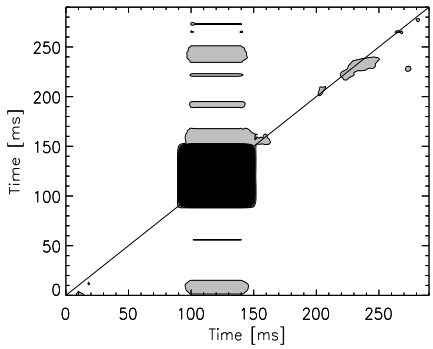

Figure 2.13: The synchronization measure $T(\mathbf{x}[n,\eta]|\mathbf{y})$ applied to the bursting ensembles of data with weak noise (SNR ≈ 100). The plotting and color scheme are the same as that used to create Figure 2.5(b). A region of strong synchronization occurs for 90 ms $< n <$ 150 ms in $r^k[n]$ along the horizontal axis and 100 ms $< n <$ 160 ms in $s^k[n]$ along the vertical axis.

we have used to create $\mathbf{x}^k[n]$ and $\mathbf{y}^k[n]$. For $\tau = 1$ and $d = 10$, $\mathbf{x}^k[n] = (s^k[n], s^k[n+1], \ldots, s^k[n+9])$; the vector $\mathbf{x}^k[n]$ depends upon $s^k[n]$ and future values of $s^k[n]$. Thus, although the oscillatory burst begins at $n = 100$ ms in $s^k[n]$, the effect of this burst on the reconstructed vector $\mathbf{x}^k[n]$ begins at $n = 100 - 9 = 91$ ms. Similarly for $r^k[n]$ and $\mathbf{y}^k[n]$. The effects of the phase space reconstruction must be considered when interpreting the synchronization results of experimental data.

We now summarize the results of our computer simulations. We have shown in Section 2.2 that the linear and nonlinear coupling measures can detect the interdependence of two nonlinear maps. In Section 2.3 we showed that, when a time lag occurs in the coupling, most of the measures fail. Only the synchronization measure $T(\mathbf{x}[n,\eta]|\mathbf{y})$ succeeded in detecting the coupling and the lead/lag relationship between the ensembles. Finally, in Section 2.4 we applied the coupling measures to bursting data inspired by EEG and ECoG recordings. In Section 2.4.1 we showed that $S(\mathbf{x}[n]|\mathbf{y})$ erroneously detects synchronization between two unrelated ensembles in one of which oscillatory bursts occur. In Section 2.4.2 we showed that $H(\mathbf{x}[n]|\mathbf{y})$, $N(\mathbf{x}[n]|\mathbf{y})$, and the phase synchronization fail to detect interdependence between two related ensembles in which bursts of oscillatory activity occur. The measure $T(\mathbf{x}[n,\eta]|\mathbf{y})$ is the only measure to behave correctly in the three examples we considered.

We do not wish to suggest that the WCC, WC, $S(\mathbf{x}[n]|\mathbf{y})$, $H(\mathbf{x}[n]|\mathbf{y})$, $N(\mathbf{x}[n]|\mathbf{y})$, and phase synchronization are poor coupling measures. The references in Section 2.1.1 have shown the utility of these synchronization methods applied to a variety of simulated and experimental data. Instead, we suggest that these measures are not appropriate to, say, compute the coupling between ensembles containing short, oscillatory bursts of activity. In the next section, we apply some of the coupling measures to time series collected in two observations and suggest how the coupling

measures are useful in inferring cortical connectivity.

2.5 Application: auditory ECoG ERP data.

Having described the coupling measures in Sections 2.1.2 and 2.1.3 and applied them to simulated data in Sections 2.2 - 2.4, we now apply them to data collected in an ECoG ERP experiment [34]. The ECoG data were recorded from an awake subject undergoing neurosurgery for tumor removal. The recordings were done in accordance with University of California, San Francisco (UCSF) and University of California, Berkeley (UCB) human subjects requirements and patient consent was obtained. Seven carbon ball electrodes (just under 3 mm in diameter) were placed on the left hemisphere around the posterior extent of the Sylvian fissure, near the known position of primary and secondary auditory cortices. Two epidural electrodes served as reference and ground for the differential amplifiers. The analog signals were bandpass filtered in the amplifier between 0.1 and 250 Hz, amplified by 10^4, and digitized at a sampling rate of 2003 Hz with 16 bit resolution. The data were subsequently high-pass filtered above 2.3 Hz using a symmetrical finite response filter and all epochs with detectable artifact were removed.

The stimuli consisted of short duration (180 ms) tones occurring at two different frequencies. During the experiment, the patient passively heard three, 210 s blocks of tones while watching a slide show. In the first and third blocks, 85% of the tones were at 500 Hz (*standards*) and 15% of the tones were at 550 Hz (*deviants*). Tones occurred at a rate of $\approx$ 2.5 Hz. In the second block, the standards were replaced by silences (i.e., only deviant tones occurred.) Traditional time-frequency analyses revealed cortical responses between approximately 25 ms and 250 ms from tone onset [6]. As expected from previous scalp EEG and animal studies, responses to standards were weak, responses to deviants were stronger, and responses to deviants only were strongest.

In the analysis that follows, we apply a coupling measure to three electrodes from the second block of tones (deviants only) in which the evoked responses were strongest. For convenience, we refer to the three electrodes as A, B, and C. We consider times 125 ms preceding the stimulus onset to 220 ms following the stimulus onset, choose $k' = 40$ ensemble members, and subtract the mean from each ensemble member. We do not average reference the data due to the small number (nine) of electrodes. Therefore, the shared reference electrode may artificially increase the coupling results. If this effect were important, we would expect all electrode pairs to show strong coupling for all time. We show below that the coupling results vary from strong to weak, and for some electrode pairs no coupling was detected. Therefore, we assume that the reference electrode only weakly effects the coupling results presented below.

Before applying the coupling measures, we illustrate the characteristics of the data collected at the three electrodes. In Figure 2.14(a) we show typical ensembles members recorded at electrodes A (solid curve), B (dashed curve) and C

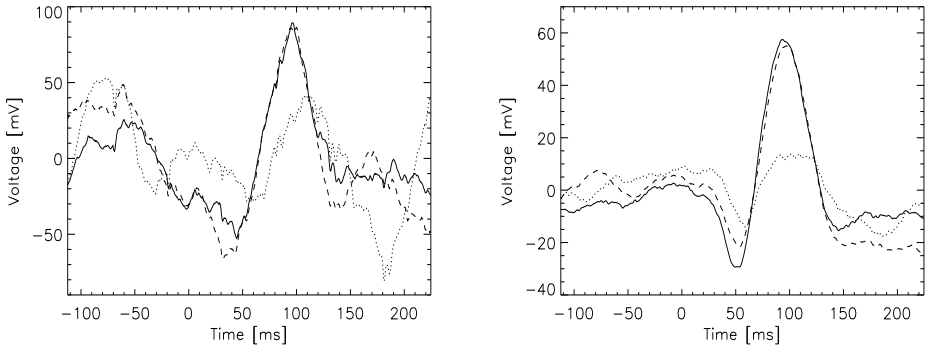

(a) (b)

Figure 2.14: ECoG data recorded in the ERP experiment at electrodes *A*, *B*, and *C*. In both figures we plot time (in ms) relative to stimulus onset along the horizontal axis and voltage (in mV) along the vertical axis. (a) Individual members of the first ensemble recorded at electrodes *A* (solid curve), *B* (dashed curve), and *C* (dotted curve). (b) The ensemble average results at electrodes *A* (solid curve), *B* (dashed curve), and *C* (dotted curve).

(dotted curve). The stimulus (i.e., the deviant tone) occurs at $t = 0$ ms. Inspecting the individual ensemble members shown in Figure 2.14(a), we cannot determine which electrodes record a response to the stimulus. In Figure 2.14(b) we show the ERPs averaged over the ensembles of measurements at each electrode. We note that for $t < 0$ the average voltages recorded at all three electrodes fluctuate around 0 mV. This result is expected; preceding the stimulus, the cortical electrical activity recorded at each electrode is seemingly random. Summing these random voltages over the ensemble, we find an average value near 0 mV. Following the stimulus, we find that all three electrodes exhibit a nonzero average response. We find that the responses recorded at electrodes *A* and *B* are similar; both decrease by approximately -20 mV near $t = 50$ ms and increase by approximately 80 mV for 50 ms $< t <$ 100 ms. We note that the average response at electrode *A* achieves a lesser minimum and greater maximum than that recorded at electrode *B*. We also find a weaker averaged response at electrode *C*; at this electrode the average response decreases by approximately -15 mV near $t = 50$ and increase by approximately 30 mV for 50 ms $< t <$ 100 ms.

Using the averaged responses shown in Figure 2.14(b) we may predict the coupling between the three electrodes. We interpret the similar responses of electrodes *A* and *B* to imply strong coupling. We could quantify this result by computing the cross-correlation between the two averaged responses. From the conclusion that *A* and *B* are strongly coupled, we may guess that these two electrodes possess a similar coupling relationship with electrode *C*. For example, if we find that electrodes *A* and *C* are strongly coupled, we might then expect that electrodes *B* and *C* are strongly coupled. We show in what follows that this intuition is incorrect.

We showed in Section 2.4 that for an ensemble of data consisting of oscillatory bursts, the synchronization measure $T(\mathbf{x}[n,\eta]|\mathbf{y})$ is the most accurate measure of coupling. The ECoG ERP data considered here consist of three ensembles (recorded at electrodes *A*, *B*, and *C*) of oscillatory, bursting data. Therefore, we choose to analyze the coupling between the three electrodes using the synchronization measure $T(\mathbf{x}[n,\eta]|\mathbf{y})$. We set σ_D in (2.14) to zero in what follows to obtain the most conservative measure of $T(\mathbf{x}[n,\eta]|\mathbf{y})$. In Figure 2.15(a) we show the synchronization measure $T(\mathbf{x}[n,\eta]|\mathbf{y})$ applied to the data recorded at electrodes *A* and *B*. The solid diagonal line denotes the location of zero time lag. The vertical and horizontal dashed lines denote the time of stimulus onset. From Figure 2.15(a) it is clear that electrodes *A* and *B* are synchronous. We note that *A* and *B* become strongly synchronous approximately 90 ms after the stimulus onset, and that the duration of the synchronization is longer in *A* than in *B*.

Next we show the synchronization between electrodes *C* and *A* in Figure 2.15(b). It is clear that *C* and *A* are synchronous although less so than *A* and *B*. The synchronization is elongated in time along the *C* direction, and the maximum synchronization occurs after the stimulus and below the diagonal: near 130 ms in *C* and 90 ms in *A*.

Finally in Figure 2.15(c) we show the synchronization $T(\mathbf{x}[n,\eta]|\mathbf{y})$ between electrodes *C* and *B*. In this case, the synchronization is very weak. Thus, we conclude from the measure $T(\mathbf{x}[n,\eta]|\mathbf{y})$ that electrodes *A* and *B* are strongly synchronous, *C* and *A* are weakly synchronous, and *C* and *B* are not significantly synchronous.

We can interpret these results in a qualitative manner consistent with the physiology of the human cortex. That the synchronization follows the stimulus onset in Figure 2.15(a) suggests the synchronization between electrodes *A* and *B* is induced by the stimulus. The area of maximum synchronization in Figure 2.15(a) occurs at a physiologically reasonable temporal location, approximately 90 ms after the stimulus onset, and the closeness of the synchronization maximum to the diagonal suggests that electrodes *A* and *B* are synchronous with zero time lag. We may therefore make the hypothesis that the stimulus activates the cortical regions below electrodes *A* and *B* simultaneously. This suggests that a common input — perhaps from other cortical areas or deeper brain regions — activates both cortical regions simultaneously. In this way we can begin to map the cortical pathway activated by a deviant auditory tone.

We present two more simulated examples similar to those in Section 2.4 to help interpret the synchronization results for electrodes *C* and *A*, and *C* and *B*. We begin by noting that experimental ERPs are not precisely time locked to the stimulus onset. Different paths of action potential propagation, changing states of the subject, and inherent experimental error will vary the time at which the ERPs occur. Although the time interval between the stimulus and the cortical response may vary, different cortical regions may still be strongly synchronous. In both simulated examples that follow, $s^k[n]$ consists of an oscillatory burst 50 ms in duration and centered at $n = 175$ ms, while $r^k[n]$ consists of an oscillatory burst 100 ms in duration, also centered at $n = 175$ ms. To each $s^k[n]$ and $r^k[n]$ we added sinusoidal noise such that the SNR=10.

To mimic the known variation in ERPs mentioned above, we consider two cases. In the first case, we include random time shifts (up to ± 20 ms) in the location of the oscillatory bursts. We do this in such a way that, for each k, the pair of ensemble members $s^k[n]$ and $r^k[n]$ are time shifted by the same amount and in the same direction. Thus, although the time series are not precisely time locked to the stimulus, they are precisely time locked to each other. For example, in the first ensemble ($k = 1$) the oscillatory burst in $s^1[n]$ and $r^1[n]$ may begin at 125 ms and 150 ms, respectively. For $k = 2$, the burst may begin at 115 ms and 140 ms. For $k = 3$, at 130 ms and 155 ms, and so on. In each case, the onset times of the bursts in $s^k[n]$ and $r^k[n]$ differ by 25 ms. We refer to this type of shifting as *uniform shifting*. In Figure 2.16(a) we show the synchronization measure $T(\mathbf{x}[n,\eta]|\mathbf{y})$ where $\mathbf{x}^k[n]$ and $\mathbf{y}^k[n]$ are the phase space reconstructions (with $\tau = 1$ and $d = 10$) of $s^k[n]$ and $r^k[n]$, respectively, and we have set $\sigma_D(\mathbf{x}^k[n+\eta])$ in (2.14) to zero. We note that the $T(\mathbf{x}[n,\eta]|\mathbf{y})$ result for this uniformly shifted simulated data, shown in Figure 2.16(a), is similar to the result for the experimental data shown in Figures 2.15(a) and 2.15(b); both results possess an elongated region of synchronization centered near zero time shift.

For the second case of simulated data, we again shift the oscillatory bursts in the time series $s^k[n]$ and $r^k[n]$ by random amounts (up to ± 10 ms.) But, in this example, we do not make identical time shifts for pairs of ensemble members. For example, in the first ensemble ($k = 1$), we may set the oscillatory bursts in $s^1[n]$ and $r^1[n]$ to begin at 125 ms and 150 ms, respectively. For $k = 2$, we may set the bursts to begin at 116 ms and 152 ms; for $k = 3$, 130 ms and 140 ms, and so on. Thus, the time series are neither time locked to the stimulus nor to each other. We refer to this type of shifting as *random shifting*. As above, we determine the phase space reconstructions $\mathbf{x}^k[n]$ and $\mathbf{y}^k[n]$ of $s^k[n]$ and $r^k[n]$, respectively, and we set $\sigma_D(\mathbf{x}^k[n+\eta])$ in (2.14) to zero. The synchronization measure $T(\mathbf{x}[n,\eta]|\mathbf{y})$ shown in Figure 2.16(b) reveals very weak synchronization between the two randomly shifted ensembles. Here, $T(\mathbf{x}[n,\eta]|\mathbf{y})$ allows one to draw the correct conclusion — if the two times series are neither time locked to the stimulus nor to each other, they are only weakly dependent. The two ensembles of time series are not independent because both time series respond to the stimulus at approximately the same time. This simulated result shown in Figure 2.16(b) is consistent with the weak synchronization found between electrodes C and B and shown in Figure 2.15(c).

The qualitative reasoning and simple simulations suggest the following conclusions. The strong synchronization between electrodes A and B may be due to simultaneous or uniformly shifted ERPs — this electrode pair may be driven by a common source. The weak synchronization between electrodes C and B may be due to randomly shifted ERPs; although both electrodes respond to the stimulus, they do so in an unrelated way. Finally, the intermediate synchronization between electrodes C and A may be due to a combination of uniform shifting and small, random shifting. Thus, this electrode pair may be weakly driven by a common source. In this way, we use the synchronization measure $T(\mathbf{x}[n,\eta]|\mathbf{y})$ to establish a crude model of cortical connectivity between the three cortical regions observed with the three electrodes. In the next section, we apply three synchronization measures to scalp EEG data collected

from patients diagnosed with a type of dementia. We use the results to infer changes in cortical connectivity associated with the disease.

2.6 Application: discrimination between healthy and demented subjects

The most common form of dementia, Alzheimer's disease (AD), affects 4.5 million people in the U.S [35]. At present, no cure for AD exists, although some medications may delay memory decline or treat behavioral and emotional symptoms [36]. The primary treatment for AD is supportive care provided both to patients and their families. In 1991, the costs of treating AD in America were estimated to exceed 85 billion dollars, and are expected to increase dramatically during the next 25 years [37].

Although prevalent, AD is difficult to diagnose. The gold standard for diagnosis occurs post-mortem when an autopsy reveals neurofibrillary tangles or neuritic plaques in the cortex and hippocampus. The clinical diagnosis of AD is often accurate (in greater than 80% of cases,) yet the similarity of symptoms expressed in AD and other forms of dementia and depression often hinders the diagnosis [38]. In addition, physicians must diagnose patients intermediate between cognitively normal elderly individuals and those with dementia [36]. This intermediate zone is referred to as mild cognitive impairment (MCI) and patients diagnosed with MCI are 5-10 times more likely to develop dementia [36]. That MCI symptoms often precede AD suggests the possibility of detecting AD before its complete onset. Early detection of AD would provide individuals more time to make special arrangements, and perhaps allow future preventative treatments to be administered.

The scalp EEG reveals changes in cortical electrical activity associated with normal aging, MCI, and AD. The most established of these EEG diagnostic techniques analyze changes in the power spectrum. Many researchers have found that AD patients exhibit increased power in the θ ($\approx 1-4$ Hz) and δ ($\approx 4-8$ Hz) frequency bands, and decreased power in the α ($\approx 8-12$ Hz) and β ($\approx 13-28$ Hz) frequency bands compared to healthy controls [38, 39, 40]. This "slowing" of the EEG occurs across the scalp with a nearly uniform distribution. Recently researchers have shown that measures adopted from dynamical systems theory, such as the correlation dimension, reveal decreased complexity of EEG traces from AD patients [41, 42].

Both the power spectrum and correlation dimension are computed from EEG data collected at individual electrodes; these two measures reveal changes in the spatially localized voltage produced near each electrode. Coupling measures, on the other hand, reveal changes in the interdependence of EEG data recorded at two different electrodes. For example, in Section 2.1.2 we defined the ensemble averaged linear coherence between two time series. Researchers have applied linear coherence measures to EEG data and found that patients diagnosed with AD often exhibit a lower

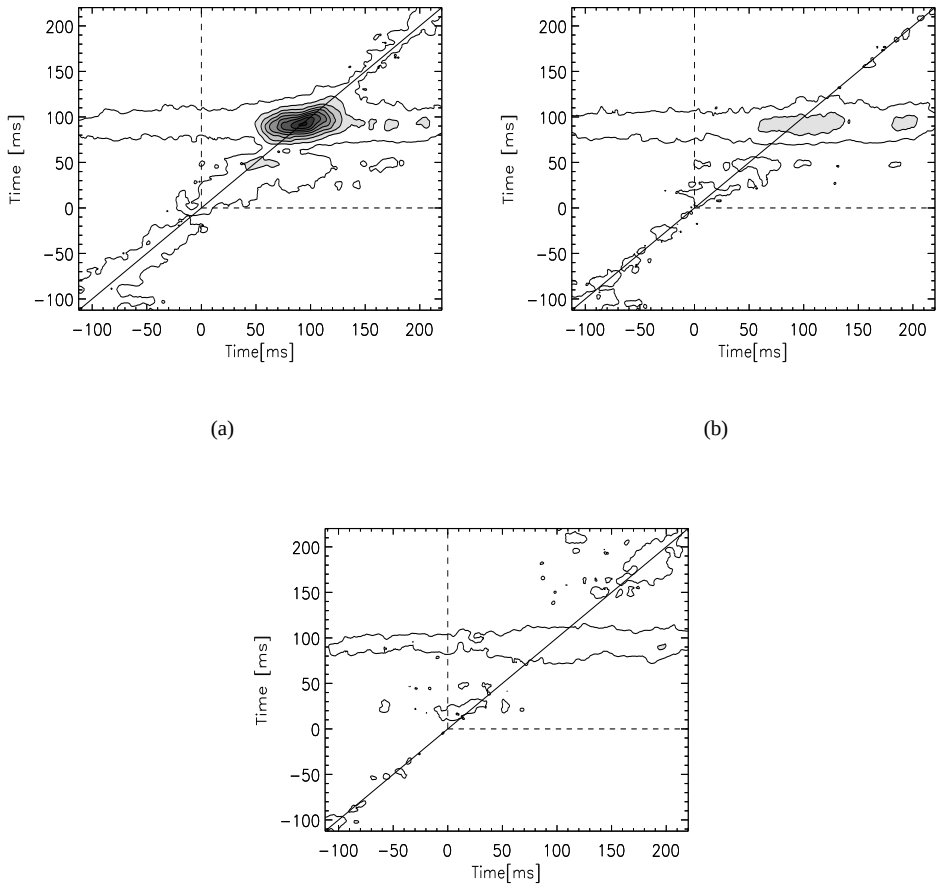

(a)

(b)

(c)

Figure 2.15: The synchronization measure $T(\mathbf{x}[n,\eta]|\mathbf{y})$ applied to the three electrodes pairs: (a) *A* versus *B*, (b) *A* versus *C*, and (c) *B* versus *C*. $T(\mathbf{x}[n,\eta]|\mathbf{y})$ was smoothed over a two-dimensional window of size 11 at each time point. The solid diagonal line corresponds to the location of zero time lag. The horizontal and vertical dashed lines correspond to the time of stimulus onset. For this figure there are 10 evenly spaced contour levels from 0.01 (white) to 0.19 (black). Note the region of strong synchronization from 40 ms $< n <$ 130 ms in *A* and 60 ms $< n <$ 110 ms in *B*. The synchronization measure $T(\mathbf{x}[n,\eta]|\mathbf{y})$ applied to electrodes *C* and *A* from the ECoG ERP experimental data. Note that the synchronization is elongated in *C* and is weaker than the synchronization between electrodes *A* and *B*. (b) The synchronization measure $T(\mathbf{x}[n,\eta]|\mathbf{y})$ applied to electrodes *C* and *B* from the ECoG ERP experimental data. Note that the synchronization is weaker than the synchronization between the other electrode pairs.

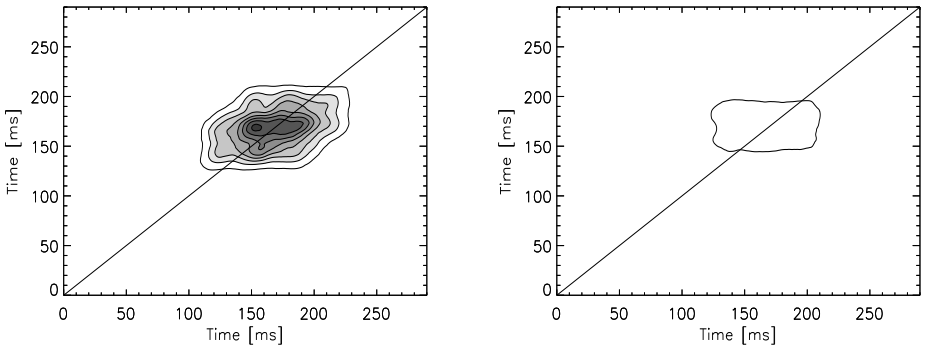

(a) (b)

Figure 2.16: The synchronization measure $T(\mathbf{x}[n,\eta]|\mathbf{y})$ applied to shifted simulated data. In both figures, $T(\mathbf{x}[n,\eta]|\mathbf{y})$ was smoothed over a two-dimensional window of size 11 at each time point. The solid diagonal line in both figures corresponds to the location of zero time lag. For both figures there are ten evenly spaced contour levels from 0.01 (white) to 0.19 (black). (a) The synchronization measure $T(\mathbf{x}[n,\eta]|\mathbf{y})$ applied to uniformly shifted simulated data. The ensembles s and r consist of oscillatory bursts with the same center time. The oscillatory bursts in each ensemble member pair $s^k[n]$ and $r^k[n]$ are shifted in time by the same amount, up to ± 20 ms, and in the same direction. (b) The synchronization measure $T(\mathbf{x}[n,\eta]|\mathbf{y})$ applied to randomly shifted simulated data. The ensembles s and r consist of oscillatory bursts with the same center time. The oscillatory bursts in each ensemble member pair $s^k[n]$ and $r^k[n]$ are shifted in time by different amounts, up to ± 10 ms, and in different directions.

coherence between electrode pairs than healthy controls [43]. These decreased coherence values are typically localized in both frequency and location (e.g., decreased frontal cortex coupling and central cortex coupling in the θ, α, and β bands [44], decreased temporofrontal coupling and temporoparietal coupling in the α band [40], decreased temporal lobe coupling in the α band [45].) Recent measures of nonlinear coupling — as we discussed in Section 2.1.3 — have been applied to EEG data collected from healthy, MCI, and AD subjects. In [46] the authors apply a synchronization measure to EEG data collected from these three subject groups and find that cortical interactions from AD patients decrease in the β band compared to healthy controls.

Here we collaborate with Dr. F. L. Chang at the Fort Wayne Neurological Center, and Drs. D. Hudson and M. Cohen at UCSF-Fresno to study resting scalp EEG collected from 20 individuals clinically diagnosed to have either no dementia (7 healthy controls, ages 62 ± 14 years, we denote as H), MCI (5 subjects, ages 71 ± 5 years), or AD (8 subjects, ages 81 ± 6 years.) In Section 2.6.1 we discuss the clinical diagnosis of these conditions and the data collection procedure and in Section 2.6.2 we apply three synchronization measures to the EEG data. We show that the synchronization between EEG time series recorded at electrodes O1 and O2 — above the left and right occipital lobes, respectively — provides a quantitative means to discriminate AD subjects from healthy and MCI subjects. In Section 2.6.4 we discuss how the results suggest changes in cortical connectivity.

2.6.1 Clinical Diagnosis and Data Collection

Each subject was assigned a clinical diagnosis by a team of physicians at the Fort Wayne Neurological Center. These diagnoses were based on clinical assessments, neuropsychological tests, psychometric tests, and a medical history. As part of the assessment, scalp EEG data were collected from each subject. These data are recorded using the standard 10-20 electrode configuration and a sampling rate of 256 Hz. During the data collection, typically lasting 30 minutes, each subject was instructed to relax and close his or her eyes. Deviations from this behavior, such as eye movements or sleep, were noted and the associated time intervals were omitted from further analysis. In what follows we analyze these EEG data in accordance with UCB human subjects guidelines.

2.6.2 Methods of Analysis

The goal of the analysis is to provide a concise, quantitative measure capable of distinguishing between AD, MCI, and healthy subjects from the scalp EEG data. To do so, we apply three synchronization measures to the EEG data and determine the nonlinear coupling between time series recorded at two, neighboring electrodes. In this subsection, we describe the preprocessing of the data and the manipulations we perform on the results of the three synchronization

measures. We apply these measures to the data in Section 2.6.3.

We start the analysis by choosing two neighboring electrodes (O1 and O2, say) from one subject. For convenience, we label the time series recorded at the two electrodes $x[t]$ and $y[t]$ where $t = \{0, \ldots, T\}$ is the time index, and T is the total number of data points collected. We note that to derive the time (in seconds) from the time index, we multiply t by the sampling interval $1/256$ s. The preprocessing of $x[t]$ and $y[t]$ consists of three steps. First, we average reference the data with respect to the remaining 19 electrodes; we do not include omitted electrodes (e.g., electrodes that lost electrical contact with the scalp) in the average reference procedure. Second, we bandpass digital filter the data between 1 Hz and 50 Hz, subtract the mean from each electrode, and scale the data to have a maximum absolute value of one. Third, we divide $x[t]$ and $y[t]$ into 120, consecutive, one second intervals (256 index points per interval). We choose these intervals from simultaneous segments of $x[t]$ and $y[t]$. For example, if we choose the first segment in $x[t]$ from $256 \leq t \leq 511$, then the first segment in $y[t]$ is from $256 \leq t \leq 511$. We label the data in each interval chosen in this way from $x[t]$ and $y[t]$ as $x^i[t]$ and $y^i[t]$, respectively. We note that the superscript i denotes the i^{th} interval. Finally, we label the data from $x[t]$ and $y[t]$ referenced, filtered, fixed zero mean, scaled, and divided into intervals, as $\tilde{x}^i[t]$ and $\tilde{y}^i[t]$, respectively. In this way, we create an ensemble of measurements. We note that the ensembles constructed here differ from those analyzed in Section 2.5. In that section, the data collection procedure dictated the ensemble; we referenced the zero time of each ensemble member to the stimulus onset. For the EEG data of interest in this section, we extract the data from a continuous time series without time referenced to a stimulus onset.

To determine the coupling between the ensembles $\tilde{x}^i[t]$ and $\tilde{y}^i[t]$ we apply three different synchronization measures defined in Section 2.1.3. The advantage of synchronization measures over traditional techniques of time series analysis (such as the linear coherence results in [43, 44, 40, 45]) is that synchronization measures detect nonlinear coupling between two time series. A measure of nonlinear interdependence may be especially important when studying complicated systems, such as the electrical activity produced by the human cortex. It is reasonable to assume that, because of the nonlinear processing of single neurons and the high density of cortical connections, the EEG does possess a nonlinear component, (i.e., the EEG cannot be modeled only as a collection of independent oscillators or modes [47].) To apply these ideas, we must also assume that the EEG is the result of a low dimensional, deterministic process [24]. Without these assumptions, we may still apply the synchronization measures to characterize the EEG signal. As in Section 2.5 we do not interpret the results in terms of low dimensional dynamical systems; instead we apply the synchronization measures to discriminate between the healthy, MCI, and AD subjects.

In what follows we apply the three synchronization measures $S(x|y)$, $H(x|y)$, and $P(\theta)$ to the data. To compute $S(x|y)$ or $H(x|y)$, we first embed the data $\tilde{x}^i[t]$ and $\tilde{y}^i[t]$ from interval i. The embedding procedure creates d-dimensional vectors $\tilde{X}^i[t]$ and $\tilde{Y}^i[t]$ from the 1-dimensional vectors $\tilde{x}^i[t]$ and $\tilde{y}^i[t]$, respectively. To construct $\tilde{X}^i[t]$ and $\tilde{Y}^i[t]$ we must

determine the delay time τ and the embedding dimension d. Here we do not compute the AMI to find τ nor the percentage of false nearest neighbors to find d. Instead, we compute $S(x|y)$ and $H(x|y)$ for different values of d and τ and show that the results are invariant. In [42] and [41], the authors follow a similar procedure and compute the correlation dimension for different values of d and τ. For the third measure, we compute the phase synchronization $P(\theta)$ between $\tilde{x}^i[t]$ and $\tilde{y}^i[t]$ for all intervals i. We note that, for this measure, we do not embed the data.

The result of applying two of the measures — $S(x|y)$ and $H(x|y)$ — to $\tilde{x}^i[t]$ and $\tilde{y}^i[t]$ is the synchronization as a function of time t and interval i. To provide a concise diagnostic measure of dementia, we make two assumptions regarding the stationarity of the synchronization results. First, we assume that within each one second interval the synchronization between $\tilde{x}^i[t]$ and $\tilde{y}^i[t]$ remains approximately constant. We may then average the synchronization values over time t for fixed i. Second, we assume that the synchronization results are stationary over the 120 intervals, and therefore average the synchronization results across intervals i. Both stationarity assumptions are likely invalid — the electrical activity of the cortex constantly changes in response to input from, for example, environmental stimuli and the thalamus. But, we show below that these assumptions do not prevent the goal of this work: to discriminate between healthy, MCI, and AD subjects. The final result is two scalar values representing the averaged $S(x|y)$ and $H(x|y)$ results for each subject. For the third measure, we average $P(\theta)$ over all intervals and over phases θ between 0.3 and -0.3. Here we again assume stationarity of the synchronization result over the intervals. The final result is a scalar value representing the average (over time and angles) $P(\theta)$ for each subject.

2.6.3 Data Analysis

Having defined the three measures, we now apply each to the EEG data. We illustrate the results with two examples. First, we apply the three synchronization measures to the data collected at electrodes O1 and O2, located near the left and right occipital lobes, respectively. We show that two measures — $S(x|y)$ and $H(x|y)$ — produce similar results and significant (or near significant) separation between healthy and AD subjects for different embedding parameters d and τ. We note that the third measure $P(\theta)$ is independent of the embedding parameters. Second, we fix the embedding parameters $d = 10$ and $\tau = 1$, and compute the synchronization between electrodes P3 and P4 using each of the measures. In this case, we find no significant separation between the conditions. We find, but do not show, similar insignificant separation between the three subject groups for three other pairs of interhemispheric electrodes: C3 and C4, F3 and F4, and FP1 and FP2. We conclude that the AD subjects show decreased synchronization between the left and right occipital lobes compared to the healthy and MCI subjects.

We start with the application of the synchronization measures to the EEG data collected at electrodes O1 and O2. We show the results for the embedding parameters $d = 10$ and $\tau = 1$ in Figure 2.17. For each of the three

synchronization measures ($S(x|y)$, $H(x|y)$, and $P(\theta)$) we plot the results for the three subject groups (H, MCI, and AD.) We indicate the mean value for each subject group and condition with an asterisk, and the standard deviation by the vertical lines extending above and below each asterisk. We also list the synchronization values and standard deviations in Table 2.1. We note that the three synchronization measures illustrated in Figure 2.17 produce similar results. Specifically, we find that the average synchronization value for the healthy subjects exceeds the average synchronization value for the AD subjects. The separation between these two values is statistically significant (t-means test $p < 0.05$) for two measures: $H(x|y)$ and $P(\theta)$. We indicate this significant separation by drawing a small horizontal line one standard deviation *above* the mean values for the healthy and AD subjects. We note that the separation is near significance ($p = 0.08$) for $S(x|y)$. We also find that the average synchronization for the MCI subjects is less than that of the healthy subjects and greater than that of the AD subjects. These differences are not statistically significant except for the separation between the MCI and AD subjects computed with $H(x|y)$. We indicate this significant separation by drawing a small horizontal line one standard deviation *below* the mean values for the MCI and AD subjects.

In Figure 2.18 we show the synchronization measures $S(x|y)$ and $H(x|y)$ computed with different embedding parameters d. Here we fix $\tau = 1$ and plot the synchronization results for $d = 4$ (in squares and dotted lines,) $d = 10$ (in asterisks and solid lines — as in Figure 2.17,) and $d = 16$ (in diamonds and dashed lines.) We find that, compared to the $d = 10$ results, the mean values of $S(x|y)$ decrease for $d = 4$ and increase for $d = 16$, while the values of $H(x|y)$ increase for $d = 4$ and decrease for $d = 16$. Yet the trend — that the average synchronization values for the healthy controls exceeds those of the MCI subjects which exceeds those of the AD subjects — is preserved. We find for both embedding parameters $d = 4$ and $d = 16$ that the average synchronization values for the healthy subjects exceeds the average synchronization values for the AD subjects. This separation is significant for both $S(x|y)$ and $H(x|y)$ with $d = 4$, and only for $H(x|y)$ with $d = 16$. We indicate this significant separation by drawing a small horizontal line one standard deviation *above* the mean values for the healthy and AD subjects. We note that the separation between the healthy and AD subjects is near significance ($p = 0.09$) for $S(x|y)$ with $d = 16$. As for the $d = 10$ case, the separation between the MCI and AD subjects is statistically significant only for $H(x|y)$. We indicate this significant separation by drawing a small horizontal line one standard deviation *below* the mean values for the MCI and AD subjects. Thus, we may discriminate between the healthy and AD subjects with the synchronization measures $S(x|y)$ and $H(x|y)$, and the MCI and AD subjects with $H(x|y)$ using the embedding parameters $d \in \{4, 10, 16\}$ and $\tau = 1$.

We now perform a similar analysis for the embedding parameter τ. Here we fix $d = 10$ and plot in Figure 2.19 the synchronization results for $\tau = 1$ (in asterisks and solid lines — as in Figure 2.17,) $\tau = 4$ (in squares and dotted lines,) and $\tau = 8$ (in diamonds and dashed lines.) We find that, as τ increases, the values of $S(x|y)$ increase and the values of $H(x|y)$ decrease. For $\tau = 4$, the separation between the healthy and AD subjects is significant for both measures, and the separation between the MCI and AD subjects is significant only for $H(x|y)$. For the $\tau = 8$ case, the separation

between the healthy and AD subjects is significant for both measures, and the separation between the MCI and AD subjects is significant only for $S(x|y)$. In this case, the $H(x|y)$ result is near significance: $p = 0.06$. We indicate these significant separation following the prescription we use to create Figure 2.18. We note that the trend illustrated in Figures 2.17 and 2.18, that the average synchronization values for healthy controls exceeds those for the MCI subjects which exceeds those for the AD subjects, is violated for $\tau = 8$. In this case, the average synchronization values for the MCI subjects exceeds those of the healthy controls. We conclude that the synchronization measures $S(x|y)$ and $H(x|y)$ discriminate between the healthy and AD subjects, and the MCI and AD, subjects for d near 10 and τ near 1. In what follows, we fix $d = 10$ and $\tau = 1$.

In Figure 2.20 we show the synchronization results computed for the EEG data collected at electrodes P3 and P4. We plot these results in the same way as those shown in Figure 2.17. For this interhemispheric electrode pair, we find no significant differences in the synchronization results for the three subject conditions. We find, but do not show, similar results when we compute the synchronization between electrodes: C3 and C4, F3 and F4, and FP1 and FP2. None of these electrode pairs possess significant differences in coupling between the three subject conditions. We conclude that the only interhemispheric electrodes with significant synchronization differences between the healthy and AD, and MCI and AD conditions, are electrodes O1 and O2.

Table 2.1: The value and standard deviation of the synchronization between electrodes O1 and O2 averaged over subject groups. We mark the statistically significant separations ($p < 0.05$) between the healthy and AD subjects, and the MCI and AD subjects with an asterisk ($*$) and double asterisk ($**$), respectively.

	$S(x\|y)$	$H(x\|y)$ [$*$, $**$]	$P(\theta)$ [$*$]
H	0.35 ± 0.08	0.37 ± 0.08	0.27 ± 0.10
MCI	0.31 ± 0.04	0.36 ± 0.02	0.19 ± 0.13
AD	0.28 ± 0.05	0.25 ± 0.08	0.15 ± 0.5

Table 2.2: The value and standard deviation of the synchronization between electrodes P3 and P4 averaged over subject groups. There are no statistically significant differences.

	$S(x\|y)$	$H(x\|y)$	$P(\theta)$
H	0.23 ± 0.04	0.19 ± 0.05	0.12 ± 0.05
MCI	0.23 ± 0.02	0.21 ± 0.07	0.15 ± 0.09
AD	0.21 ± 0.04	0.16 ± 0.02	0.13 ± 0.13

2.6.4 Discussion

In Section 2.6.3 we applied three synchronization measures to EEG data collected from three subjects groups: healthy controls, patients diagnosed with MCI, and patients diagnosed with AD. We showed that the synchronization between the EEG data recorded at electrodes O1 and O2 decreased for the AD subjects compared to the healthy controls. This decrease was significant for two of the measures — $H(x|y)$ and $P(\theta)$ — and near significance for

$S(x|y)$. We computed the $S(x|y)$ and $H(x|y)$ measures with different embedding parameters and showed that the results are robust. Finally, we reported no significant differences in the synchronization values measured at other interhemispheric electrode pairs (e.g., P3 and P4) for the three subject groups.

The methods of analysis we present differ from those used in previous studies. Here we employ measures of nonlinear coupling that operate in the time domain. A common coupling measure for the study of AD is the coherence — a linear measure that operates in the frequency domain. Linear coherence analysis (and some nonlinear synchronization analysis, as in [46]) reveals the coupling between EEG data within different frequency bands. Here, we bandpass filter the EEG time series between 1 Hz and 50 Hz, and apply the three synchronization measures to the data within this wide frequency range. Therefore, we cannot use the synchronization results to determine changes in coupling confined to specific frequency intervals. Instead we consider the nonlinear coupling between the EEG data throughout many frequency bands.

We may interpret the results in Section 2.6.3 in terms of the disconnection model of AD. To do so, we use the synchronization results to infer changes in cortical connectivity. For example, we showed that the synchronization between EEG data recorded at electrodes O1 and O2 decreased significantly for AD subjects compared to healthy controls. We infer from this result a decreased functional connectivity, or disconnection, between between the left and right occipital lobes. Such changes in functional connectivity may occur in many ways. At the cortex, the death of pyramidal neurons and the associated cortico-cortical connections decreases functional connectivity. In subcortical regions, the loss of white matter decreases functional connectivity. In this study, we infer a disconnection only between the left and right occipital lobes. We do not detect losses in functional connectivity between other interhemispheric regions.

We note that the synchronization results do not indicate the physiological changes associated with decreased interdependence between the left and right occipital lobes. One method to identify these physiological changes may be a post-mortem examination. Such examinations are the gold-standard for the diagnosis of AD. In this study, no post-mortem examinations were performed. Thus an uncertainty results both in the clinical diagnosis and in the interpretation of the synchronization results. Most studies that distinguish between MCI and AD suffer from this limitation. In the future synchronization measures, combined with traditional linear measures (e.g., power spectra and linear coherence), may provide physicians with additional diagnostic tools perhaps as reliable as the current gold-standard.

Another method to identify the physiological changes associated with a decreased synchronization may be the development of a mathematical model. For example, given a mathematical model of human cortical electrical activity, one may find that a decrease in a particular model parameter (the number of synaptic connections between neurons,

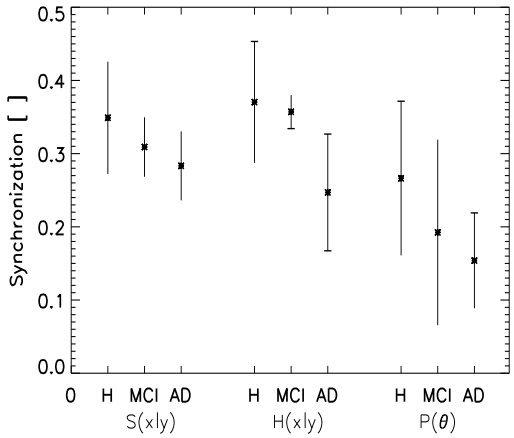

Figure 2.17: The synchronization values for the three measures $S(x|y)$, $H(x|y)$, and $P(\theta)$ between electrodes O1 and O2 averaged over the three subject groups: healthy (H), mild-cognitive impairment (MCI), and Alzheimer's disease (AD). We plot the results for the three synchronization measures $S(x|y)$, $H(x|y)$, and $P(\theta)$ in the left, center, and right of the figure, respectively. We indicate the average synchronization values by asterisks and the standard deviation within each subject group by vertical lines above and below each asterisk. The synchronization values and standard deviations are also listed in Table 2.1. We indicate statistically significant ($p < 0.05$) separations between the H and AD values by drawing a small horizontal line one standard deviation *above* the mean synchronization values for the healthy and AD subjects. We indicate statistically significant ($p < 0.05$) separations between the MCI and AD values by drawing a small horizontal line one standard deviation *below* the mean synchronization values for the MCI and AD subjects.

say) results in a decreased synchronization of the model dynamics. Comparing this synchronization result with those determined from scalp EEG data, one may find that the two agree. If so, one may then associate the decreased synchronization observed in the EEG data with a change in a model parameter (here, a change in the number of synaptic connections.) In this way the mathematical model serves to relate the observed data to a physiological change.

Unfortunately, a mathematical model of human cortical electrical activity that can mimic the progression of AD does not exist. At best, the current mathematical models can approximate only the simplest cases of cortical activity. Two of these simple cases represent pathological brain states: the transition to unconsciousness induced by anesthesia and seizures. In the next chapter, we describe a mathematical model of the latter.

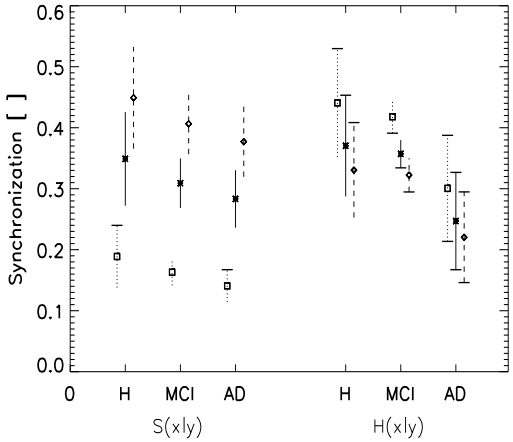

Figure 2.18: The synchronization values $S(x|y)$ and $H(x|y)$ computed for different embedding parameters between electrodes O1 and O2 averaged over the three subject groups: healthy (H), mild-cognitive impairment (MCI), and Alzheimer's disease (AD). Here we fix $\tau = 1$ and set $d \in \{4, 10, 16\}$. We indicate the mean values and standard deviations for $d = 4$ by squares and dotted lines, respectively; for $d = 10$ by asterisks and solid lines, respectively; and for $d = 16$ by diamonds and dashed lines, respectively. We indicate statistically significant separations between the healthy and AD subjects, and the MCI and AD subjects in the same way as that used to create Figure 2.17.

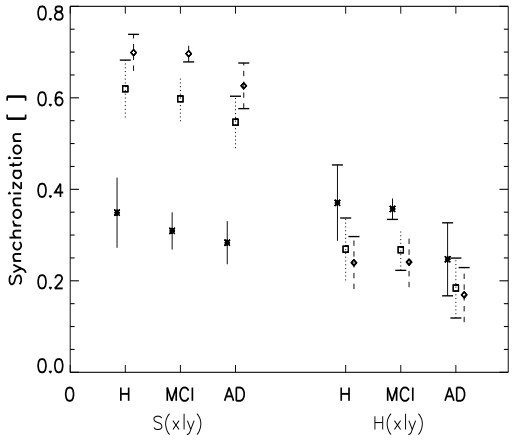

Figure 2.19: The synchronization values $S(x|y)$ and $H(x|y)$ computed for different embedding parameters between electrodes O1 and O2 averaged over the three subject groups: healthy (H), mild-cognitive impairment (MCI), and Alzheimer's disease (AD). Here we fix $d = 10$ and set $\tau = \{1, 4, 8\}$. We indicate the mean values and standard deviations for $\tau = 1$ by asterisks and solid lines, respectively; for $\tau = 4$ by squares and dotted lines, respectively; and for $\tau = 8$ by diamonds and dashed lines, respectively. We indicate statistically significant separations between the healthy and AD subjects, and the MCI and AD subjects in the same way as that used to create Figure 2.17.

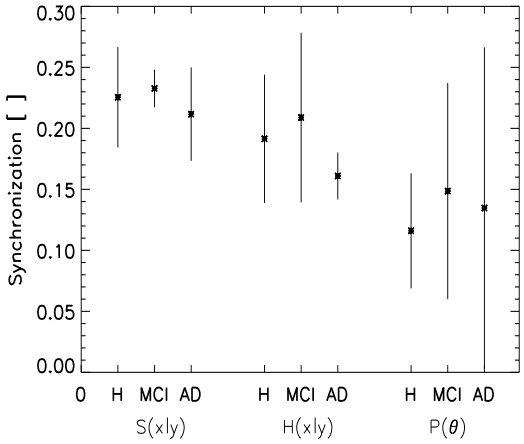

Figure 2.20: The synchronization values between electrodes P3 and P4 averaged over the three subject groups: healthy (H), mild-cognitive impairment (MCI), and Alzheimer's disease (AD). We plot the results for the three synchronization measures $S(x|y)$, $H(x|y)$, and $P(\theta)$ in the left, center, and right of the figure, respectively. For the three measures, we find no statistically significant separations between the three subject groups.

Chapter 3

Model

3.1 Introduction

In Chapter 2 we applied measures of linear and nonlinear coupling to EEG and ECoG data. We interpreted the results to infer connectivity changes between cortical regions and to develop crude models of cortical interactions. However, we could only speculate how these coupling results related to physiological changes within the cortex. For example, in Section 2.5 we could not relate the change in synchronization between two cortical regions to, say, a change in the density of synaptic connections in the cortex. To connect the EEG and ECoG data (and its analysis) to the physiology of the cortex, we develop a mathematical model.

In this chapter, we describe a mathematical model of the mesoscopic electrical activity recorded at the human cortex. We employ a recently developed continuum model of cortical electrical activity, which consists of a system of stochastic partial differential equations (SPDEs.) We use this model to help us understand a pathological instance of cortical electrical activity: that recorded during seizure. We choose to model the electrical activity of the seizing human cortex for three reasons. First, during a seizure, the cortex enters an organized state in which many neurons act in unison. We find an analysis of this organized state simpler than that of the typical "disorganized" cortex. Second, physicians often record ECoG data from epileptic subjects before performing resective surgery. Thus, observational data to compare with the model are available. Third, the electrical activity of the seizing cortex (although poorly understood) has been studied for decades. Therefore, numerous other models exist to which we can compare the dimensionless SPDEs.

The organization of this chapter is as follows. In Section 3.2 we discuss ictal ECoG data recorded from four

epileptic subjects [48, 49]. In Section 3.3 we define the model equations — the dimensionless SPDEs we utilize here — and the variable of principal interest: the excitatory mean soma potential h_e. In Section 3.4 we consider a simplified version of the SPDEs that possesses neither spatial variance nor stochastic input; we call this system the dimensionless ordinary differential equations (dimensionless ODEs). In Sections 3.4.1 and 3.4.2 we compute bifurcation diagrams for the dimensionless ODEs at two different parameter values. We show that in both cases oscillatory activity (as expected during a seizure) occurs. For typical parameter values, the oscillatory activity is unstable and short-lived. For other parameter values (which may be consistent with the seizing cortex) the oscillatory activity is stable and long-lived. In Section 3.5 we analyze the complete dimensionless SPDEs. We show how results from this system agree with results from the simpler dimensionless ODEs, and that traveling wave solutions exist. In Section 3.6 we compare the model solutions with the ECoG recordings, and show that the two agree in two important ways during seizure. We conclude that, for certain parameter values, the dimensionless SPDEs are a valid model of the electrical activity of the seizing human cortex. In Section 3.7 we show three methods for controlling and aborting seizure-like oscillations in the model, and finally in Section 3.8 we illustrate other parameter changes that make the model "seize" [50, 49]. Some material in this chapter is reprinted with permission from M. A. Kramer, H. E. Kirsch, and A. J. Szeri, Journal of the Royal Society Interface, 2, 113-127, 2005.

3.2 Observational Data: ECoG Seizure Recordings

The cellular mechanisms of a seizure have been extensively studied and some general microscopic characteristics have been deduced [51]. Preceding a seizure, thousands of individual neurons in the seizure focus (the brain region where a seizure begins, also known as the epileptogenic zone) undergo depolarization shifts followed by an afterhyperpolarization. As long as this behavior is confined to the seizure focus, there may be no clinical manifestation (although this synchronous activity can be detected as an interictal spike or a sharp wave in the EEG or ECoG.) Gradually, as the seizure develops, the magnitude of the afterhyperpolarization decreases and individual neurons generate nearly continuous action potentials. The inhibition surrounding the seizure focus weakens, the seizure spreads to other cortical neurons, and a clinical seizure occurs. Here we will not consider this microscopic behavior of individual neurons. Nor will we consider ictogenesis (the initiation of the seizure, which may occur in deeper brain regions.) Instead, we investigate the mesoscopic characteristics of seizure activity on the cortical surface as made manifest in subdural ECoG recordings.

Large amounts of ECoG data are often recorded from the seizing cortex (i.e., ictal data) as part of clinical care of patients with intractable epilepsy. These patients — whose seizures do not respond well to drug treatments — may

undergo surgery to remove a region of cortex that is believed to contain the seizure focus. Such resective surgery offers a chance to eliminate or ameliorate the seizures. In the process of planning such surgery, clinicians must accurately locate the seizure focus and identify any surrounding areas of functional cortex that should be preserved to minimize post-operative deficits. If necessary, in order to define the seizure focus more precisely with respect to structural and functional anatomy, clinicians may implant subdural electrodes on the brain surface for extended time periods (typically one week) in order to obtain recordings during seizures and locate the seizure onset. The electrodes are placed over the region of cortex suspected to contain the seizure focus based on: 1) semiologic features of the patient's seizures (i.e., the observable features of the seizure, such as eye deviation or limb jerking), 2) scalp EEG recordings made during typical seizures, 3) abnormalities observed in the ECoG recorded intraoperatively at the time of electrode implantation (i.e., interictal recordings), or 4) abnormalities seen on brain images. After the electrodes are implanted and the patient experiences his or her typical seizures, physicians locate the seizure focus through visual analysis of the ECoG recordings and formulate the surgical plan.

In subsections 3.2.1 - 3.2.4 we consider ictal ECoG data collected from four human subjects. Each subject suffered from intractable epilepsy and underwent electrode implantation as part of his or her care at the University of California, San Francisco (UCSF) Epilepsy Center. For each subject, a surgeon implanted one or two 8×8 electrode grids (10 mm spacing in the vertical and horizontal directions) and one or two 6-electrode subdural strips (also 10 mm spacing.) All electrodes were 4 mm diameter platinum-iridium discs embedded in a 1.5 mm thick silastic sheet with 2.3 mm diameter exposed surfaces and 10 mm spacing between the discs. To observe multiple seizures, physicians recorded ECoG data continuously at 400 Hz for several days from each subject, and seizing intervals were identified by a board-certified neurologist. In all cases, UCSF and UCB human subjects guidelines were observed.

We begin the analysis of the ECoG data in Section 3.2.1. In this section, we introduce the methods of analysis we use to calculate two quantities of interest: f_0 the frequency of maximum power during seizure, and v the speed of electrical potential propagation across the cortex during seizure. We compute these quantities for each of the four subjects, and in Section 3.6 we compare these observational results with identical quantities derived from the mathematical model.

3.2.1 Subject 1

The first subject we consider — Subject 1 — is a 49 year old male who had medically refractory complex partial seizures that began with staring and manual automatisms and frequently generalized into convulsions. Prior scalp EEG recordings had suggested that his seizures originated in the right temporal lobe, but MRI showed left mesial temporal sclerosis, raising the possibility that his seizures arose from the left temporal lobe instead. In order to better

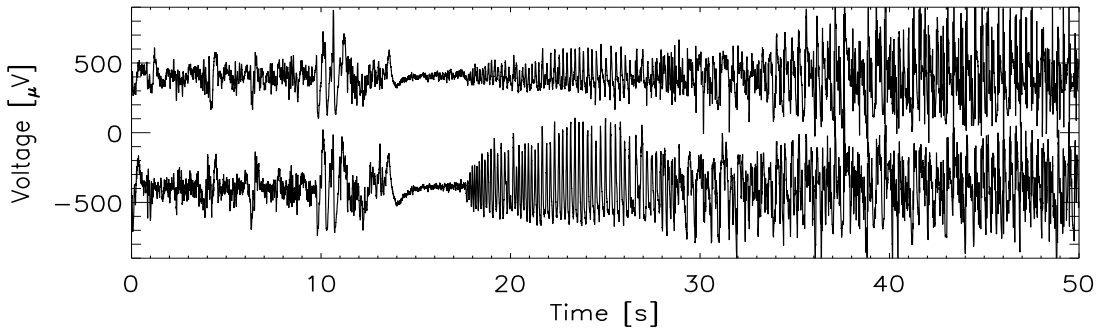

(a)

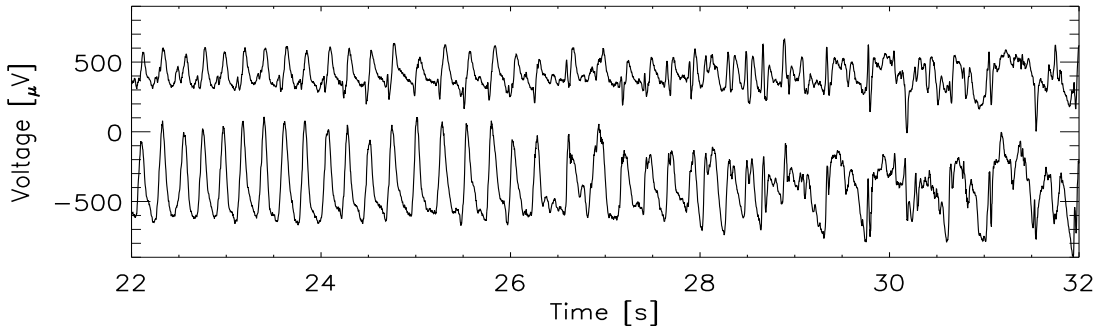

(b)

Figure 3.1: ECoG data recorded from Subject 1 at two neighboring subdural electrodes (separated by 10 mm) located on the surface of the right lateral frontal lobe. We label the time series X (lower trace in each figure) and Y (upper trace in each figure). To ease visual comparison we subtract 400 μV from X and add 400 μV to Y. (a) Here we show 50 s of ECoG activity recorded at two electrodes. There are three regions of ECoG activity: normal ECoG activity (0 s $< t <$ 14 s), followed by voltage suppression (14 s $< t <$ 17.5 s), and seizure ($t >$ 17.5 s). (b) Here we show the data from (a) for 22 s $< t <$ 32 s. We note that initially oscillations in X and Y have the same shape, and that oscillations in X are of larger magnitude and appear to precede those in Y. For $t >$ 27 s the relationship between X and Y becomes more complicated.

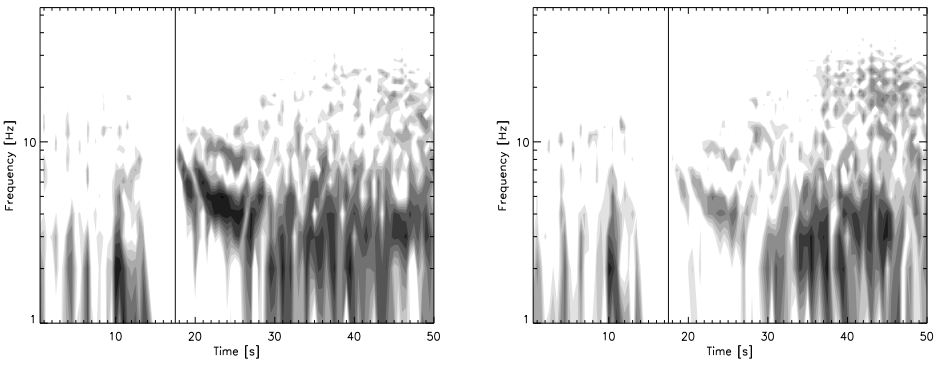

(a) (b)

Figure 3.2: The windowed power spectra (WPS) for the two ECoG time series shown in Figure 3.1. Here subfigures (a) and (b) correspond to the time series X and Y in Figure 3.1, respectively. The WPS are plotted in logarithmic greyscale with black and white denoting regions of high power (greater than 30 μV^2) and low power (less than 0.03 μV^2), respectively. The vertical line in the figure at $t = 17.5$ s denotes the approximate onset of seizure.

lateralize seizure onset, subdural and depth electrodes were implanted, with subdural electrode strips placed over the left and right lateral frontal regions and the left and right subtemporal regions. In addition bilateral hippocampal depth electrodes were placed, though we will not discuss these hippocampal recordings here. After electrode implantation, the subject was brought to the video-telemetry unit, where his antiseizure medications were slowly withdrawn. ECoG data were recorded continuously at 400 Hz from all electrodes for five and a half days. During this time, observations of eight typical seizures were captured. These recordings were of good quality and were determined, based on clinical review by board-certified clinical neurophysiologists, to show seizure onset from right medial temporal regions, with a pattern characteristic of seizures arising from this region. The subject went on to have a right anterior temporal lobectomy based on these clinical data.

ECoG epochs containing six of the subject's seizures were extracted from the clinical record. (Two of the seizure data files were corrupted and no longer available for extraction.) In Figure 3.1 we show ECoG data leading up to and during a seizure recorded at two neighboring subdural electrodes above the right lateral frontal region. We refer to the time series recorded at these two electrodes as X (lower curve) and Y (upper curve). The ECoG data shown in this figure possess three notable features. First, we observe that large amplitude voltage oscillations occur during the seizure ($t > 17.5$ s). We determine the frequency of these oscillations by computing the windowed power spectrum (WPS) of X and Y. To compute the WPS we partition the 50 s of data plotted in Figure 3.1 into 100 overlapping windows of 1.0 s duration and 0.5 s overlap. For example, the first window includes data for 0.0 s $\leq t \leq$ 1.0 s, the

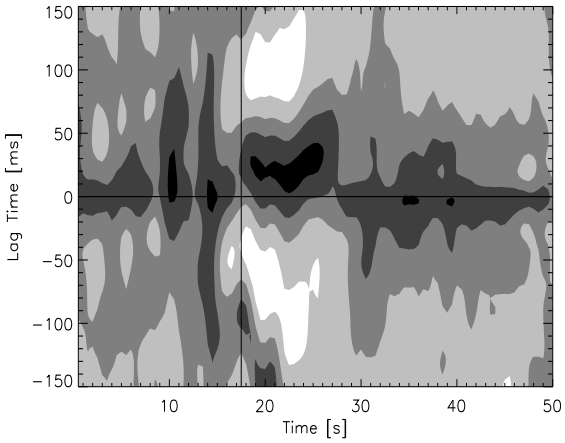

Figure 3.3: The windowed cross correlation between the two ECoG time series shown in Figure 3.1. The WCC are plotted in linear greyscale with regions of strong correlation (greater than 0.8) and anticorrelation (less than -0.8) denoted by black and white, respectively. The vertical line in the figure at $t = 17.5$ s denotes the approximate onset of seizure. The horizontal line in the figure denotes the zero lag.

second 0.5 s $\leq t \leq$ 1.5 s, the third 1.0 s $\leq t \leq$ 2.0 s, and so on. We then multiply the data in each window by the Hanning function and compute the power spectrum. We plot the WPS results for X and Y in Figures 3.2(a) and 3.2(b), respectively. The horizontal axis in each figure corresponds to the center times of the windows, and the solid vertical line to the time of seizure onset. We note, in the seconds preceding the seizure, the suppression of power at both electrodes for all frequencies below 55 Hz. After seizure onset, the regions of largest power occur at frequencies between 1 Hz and 10 Hz. The second notable feature in the observed data is the abrupt transition from normal ECoG activity (for $t < 14$ s) to seizing activity (for $t > 17.5$ s). This can be observed both in the original time series data (Figure 3.1(a)) and in the WPS (Figure 3.2). Lastly, we find that the oscillations recorded at the two electrodes are slightly out of phase. One may deduce this conclusion directly from Figure 3.1(b); we note that peaks in the oscillations in X (lower trace) appear to precede those in Y (upper trace) until $t \approx 29$ s. At this point, the relationship between the two time series becomes more complicated. To determine how the phase relationship between these two electrodes changes over time, we utilize a linear coupling measure defined in Section 2.1.2: the windowed cross correlation (WCC). In a manner similar to the WPS calculation, we partition the data into overlapping windows, and compute the cross correlation between X and Y in each window. We show the results in Figure 3.3. Following seizure onset (denoted by the vertical line in the figure) two regions of strong correlation occur: the first from 17.5 s $< t <$ 27 s, and the second from 28 s $< t <$ 50 s. In the first region, X leads Y (i.e., the lag time is positive) while in the second region, X lags Y (i.e., the lag time is negative but near zero).

To compare the observed ECoG data with the model solutions we use the WPS and WCC results to compute two quantities: 1) the average frequency at which the power spectrum achieves its maximum during seizure, and 2) the average speed at which the voltage peaks propagate between two subdural electrodes during seizure. We denote these quantities f_0 (the peak frequency) and v (the propagation speed), respectively. Here we discuss the computation of f_0 and v for Subject 1. We apply the same computations to determine f_0 and v for the other three subjects in Sections 3.2.2 - 3.2.4.

To determine f_0, we consider data collected at the same two subdural electrodes (e.g., X and Y) for each of six seizures recorded from Subject 1; part of one such seizure is shown in Figure 3.1. We first low pass filter the ECoG data X and Y below 55 Hz, and then compute the WPS. For example, in Figure 3.2(a) we show the WPS for the time series X recorded during a typical seizure. In this case the maximum power occurs between 1 Hz and 10 Hz following seizure onset (at $t \approx 17.5$ s). We then calculate the average frequency of maximum power in the WPS for the duration of the seizure (here, for 17.5 s $< t <$ 50 s.) Finally, we average this frequency of maximum power over the seizures (in this case, six.) We define this quantity — averaged over time and each seizure as f_0. We list f_0 and its standard deviation for both electrodes (i.e., X and Y) from Subject 1 in the second column of Table 3.1. We find for f_0 the values 4.1 ± 0.1 Hz and 4.8 ± 0.2 Hz, for X and Y, respectively.

Table 3.1: The average frequency of maximum power f_0 and average propagation velocity v in I1 and I2 for the ECoG time series data recorded from Subject 1 during seizure. We label the neighboring electrodes X and Y. We compute v from Y to X. To compute the uncertainty in the average, we assume the uncertainties in f_0 and v for each seizure are independent and random and propagate the uncertainties in the standard way.

ELECTRODE	f_0 [Hz]	v from b in I1 [m/s]	v from b in I2 [m/s]
X	4.1 ± 0.1	—-	—-
Y	4.8 ± 0.2	0.5 ± 0.1	-3 ± 1

Propagating waves of electrical activity have been observed in numerous mammalian systems and during seizures in rats and in cats [52, 53, 54]. Here we assume that, during each seizure, voltage peaks propagate between the two neighboring subdural electrodes (with time series X and Y.) That this assumption is valid can be inferred from the data shown in Figure 3.1(b). We note for 17.5 s $< t <$ 27 s the similarity of the wave forms in X and Y and that peaks in X precede peaks in Y. To determine the average propagation speed v of these voltage peaks, we first low pass filter the time series below 55 Hz. We then compute the WCC between X and Y, as shown in Figure 3.3. At each time in the WCC, a maximum correlation occurs for some lag time. For example, at $t = 20$ s, the maximum correlation occurs at a lag of approximately 25 ms. We compute this lag at which the maximum correlation occurs for the duration of the seizure. We find that, in general, the lag values are consistent over two temporal intervals. The first interval includes the time of seizure onset and the ten seconds that follow. The second includes all later times (i.e., all times ten seconds after the seizure onset until seizure termination.) For the data shown in Figure 3.3 the two time intervals over which

the lag of maximum correlation is consistent are: I1 = 17.5 s $< t <$ 27 s, and I2 = 28 s $< t <$ 50 s. Such intervals can be chosen for five seizures of Subject 1. For the sixth seizure, the lag values of maximum correlation are near zero for all times following seizure onset. Therefore, we do not include this seizure in our analysis of v. We determine v in each interval by dividing the known electrode separation (10 mm) by the average lag in each interval and averaging this velocity over the (in this case, five) seizures. We list v and its standard deviation for Subject 1 in the third and fourth columns of Table 3.1. We note that for one seizure the average lag is 0 ms in I2 and therefor v is infinite. We exclude this result from the calculation of v in I2. We find for v the values 0.5 ± 0.1 m/s and -3 ± 1 m/s, in I1 and I2, respectively. In the next three subsections, we use the techniques applied here to compute f_0 and v for three additional subjects. We summarize these results and compare them to similar quantities determined from the mathematical model in Section 3.6.

3.2.2 Subject 2

In this section, we analyze ECoG data recorded from a 28 year old man. To help localize the seizure focus before performing resective surgery, physicians implanted an 8×8 electrode grid over the left frontotemporal region and two, 6-electrode subdural strips curled under the left anterior and left posterior temporal lobe. ECoG data, recorded continuously for 15 days, captured two subclinical seizures. Both seizures arose from the proximal ends of the subtemporal strips.

To compare the observational and model results we follow the procedure in Section 3.2.1 to determine f_0 and v. For Subject 2 we analyze ECoG data recorded from one region of seizure initiation identified by the physicians; namely, we consider the three most proximal electrodes on the subdural strip that traverses the inferior aspect of the temporal lobe with the most distal end approximating the parahippocampal gyrus. For convenience, we label these neighboring electrodes a, b, and c, with c the most proximal of the three. We begin the analysis by bandpass filtering the data between 1.0 Hz and 55.0 Hz, and then computing the WPS for each electrode. We illustrate these WPS results for the second subclinical seizure in Figure 3.4. Subfigures (a), (b), and (c) correspond to electrode labels a, b, and c, respectively. Here we plot power in logarithmic grey scale with powers greater than 50 μV^2 in black and less than 0.3 μV^2 in white. We show time in seconds along the horizontal axis and frequency in Hertz along the vertical axis. This subclinical seizure begins at $t = 15$ s; we denote this time with a (red) vertical line in each subfigure. The subclinical seizure continues until $t = 49$ s; we denote the end of the subclinical seizure with a (red) vertical line in each subfigure. We find that of the three electrodes the middle electrode — shown in Figure 3.4(b) — displays the most power (i.e., the darkest regions) during the subclinical seizure. We also note the abrupt decreases in power below 50 Hz both preceding and following the subclinical seizure.

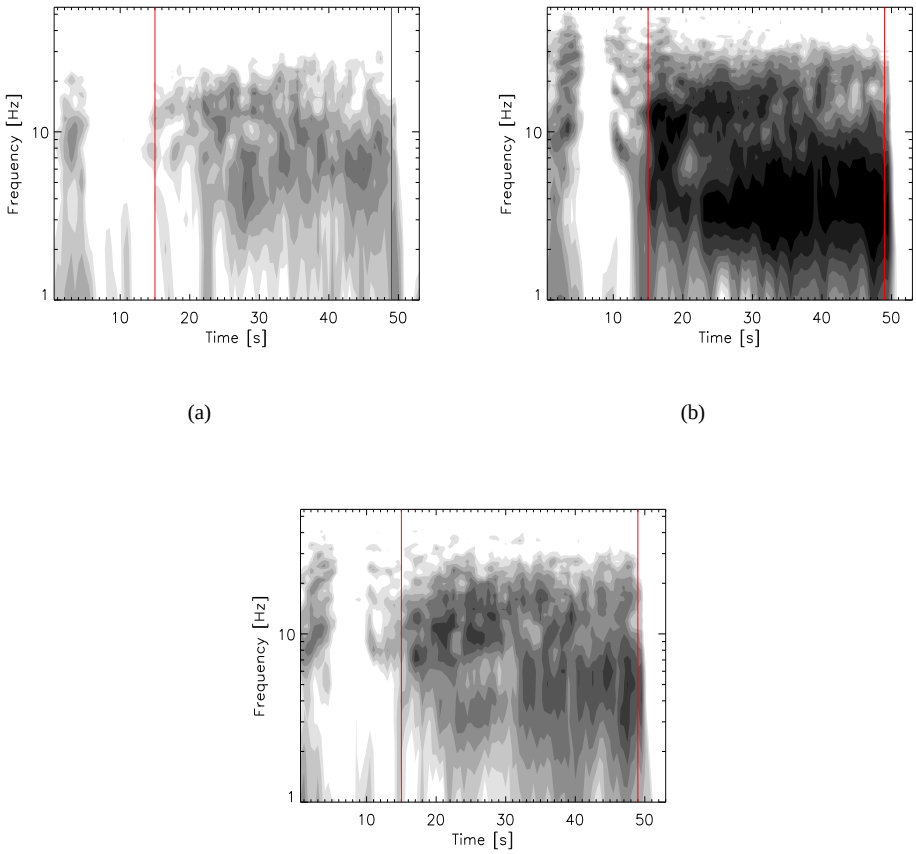

Figure 3.4: The windowed power spectra (WPS) for three ECoG time series recorded during the second subclinical seizure of Subject 2. Subfigures (a), (b), and (c) correspond to neighboring electrodes along a subdural strip with (c) the most proximal. The WPS are plotted in logarithmic greyscale with black and white denoting regions of high power (greater than 50 μV^2) and low power (less than 0.3 μV^2), respectively. For the purpose of visual presentation, we smooth the WCC results with a boxcar average of size 1.5 s in time and 3 Hz in frequency. The vertical (red) lines at $t = 15$ s and $t = 49$ s denote the approximate beginning and end of the seizure. We compute the frequency of maximum power at each electrode between the two vertical lines.

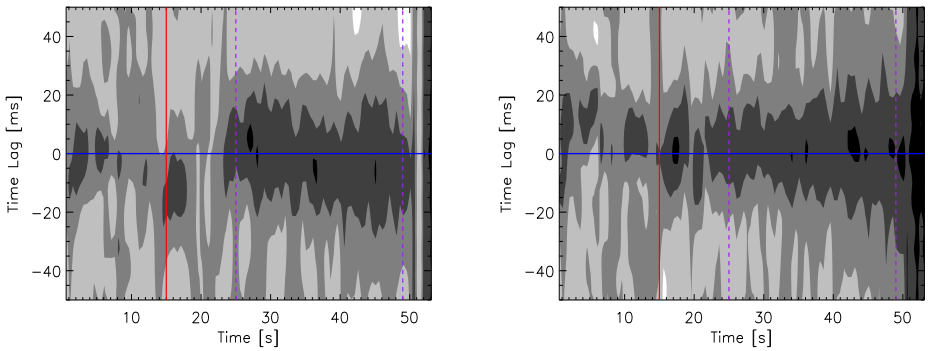

(a) (b)

Figure 3.5: The windowed cross correlation (WCC) between the ECoG time series recorded from the second subclinical seizure of Subject 2. We show in subfigures (a) and (b) the WCC between electrodes *b* and *a*, and *b* and *c*, respectively. The WCC are plotted in linear greyscale with regions of strong correlation (greater than 0.8) and anti-correlation (less than -0.8) denoted by black and white, respectively. We denote the seizure onset with a solid vertical (red) line and the interval I2 between the dashed vertical (purple) lines. The (blue) horizontal line in the figure denotes the location of zero lag.

To compute f_0, we determine the average frequency of maximum power during the subclinical seizure. We briefly discuss this procedure for the most proximal electrode whose WPS we show in Figure 3.4(c). We start by locating the time interval of the subclinical seizure, here 15 s $< t <$ 49 s, between the vertical (red) lines in the figure. At each time point within this interval, we locate the frequency of maximum power. For example, near $t = 25$ s, we find the maximum power occurs at 13 Hz. We then average these frequencies of maximum power determined at each time point over the duration of the seizure and for the two subclinical seizures. The result is f_0. We repeat this calculation for the other two electrodes and list these results in the second column of Table 3.2. We find that the mean values for f_0 lie between 5.2 Hz and 8.1 Hz with a maximum uncertainty in the mean of 0.4 Hz.

Table 3.2: The average frequency of maximum power f_0 and average propagation velocity v in I1 and I2 for the ECoG time series data recorded from Subject 2 during his two subclinical seizures. We label the neighboring electrodes *a*, *b*, *c*, with *c* most proximal. We compute v from the middle electrode *b*. To compute the uncertainty in the average, we assume the uncertainties in f_0 and v for each seizure are independent and random and propagate the uncertainties in the standard way. For comparison, we list the approximate values for f_0 and v determined from the mathematical model in the last row [48].

ELECTRODE	f_0 [Hz]	v from *b* in I1 [m/s]	v from *b* in I2 [m/s]
a	7.6 ± 0.3	-0.6 ± 0.2	-1.7 ± 0.7
b	5.2 ± 0.3	—	—
c	8.1 ± 0.4	7 ± 12	3.4 ± 0.6
Model	~ 10	~ 2	~ 2

The second quantity we determine is the speed of wave propagation v between the middle electrode b and its two neighboring electrodes a and c. To do so, we first bandpass filter the data between 1.0 Hz and 55.0 Hz. We then compute the WCC between electrodes b and a, and b and c. We show the results for the second subclinical seizure in Figure 3.5 where we plot the WCC between b and a, and b and c in Figures 3.5(a) and 3.5(b), respectively. In each figure we plot the correlation as a function of time (in s) and time lag (in ms), and indicate the seizure onset with a vertical (red) line, and the location of zero lag with a horizontal (blue) line. We show the correlation in linear grey scale, with black denoting regions of correlation greater than 0.8 and white denoting regions of anti-correlation less than -0.8. We found in Section 3.2.1 that two intervals of wavelike character occurred in the ECoG data recorded from that subject. The first — I1 — began at seizure onset and lasted for 10 s. The second — I2 — began 10 s after seizure onset and ceased at seizure termination. The same appears to be true here. From Figure 3.5(a) one notes that the WCC between b and a is not consistent with any time lag in I1 (i.e., for 15 s $< t <$ 25 s.) Only in I2 (i.e., for 25 s $< t <$ 49 s, between the two vertical dashed (purple) lines in Figure 3.5(a)) is the correlation between b and a significant. For electrodes b and c — whose WCC we show in Figure 3.5(b) — we find significant correlations in both I1 and I2.

To compute v in both intervals, we first determine the time lag of maximum correlation within each window in I1 (the interval shown between the vertical solid (red) line and the left, vertical dashed (purple) line in Figure 3.5) and in I2 (the interval shown between the vertical dashed (purple) lines in Figure 3.5.) For example, in Figure 3.5(a) we find that at $t = 36$ s in I2 the time lag of maximum correlation between electrodes b and a occurs near -5 ms. We repeat this calculation for all windows within each interval and average the resulting time lags of maximum correlation over the interval. Then we divide the electrode separation (approximately 10 mm) by the average time lag to determine v in I1 and I2. We note that here we determine only the one-dimensional component of v along the direction of the subdural electrode grid. We perform this analysis on both subclinical seizures and average the resulting values for v. We list the results for both electrode pairs in I1 and I2 in the third and fourth columns of Table 3.2, respectively. We note that in I1 the magnitudes of the observational results range from 0.6 m/s to 7 m/s with maximum uncertainty in the mean of 12 m/s. We find that in I2 the magnitudes of the observational results range from 1.7 m/s to 3.4 m/s with a maximum uncertainty in the mean of 0.7 m/s. For both intervals, we find that v from b to a is negative, while v from b to c is positive (although we again note the large uncertainty in I1 between electrodes b and c.) Thus, during seizure a component of the wave appears to propagate in the proximal direction, from electrodes a to b to c.

3.2.3 Subject 3

The third subject we consider is 37 year old woman with an 8×8 electrode grid over her left frontotemporal region, a 6-contact electrode strip over her left suborbital frontal lobe, and two, 6-contact left hippocampal depth electrodes. Physicians recorded ECoG data continuously from this subject for five days and detected nine seizures. Each seizure began near the distal end of both depth electrodes in the hippocampus and, approximately 15 s later, were seen on the electrode grid on the cortical surface.

Here we consider only the electrical activity recorded by the electrode grid, since the model applies only to seizure propagation on the cortical surface. In what follows, we investigate a 3×3 subgrid of electrodes located on the lateral aspect of the middle to posterior left temporal lobe, abutting the temporo-occipital junction. To help illustrate the location of this electrode subgrid, we show the craniotomy for this subject in Figure 3.6(a). Here the subject's left frontal lobe is visible at the left of the figure. We enclose six electrodes from the 3×3 subgrid with three yellow lines; the other three electrodes are hidden beneath the edge of the incision.

To determine f_0 we follow the procedure described for Subject 1 in Section 3.2.1. For each of the nine electrodes in the 3×3 subgrid, we compute the WPS and determine the average frequency of maximum power during the seizing interval. We repeat this analysis for eight of the subject's seizures (we were unable extract data for the ninth seizure) and average the results over the seizures to determine f_0 at each electrode. We show the results for the 3×3 subgrid in Figure 3.6(b). To orient this subgrid on the boxed region of the craniotomy, the reader may rotate Figure 3.6(b) counterclockwise by approximately 45°. We illustrate the results for f_0 by plotting at each grid position a circle whose radius corresponds to the mean value of f_0 at the electrode. We also write the value of f_0 (in Hz) and the uncertainty in the mean within each circle. We find values for f_0 between 7.2 Hz and 10.9 Hz, and a maximum uncertainty in the mean of 0.2 Hz.

Now we determine v. In Sections 3.2.1 and 3.2.2, we computed the component of v in one spatial dimension — along the direction of the subdural electrode strip — for Subject 1 and Subject 2, respectively. In this section, we determine the components of v along the two spatial dimensions of the electrode grid for Subject 3. To do so, we compute the WCC between each electrode of the 3×3 subgrid and its (three, five, or eight) neighbors. We follow the procedure in Section 3.2.1 and determine the time lag of maximum correlation in the two intervals I1 and I2. We average these time lags within each interval and across the eight seizures, and divide the electrode separation (10 mm in the horizontal and vertical directions, or 14.1 mm in the diagonal directions) by this result to compute v in I1 and I2 for each pair of neighboring electrodes. We show the results for v in I1 and I2 in Figures 3.7(a) and 3.7(b), respectively. The spatial arrangement of the results shown in these figures and Figure 3.6(b) are identical. Here we plot an arrow connecting each electrode — denoted by a filled black circle — with its neighbors if the uncertainty in

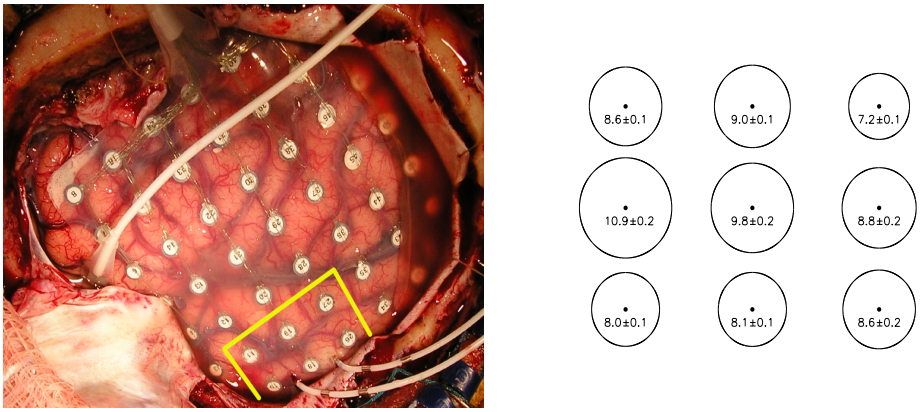

(a) (b)

Figure 3.6: (a) Craniotomy for Subject 3. The left frontal lobe is visible at the left of the figure. We indicate the location of six electrodes from the 3×3 subgrid between the three yellow lines. (b) Results for f_0 from Subject 3 recorded from the 3×3 electrode subgrid on the lateral aspect of the middle to posterior left temporal lobe, abutting the temporo-occipital junction. To orient (b) on (a), rotate (b) counterclockwise by approximately 45°. The radius of the circle corresponds to the mean value of f_0. We write the mean and uncertainty in f_0 (in Hz) within each circle.

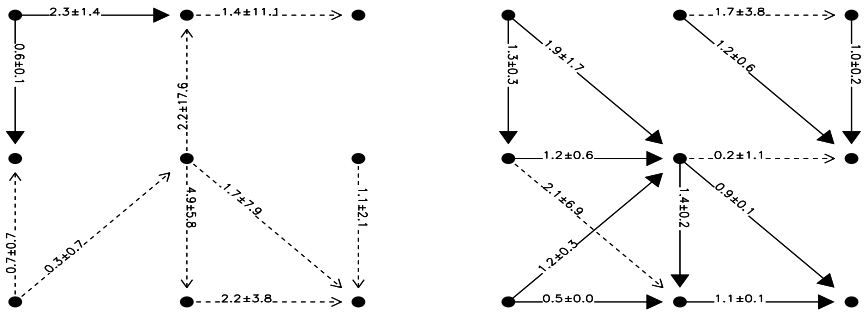

(a) (b)

Figure 3.7: Results for v from Subject 3 recorded from the 3×3 electrode subgrid on the lateral aspect of the middle to posterior left temporal lobe, abutting the temporo-occipital junction. The spatial arrangement of the results is identical to that shown in Figure 3.6(b). If the uncertainty in v is less than ten times the magnitude of v between two electrodes, then we draw an arrow connecting the two electrodes. We indicate the direction of v with the arrow and write the mean value of v and its standard deviation along the line segment. If the mean value of v exceeds one standard deviation from zero, then we draw the line segment solid and the arrowhead filled. Otherwise, we draw the line segment dashed and the arrowhead unfilled. (a) v in I1. (b) v in I2.

v is less than ten times the magnitude of v between the two electrodes. For example, in Figure 3.7(a) we do not draw an arrow between the electrode in the lower left corner and its neighbor to the right; for this electrode pair, we find $v = 3 \pm 96$ m/s, and $96 > 3 \times 10 = 30$. When an arrow is drawn, we indicate the direction of v with an arrowhead, and write the mean value of v and its standard deviation along the line segment. If the mean value of v exceeds one standard deviation from zero, we draw the line segment solid and the arrowhead filled. Otherwise, we draw the line segment dashed and the arrowhead unfilled. We note that large uncertainties in the mean occur for more values of v in I1 than in I2 (i.e., we draw fewer solid arrows in Figure 3.7(a) than in Figure 3.7(b).)

We find for Subject 3 that the magnitudes of v shown in Figure 3.7(a) range from near 0.3 m/s to 4.9 m/s, with a maximum uncertainty in the mean of 17.6 m/s; and shown in Figure 3.7(b) range from 0.2 m/s to 2.1 m/s, with a maximum uncertainty in the mean of 6.9 m/s. An inspection of Figure 3.7(b) reveals an approximate motion of the wave from the upper left corner to the lower right corner, or from the leftmost electrode in the boxed region of Figure 3.6(a) to the rightmost electrode (hidden below the incision.) This motion is not apparent for v in I1 as shown in Figure 3.7(a).

3.2.4 Subject 4

The fourth subject we consider is a 31 year old woman with an 8×8 electrode grid over her left frontotemporal region, and two, 6-electrode subdural strips curled under her left anterior and left posterior temporal lobe. Physicians recorded ECoG data from this electrode configuration for fourteen days. Three seizures were initially captured. Midway through this recording period, the surgeon inserted an additional 6-contact depth electrode into the left hippocampus. After this, three more seizures were recorded. Each seizure began in the distal end of the posterior left subtemporal electrode strip, and then spread to the distal end of the anterior subtemporal strip (as well as to the hippocampal depth electrode for the last three seizures.) After a minute delay, seizure activity appeared on the electrode grid at the frontal portions of the superior and middle temporal gyri.

To investigate the seizing activity recorded on the electrode grid, we consider a 3×3 subgrid of electrodes situated on the lateral aspects of the anterior to left temporal lobe. We indicate the location of this subgrid in the craniotomy shown in Figure 3.8(a). Here the subject's left frontal lobe is visible at the left of the figure. We enclose five electrodes from the 3×3 subgrid with three yellow lines. We note that two of these five electrodes are hidden by a wire; the other four electrodes from the 3×3 subgrid lie below the incision. To compute f_0, we follow the procedure described for Subject 3 in Section 3.2.3. We analyze the data collected during three of the subject's seizures (we were unable to extract the data for the other three seizures) and average the results over the seizures to compute f_0. We show the results for f_0 in the 3×3 subgrid in Figure 3.8(b). To orient this subgrid on the boxed region of the craniotomy, the

reader may rotate Figure 3.8(b) counterclockwise by approximately 45°. We illustrate the f_0 results by following the plotting scheme we used to create Figure 3.6(b). We find that for Subject 4 the values of f_0 range from 7.5 Hz to 8.8 Hz, with maximum uncertainty in the mean of 0.3 Hz.

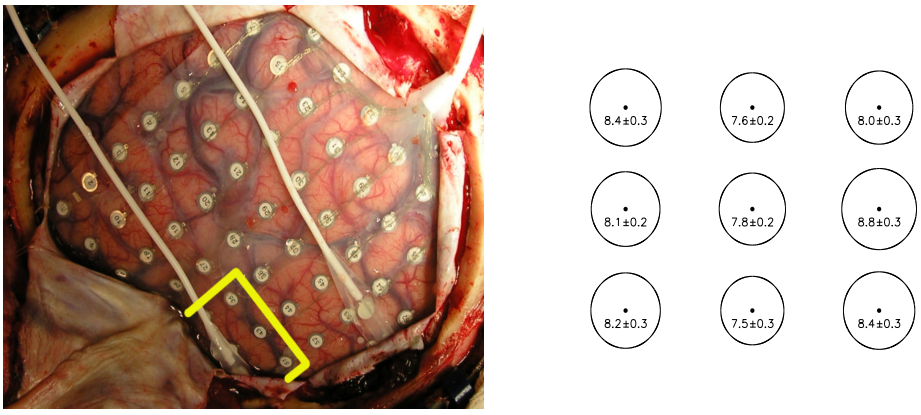

(a) (b)

Figure 3.8: (a) Craniotomy for Subject 4. The left frontal lobe is visible at the left of the figure. We indicate the location of five electrodes from the 3×3 subgrid between the three yellow lines; we note that two of the five electrodes are hidden by a wire. (b) Results for f_0 from Subject 4 recorded from the 3×3 electrode subgrid. To orient (b) on (a), rotate (b) counterclockwise by approximately 45°. The radius of the circle corresponds to the mean value of f_0. We write the mean and uncertainty in f_0 (in Hz) within each circle.

To determine v we follow the procedure described for Subject 3 in Section 3.2.3. We show the results for v in I1 and I2 from Subject 4 in Figures 3.9(a) and 3.9(b), respectively. The spatial arrangement of the results in these figures and Figure 3.8(b) are identical, and the plotting scheme follows that used to create Figure 3.7. As in Figure 3.7, we draw arrows only between those neighboring electrodes whose uncertainty in v is less than ten times the magnitude of v. We indicate the direction of v with an arrowhead and write the mean value of v and its standard deviation along the line segment. If the mean value of v exceeds one standard deviation from zero, we draw the line segment solid and the arrowhead filled. Otherwise, we draw the line segment dashed and the arrowhead unfilled. We find that the magnitudes of v range from 0.1 m/s to 13.9 m/s with a maximum uncertainty in the mean of 48.3 m/s in I1, and from 0.1 m/s to 24 m/s with a maximum uncertainty in the mean of 99.6 m/s. An inspection of Figure 3.9(b) reveals an approximate propagation of the waves to the center of the subgrid. This propagation is not apparent for v in I1 as shown in Figure 3.9(a).

In this section we applied the WPS and WCC to ECoG data recorded from four human subjects during seizure to compute f_0 and v. We summarize these results in Table 3.5 of Section 3.6. In the next section, we define a mathematical

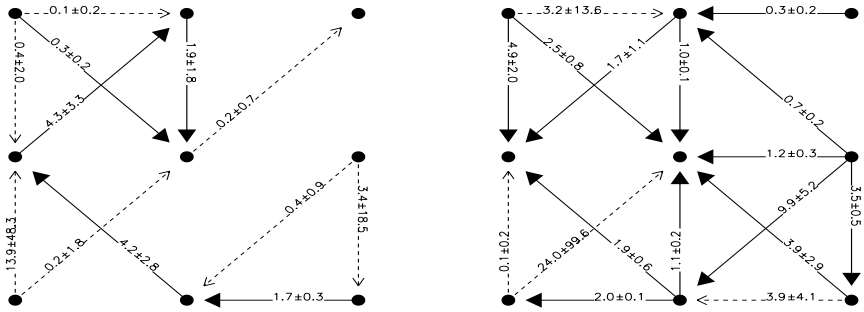

(a) (b)

Figure 3.9: Results for the 3×3 electrode subgrid recorded from Subject 4. The spatial arrangement of the results is identical to that shown in Figure 3.8(b). If the uncertainty in v is less than ten times the magnitude of v between two electrodes, then we draw an arrow connecting the two electrodes. We indicate the direction of v with the arrow and write the mean value of v and its standard deviation along the line segment. If the mean value of v exceeds one standard deviation from zero, then we draw the line segment solid and the arrowhead filled. Otherwise, we draw the line segment dashed and the arrowhead unfilled. (a) v in I1. (b) v in I2.

model of the electrical activity of the seizing human cortex: the dimensionless SPDEs. We study a simplified version of the model in Section 3.4 and the complete model in Section 3.5. We compare the observed and simulated results for f_0 and v in Section 3.6 and show how the two agree.

3.3 Model: Dimensionless SPDEs

An ideal model of the human cortex would describe the electrical behavior of each individual neuron and its surrounding extracellular environment. This discrete model — applied over the entire three-dimensional cortex — would contain over 10^{10} dynamical variables and would be intractable. Fortunately, the physiology of the cortex (e.g., dense local connections) and numerous experimental results suggest neurons act in populations or assemblies [5, 55]. Moreover, most methods for observing the human cortex (e.g., the ECoG time series of interest in this chapter) record the summed electrical activity from populations of order 10^5 cortical neurons [3]. For these reasons, researchers have developed continuum or mean field models of cortical electrical activity.

One of the earliest mean field models of cortical electrical activity was developed by H. Wilson and J. Cowan in [13]. In this work the authors described the properties of neural populations in close spatial proximity. To do so they

defined a system of differential equations to approximate the percentage of excitatory and inhibitory cells that fire per unit time in a large population. They simplified the mathematical model by performing a temporal coarse graining of the dynamical variables. The result was to average out rapid temporal variations on a time scale less than the absolute refractory period of the neurons. Thus, for a refractory period of 2 ms, we cannot use this model to simulate frequencies greater than 500 Hz. Recent experimental work has shown such high frequency oscillations (up to 650 Hz) occur and are functionally important [56].

Here we utilize a mean field model of cortical electrical activity in current use. The model — a system of SPDEs — was introduced in [57], where the authors included stochastic input to the system of PDEs first stated by D. Liley, P. Cadusch, and J. Wright (LCW) in [58]. These SPDEs (and the related ordinary differential equations — ODEs) have been successfully applied to study the electrical properties of the anesthetized human cortex (i.e., the *anesthetodynamic model* of cortical function) and the alpha rhythm. In a series of recent papers researchers have shown that the model equations predict changes in the scalp EEG of anesthetized patients consistent with experimental results [57, 59, 60, 61, 62].

Before we present the equations that define the dimensionless SPDEs model, we briefly outline its development. A detailed discussion may be found in [63]. LCW developed the system of PDEs by deducing a mathematical model of the spatially averaged soma membrane potentials (h_e and h_i) of excitatory and inhibitory cortical neural populations, respectively. To do so they performed a heuristic average of microscopic elements (e.g., individual neurons) over columnar volumes (perpendicular to the cortical surface) whose diameter was chosen to lie below the spatial resolution of EEG or ECoG recordings. We note that this averaging over space — and not over time — distinguishes the LCW model from that of Wilson and Cowan. The resulting spatially averaged neuron forms the fundamental unit of the model; it is similar to the KO set of Freeman in that both include neuronal and non-neuronal components (e.g., glial cells) [64]. We again note that the derivation is heuristic. The authors do not begin with, say, the electrical activity of an individual neuron and deduce a mean field approximation.

The spatially averaged neuron, studied in isolation, is uninteresting; the dynamical variables h_e and h_i decay to stable fixed points. To approximate cortical activity, one must include interactions between neural populations. These interactions occur through action potential — or spike — input from one neural population to another. LCW include such interactions in two ways both motivated by cortical physiology. Specifically, they assume: (1) local feedback and feedforward connections within and between excitatory and inhibitory neural populations, and (2) long range corticocortical connections that synapse on both excitatory and inhibitory populations. For simplicity and lack of detailed experimental results, LCW assume homogeneous and isotropic corticocortical connections that decrease exponentially with distance. They also include terms to describe extracortical input (e.g., input from the thalamus) to

the cortical neurons. This input is quite general; it affects the excitatory and inhibitory populations with both excitatory and inhibitory input.

Having defined the spatially averaged neuron and stated the permitted interactions between these neurons, the description of the LCW model is nearly complete. What remains is to define the relationship between the spike output and soma membrane potentials. To do so, they assume that the mean firing rate S_e (or S_i) of an excitatory (or inhibitory) local population is a function of the mean soma membrane potentials h_e (or h_i.) We note that here the term "mean" denotes a spatial — not a temporal — average. LCW make the typical approximation for the mean firing rates; they fix S_e and S_i to sigmoidal functions of h_e and h_i, respectively, and include parameters to describe the surrounding physiological environment.

The resulting mesoscopic model (with the addition of stochastic input) consists of fourteen, first-order, coupled, nonlinear SPDEs [61]. Two of these SPDEs describe the changes in voltage recorded at the excitatory and inhibitory neural populations, four describe the changing corticocortical connections, and eight describe the evolution of current inputs. By solving the SPDEs in [61] numerically, one computes solutions for all fourteen variables as functions of space and time. One of these variables, h_e, is the spatially averaged excitatory soma membrane potential. Researchers have demonstrated that the deviation of h_e from rest is proportional to the sign-reversed value of the extracellular local field potential (LFP). Because the ECoG represents the spatially averaged LFP, we assume that h_e is linearly related to the ECoG [63]. In this way, the model variable h_e is related to the observational ECoG data. In what follows we compare h_e calculated in numerical solutions to the SPDEs with ECoG data recorded during seizure. We show that increasing the subcortical excitatory input to the model cortex produces behavior in h_e that mimics ECoG data recorded from the seizing cortex.

We note that the SPDEs model used here differs from other mathematical theories of cortical electrical activity, such as those stated in [65, 66, 67], in two ways. First, the SPDEs include corticocortical excitatory to inhibitory connections which are known to exist and are essential for cortical stability [63]. Second, the time courses of the excitatory and inhibitory postsynaptic potentials recorded at the soma are described by a third order differential equation [62]. Lower order descriptions of the inhibitory postsynaptic potentials are theoretically found unable to support widespread alpha band activity. Because the SPDE model has been shown to approximate both alpha band and anesthetized human cortical activity recorded in experiment, we employ the model here.

Before beginning our analysis of the model equations, we nondimensionalize the SPDEs and associated functions. To do so we replace each dynamical variable, as well as space x and time t, with its dimensionless counterpart. For example, we replace h_e (the population mean soma voltage in [61]) with $h_e^0\tilde{h}_e$, where $h_e^0 = h_e^{\text{rest}} = -70$ mV and $\tilde{h}_e$ is dimensionless. The main advantage of recasting the equations in dimensionless form is a reduction in the number of

parameters. There are 20 parameters in the dimensionless SPDEs; in the original SPDEs there are 29. We find for the dimensionless SPDEs:

$$\frac{\partial \tilde{h}_e}{\partial \tilde{t}} = 1 - \tilde{h}_e + \Gamma_e\big(h_e^0 - \tilde{h}_e\big)\tilde{I}_{ee} + \Gamma_i\big(h_i^0 - \tilde{h}_e\big)\tilde{I}_{ie} \tag{3.1a}$$

$$\frac{\partial \tilde{h}_i}{\partial \tilde{t}} = 1 - \tilde{h}_i + \Gamma_e\big(h_e^0 - \tilde{h}_i\big)\tilde{I}_{ei} + \Gamma_i\big(h_i^0 - \tilde{h}_i\big)\tilde{I}_{ii} \tag{3.1b}$$

$$\big(\frac{1}{T_e}\frac{\partial}{\partial \tilde{t}} + 1\big)^2 \tilde{I}_{ee} = N_e^\beta \tilde{S}_e[\tilde{h}_e] + \tilde{\phi}_e + P_{ee} + \tilde{\Gamma}_1 \tag{3.1c}$$

$$\big(\frac{1}{T_e}\frac{\partial}{\partial \tilde{t}} + 1\big)^2 \tilde{I}_{ei} = N_e^\beta \tilde{S}_e[\tilde{h}_e] + \tilde{\phi}_i + P_{ei} + \tilde{\Gamma}_2 \tag{3.1d}$$

$$\big(\frac{1}{T_i}\frac{\partial}{\partial \tilde{t}} + 1\big)^2 \tilde{I}_{ie} = N_i^\beta \tilde{S}_i[\tilde{h}_i] + P_{ie} + \tilde{\Gamma}_3 \tag{3.1e}$$

$$\big(\frac{1}{T_i}\frac{\partial}{\partial \tilde{t}} + 1\big)^2 \tilde{I}_{ii} = N_i^\beta \tilde{S}_i[\tilde{h}_i] + P_{ii} + \tilde{\Gamma}_4 \tag{3.1f}$$

$$\big(\frac{1}{\lambda_e}\frac{\partial}{\partial \tilde{t}} + 1\big)^2 \tilde{\phi}_e = \frac{1}{\lambda_e^2}\frac{\partial^2 \tilde{\phi}_e}{\partial \tilde{x}^2} + \big(\frac{1}{\lambda_e}\frac{\partial}{\partial \tilde{t}} + 1\big) N_e^\alpha \tilde{S}_e[\tilde{h}_e] \tag{3.1g}$$

$$\big(\frac{1}{\lambda_i}\frac{\partial}{\partial \tilde{t}} + 1\big)^2 \tilde{\phi}_i = \frac{1}{\lambda_i^2}\frac{\partial^2 \tilde{\phi}_i}{\partial \tilde{x}^2} + \big(\frac{1}{\lambda_i}\frac{\partial}{\partial \tilde{t}} + 1\big) N_i^\alpha \tilde{S}_e[\tilde{h}_e]. \tag{3.1h}$$

The 8 dynamical variables in this system ($\tilde{h}_e$, $\tilde{h}_i$, $\tilde{I}_{ee}$, $\tilde{I}_{ei}$, $\tilde{I}_{ie}$, $\tilde{I}_{ii}$, $\tilde{\phi}_e$, and $\tilde{\phi}_i$) are functions of dimensionless space and time, $\tilde{x}$ and $\tilde{t}$, respectively. We illustrate the connections between these dynamical variables in Figure 3.10, and define the dimensionless variables and parameters in Tables 3.3 and 3.4, respectively. Each variable and parameter is expressed in terms of its dimensional counterparts from [61]. In these tables, we have made the notational simplifications in agreement with the values used in [61]: $\tau_e = \tau_i = \tau$, $S_e^{\max} = S_i^{\max} = S^{\max}$, and $h_e^{\text{rest}} = h_i^{\text{rest}} = h^{\text{rest}}$.

We also define the dimensionless sigmoid transfer functions:

$$\tilde{S}_e[\tilde{h}_e] = \frac{1}{1 + \exp[-\tilde{g}_e(\tilde{h}_e - \tilde{\theta}_e)]} \tag{3.2a}$$

$$\tilde{S}_i[\tilde{h}_i] = \frac{1}{1 + \exp[-\tilde{g}_i(\tilde{h}_i - \tilde{\theta}_i)]}, \tag{3.2b}$$

and the dimensionless stochastic input terms:

$$\tilde{\Gamma}_1 = \alpha_{ee}\sqrt{P_{ee}}\,\xi_1[\tilde{x},\tilde{t}] \tag{3.3a}$$

$$\tilde{\Gamma}_2 = \alpha_{ei}\sqrt{P_{ei}}\,\xi_2[\tilde{x},\tilde{t}] \tag{3.3b}$$

$$\tilde{\Gamma}_3 = \alpha_{ie}\sqrt{P_{ie}}\,\xi_3[\tilde{x},\tilde{t}] \tag{3.3c}$$

$$\tilde{\Gamma}_4 = \alpha_{ii}\sqrt{P_{ii}}\,\xi_4[\tilde{x},\tilde{t}]. \tag{3.3d}$$

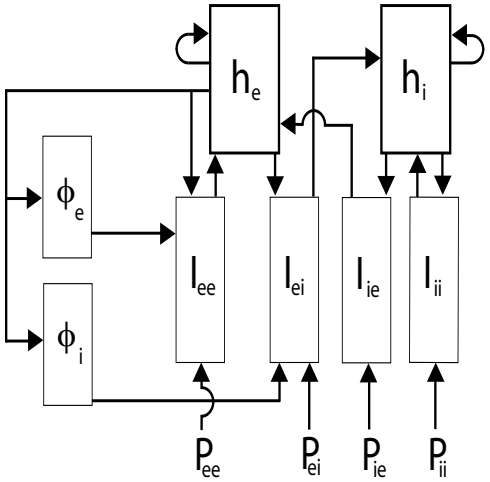

Figure 3.10: A schematic of the eight dynamical variables (boxed) and the four subcortical inputs (P_{ee}, P_{ei}, P_{ie}, P_{ii}). The variables are defined in Table 3.3; they appear in the dynamical equations (3.1). We indicate the interactions between the variables using arrows. A schematic of the cortical macrocolumn may be found in Figure 2 of [58].

The terms in (3.3) represent the noise that arises from subcortical inputs to the cortex. Here the ξ_k are Gaussian distributed white noise sources with zero mean and δ-function correlations. This assumption of Gaussian white noise is typical for the model [57, 61], although physiologically shaped brown noise is more appropriate [62]. In numerical simulations, the ξ_k are approximated as,

$$\xi_k[\tilde{x},\tilde{t}] = \frac{R(m,n)}{\sqrt{\Delta\tilde{x}\Delta\tilde{t}}}\,, \tag{3.4}$$

where $\tilde{x} = m\Delta\tilde{x}$ and $\tilde{t} = n\Delta\tilde{t}$ (m,n integers), specify space and time coordinates on a lattice with (dimensionless) grid spacings, $\Delta\tilde{x}$ and $\Delta\tilde{t}$, respectively. Here we set $\alpha_{ee} = \alpha_{ei} = \alpha_{ie} = \alpha_{ii} = \alpha$ as in the stochastic simulations of the spatioadiabatic one-dimensional cortex in [61].

In what follows, we first study a simplified ordinary differential equations (ODEs) version of the dimensionless model in Section 3.4. Our methods differ from previous discussions. We do not make the assumption that some variables equilibrate much faster than others (the slow-membrane or adiabatic approximation [57].) Nor do we apply techniques of stochastic calculus (such as the Ornstein-Uhlenbeck equation) to the linearized SPDEs [61]. Instead, we approach the SPDEs from a dynamical systems perspective and employ ideas and tools from bifurcation theory. In Section 3.5 we consider the complete dimensionless SPDEs. We show by an analysis of linear stability how the results from the simplified dimensionless ODEs relate to the dynamics of the dimensionless SPDEs with no stochastic input. We then compute three numerical solutions to the dimensionless SPDEs and in Section 3.6 we compare the model and observational results for f_0 and v.

3.4 Simulations: Dimensionless ODEs

Our goal in this chapter is to determine whether the dimensionless SPDEs in (3.1) can be used to model the mesoscopic electrical activity observed on the seizing cortical surface, as discussed in Section 3.2. However, the size of the system (14 first order differential equations, and 20 parameters), the stochastic input in (3.1c)-(3.1f), and the spatial dependence in (3.1g) and (3.1h) make this a challenging model. Therefore, to gain what insight we can from a simpler model, we ignore for the moment the spatial dependence and stochastic input in (3.1). The resulting equations form a system of ordinary differential equations which we call the dimensionless ODEs. There are many tools available for the study of ODEs; here we shall use AUTO (continuation and bifurcation software for ordinary differential equations) to determine fixed points, their stability type, limit cycles, and bifurcations in the phase portraits [68].

During a seizure the cortex typically enters a state of hyperexcitation, manifest in ECoG data through large amplitude oscillations [69]. This activity corresponds to spatially coherent oscillations in the variable h_e (or $\tilde{h}_e$.) In this direction, we investigate whether oscillations in h_e occur in the dimensionless ODEs due to changes in the excitatory parameters. We note that different types of seizures produce different oscillatory patterns in EEG and ECoG recordings [70, 71]. Here we seek to model the seizing cortex in a qualitative way suggestive of the typical ECoG data shown in Figure 3.1. Specifically, we require that: 1) the model produce stable oscillations in h_e, 2) the frequency of the oscillations agree (roughly) with clinical observations, and 3) the transition to oscillatory behavior occur abruptly.

The general statement that increased excitation (or decreased inhibition) incites cortical seizure activity masks the numerous associated physiological changes that occur in the seizing neuronal assemblies [72, 51]. At the cellular level these physiological changes are observed in experiment and can be compared to results computed from detailed computational models of a single neuron [73]. How the cellular mechanisms or single neuron models relate to mesoscopic seizure recordings or continuum models is not clear (although see [10].) Seizures induced in animal models allow mesoscopic ECoG recordings and some control over parameters related to continuum models. For example, in [74], W. Freeman discusses electrocortical data recorded from a seizing animal's olfactory bulb. He compares these recordings with his KIII model of the olfactory system and finds that a parameter connecting excitatory subsets of the model must increase to induce seizures. Analogies between such animal models and human seizure activity can be made, but, as for the cellular models, these relationships are not clear.

In our analysis, we initially vary only two parameters, P_{ee} and Γ_e, both related to the excitation of the model. We choose to vary these parameters for two reasons. First, as mentioned previously, the general claim that increased

excitation incites seizures is well known. Thus, we select two parameters related to the excitation of the model. Second, an increase in the level of the membrane potential of a neuronal population is thought to be an important control factor in inducing seizures [75, 51]. We will show that increases in Γ_e raise the excitatory mean soma potential h_e of the stable fixed points; a similar results holds for P_{ee} but is not shown. In what follows, we fix the remaining 18 dimensionless parameters at the typical values shown in Table 3.4. In terms of dimensional variables, the dimensionless parameter P_{ee} is: 1) directly proportional to p_{ee} (the subcortical excitatory spike input to the excitatory neurons of the cortex), and 2) inversely proportional to S^{max} (the maximum firing rate induced by the soma voltage). Thus an increase in P_{ee} represents either an increase in the subcortical excitation of the cortex or a decrease in the maximum firing rate. To model an increase in excitatory input (from a subcortical region, such as the thalamus) to the cortex, the parameter P_{ee} is increased. The dimensionless parameter Γ_e is: 1) directly proportional to S^{max} and G_e (the peak excitatory postsynaptic potential — EPSP), and 2) inversely proportional to γ_e (the EPSP neurotransmitter rate constant) and $|h_e^{\text{rev}} - h^{\text{rest}}|$ (the magnitude of the difference between the excitatory reversal and resting potentials.) Thus an increase in Γ_e represents either an increase in peak EPSP amplitude or maximum firing rate, or a decrease in the difference between the excitatory reversal and resting potentials or the EPSP neurotransmitter rate constant. The latter corresponds to an increase in the EPSP duration. We note that the typical values of P_{ee} and Γ_e are 11.0 and 1.42×10^{-3}, respectively; see Table 3.4.

It is perhaps easier to interpret the parameters P_{ee} and Γ_e directly from (3.1). The parameter P_{ee} only appears in (3.1c); this parameter controls the strength of the (nonstochastic) excitatory subcortical input to excitatory neurons in the cortex. The parameter Γ_e appears in (3.1a) and (3.1b), and controls the influence of excitatory input on the mean soma membrane potentials. For example, when Γ_e is large the effect of the excitatory inputs ($\tilde{I}_{ee}$ and $\tilde{I}_{ei}$) on the potentials ($\tilde{h}_e$ and $\tilde{h}_i$) is increased. Here we assume that the effect of the excitatory inputs is independent of the postsynaptic neuron (i.e., $\tilde{\Gamma}_{ee} = \tilde{\Gamma}_{ei} = \tilde{\Gamma}_e$.) In Section 3.8, we relax this (and other) assumptions. We will show that solutions of the model equations agree qualitatively with ECoG data recorded from the seizing cortex when: P_{ee} is dramatically increased, and Γ_e is slightly decreased.

In what follows, we compute bifurcation diagrams and numerical solutions of the dimensionless ODEs at two values of P_{ee}. We first consider the results for $P_{ee} = 11.0$ (the typical value) and show that oscillations in h_e occur but are unstable and short lived. We then show that for $P_{ee} = 548.066$ (nearly 50 times the typical subcortical excitation) h_e undergoes large amplitude, stable oscillations, and that similar oscillations occur over a wide range of parameter values. The results in each case are compared to the clinical data discussed in Section 3.2.

3.4.1 Example: Dimensionless ODES at $P_{ee} = 11.0$

In the first example, we fix P_{ee} at its typical (dimensionless) value of 11.0 and vary the parameter Γ_e. We plot in Figure 3.11(a) h_e for the fixed points of the dimensionless ODEs versus the parameter Γ_e. We note that in this figure we plot the dimensional variable h_e (with units mV) which is related to $\tilde{h}_e$ by the scale factor $h_e^0 = -70$ mV. The solid lines and dashed line in Figure 3.11(a) correspond to the stable and unstable fixed points of the dimensionless ODEs, respectively. We note that an increase in Γ_e produces an increase in both curves of the stable fixed point value of h_e (i.e., increased steady state values of the spatially averaged excitatory soma membrane potential.)

The S-shape and stability of the fixed points is similar to that discussed in [61] and [57]. In those works, the authors varied the (dimensional) inhibitory neurotransmitter rate constant γ_i. Here, the parameter Γ_e is inversely proportional to the (dimensional) excitatory neurotransmitter rate constant γ_e. We have found, but do not show, similar bifurcation diagrams for the *dimensional* SPDEs with $\gamma_i \to \gamma_i/\lambda$ or $\gamma_e \to \gamma_e\lambda$ and parameter λ varied between 0.1 and 1.5.

In addition to the saddle node bifurcations of fixed points, the dimensionless ODEs at $P_{ee} = 11.0$ also undergo a Hopf bifurcation at $\Gamma_e = 1.20 \times 10^{-3}$. (We note this represents a 15% decrease in the typical value of $\Gamma_e = 1.42 \times 10^{-3}$.) We mark this Hopf bifurcation in Figure 3.11(a) with an asterisk and show how the eigenvalues change near this Hopf bifurcation in Figure 3.11(b). As we approach the Hopf bifurcation along the curve of unstable fixed points, we find a transition from one positive, real eigenvalue to two. This transition occurs at the saddle node bifurcation near $\Gamma_e = 1.09 \times 10^{-3}$. As we continue past the saddle node bifurcation, the two real, positive eigenvalues approach and collide, acquire nonzero imaginary parts, and become a complex conjugate pair. Then, as we continue along the curve of unstable fixed points toward the Hopf bifurcation, the imaginary parts of both eigenvalues increase and the real parts approach zero. At the Hopf bifurcation, the pair of complex conjugate eigenvalues crosses the real axis.

We are particularly interested in Hopf bifurcations because, at a Hopf bifurcation, the dynamics of h_e can change from stationary behavior to oscillatory behavior. To illustrate the oscillatory behavior of h_e near the Hopf bifurcation we compute a numerical solution to the dimensionless ODEs near the Hopf bifurcation at $\Gamma_e = 1.21 \times 10^{-3}$ and $P_{ee} = 11.0$. We choose the initial conditions so that the dynamics begin just outside the basin of attraction of the stable fixed point and compute the trajectory using a fourth-order Runge-Kutta method with a time step of 0.4 ms. We plot in Figure 3.11(c) (dimensional) h_e as a function of dimensional time t. For $0 \text{ s} < t < 9.5$ s, h_e oscillates at approximately 8 Hz. The amplitude of the oscillations steadily increases until $t = 9.5$ s at which point h_e abruptly moves to the stable fixed point near -84 mV. We show this transition with finer resolution in Figure 3.11(d).

We have shown that for $P_{ee} = 11.0$ the dynamics of h_e undergo a Hopf bifurcation at $\Gamma_e = 1.20 \times 10^{-3}$. Near

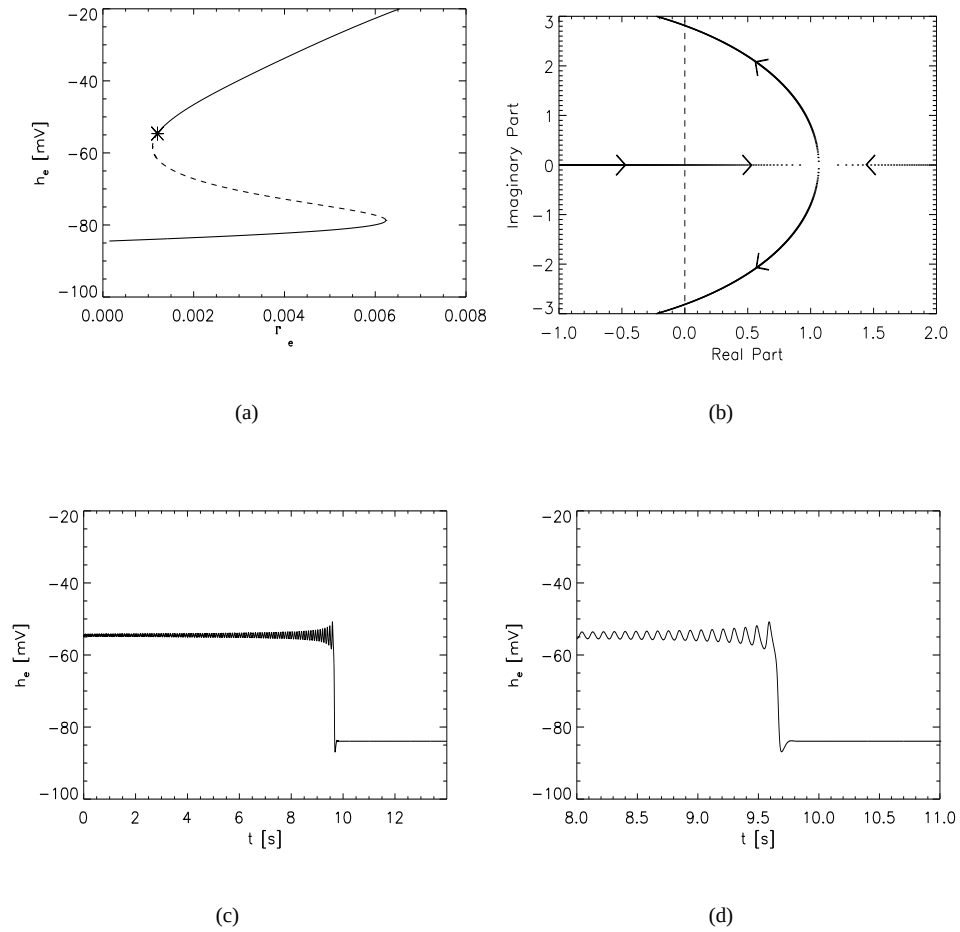

Figure 3.11: (a) Bifurcation diagram for the dimensionless ODEs at $P_{ee} = 11.0$. As the dimensionless parameter Γ_e is varied, the stable (solid curves) and unstable (dashed curves) fixed points in h_e of the dimensionless ODEs are shown. The asterisk denotes the Hopf bifurcation. There are two saddle-node bifurcations also visible in the figure. (b) The eigenvalues near the Hopf bifurcation. We plot the real and imaginary parts along the horizontal and vertical axes, respectively. The arrowheads indicate how the eigenvalues change as we approach the Hopf bifurcation along the curve of unstable fixed points in (a). (c) Numerical solution to the dimensionless ODEs at $\Gamma_e = 1.21 \times 10^{-3}$ and $P_{ee} = 11.0$, near the Hopf bifurcation shown in (a). Dimensional h_e is plotted as a function of dimensional time t. The oscillations in h_e increase in amplitude until the oscillations cease and $h_e \to -84$ mV. (d) The transition from transient oscillatory motion in h_e to the fixed point at finer resolution.

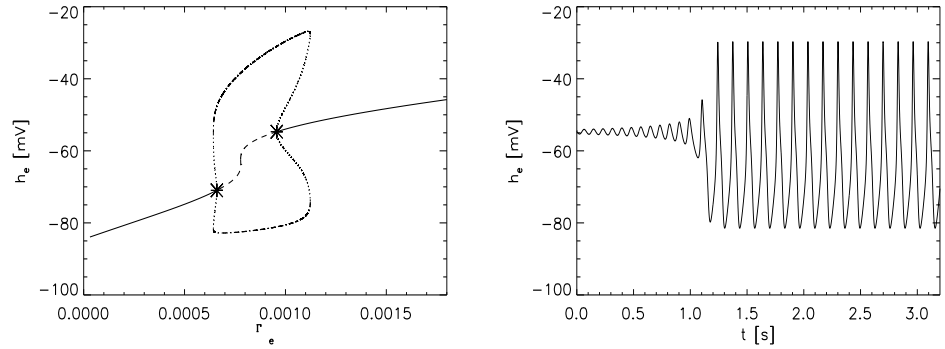

(a) (b)

Figure 3.12: (a) Bifurcation diagram for the dimensionless ODEs at $P_{ee} = 548.066$. The parameter Γ_e is varied and the stable (solid curves) and unstable (dashed curve) fixed points in h_e are shown. The asterisks denote the two Hopf bifurcations. The dash-dot lines denote the maximum and minimum values of h_e achieved during a stable limit cycle. The dotted lines denote the maximum and minimum values of h_e achieved during an unstable limit cycle. The branch of limit cycles is born and dies in two subcritical Hopf bifurcations; two saddle-node bifurcations of limit cycles lead to large amplitude stable oscillations with sudden onset. (b) Numerical solution to the dimensionless ODEs at $\Gamma_e = 0.96 \times 10^{-3}$ and $P_{ee} = 548.066$, near the rightmost Hopf bifurcation in (a). Dimensional h_e is plotted as a function of dimensional time t. The oscillations in h_e occur at a frequency near 7.5 Hz and are stable to perturbations.

the Hopf bifurcation there exist transient oscillations in h_e that increase in amplitude until the dynamics undergo a transition to a stable fixed point near -84 mV. We have not shown but note that adding noise to the system decreases the time of the transient oscillations. These unstable oscillations in h_e do not mimic the electrical activity of the seizing cortex where the oscillations maintain a large amplitude and are necessarily stable to incessant perturbations from other cortical, as well as deeper, brain regions.

3.4.2 Example: Dimensionless ODEs at $P_{ee} = 548.066$

In this subsection we consider an example more closely related to the seizing cortex. To increase the excitation of the model cortex, we fix $P_{ee} = 548.066$ (nearly 50 times the typical value.) This can be interpreted as increased excitatory input from deeper brain regions to the cortex, say. As in Section 3.4.1, we vary the parameter Γ_e and plot in Figure 3.12(a) the bifurcation diagram in h_e for the dimensionless ODEs. The solid curves and dashed curve in Figure 3.12(a) correspond to stable and unstable fixed points of the dimensionless ODEs, respectively, and the asterisks to Hopf bifurcations. We note that an increase in Γ_e produces an increase in both curves of stable fixed points of h_e.

There are additional curves in Figure 3.12(a) absent from Figure 3.11(a). These curves indicate the extremal values

and stability type of the limit cycles born in the Hopf bifurcations. The dash-dot lines in Figure 3.12(a) represent the maxima and minima of h_e achieved during a *stable* limit cycle. The dotted lines represent the maxima and minima of h_e achieved during an *unstable* limit cycle. Thus, for $0.67 \times 10^{-3} < \Gamma_e < 0.96 \times 10^{-3}$, the dynamics of h_e feature a stable limit cycle of large amplitude. These dynamics possess a subHopf/fold cycle type of bifurcation, or equivalently, the dynamics undergo elliptic bursting [76]. We note that a 32% decrease in the typical value of $\Gamma_e = 1.42 \times 10^{-3}$ is required to enter this range. The stable, oscillatory behavior of h_e satisfies one of our criteria for modeling the seizing cortex.

To illustrate the stable oscillations in h_e for $0.67 \times 10^{-3} < \Gamma_e < 0.96 \times 10^{-3}$, we compute a numerical solution to the dimensionless ODEs at $\Gamma_e = 0.96 \times 10^{-3}$ and $P_{ee} = 548.066$ using the fourth-order Runge-Kutta method with a time step of 0.4 ms. In Figure 3.12(b) we plot h_e (with dimensions mV) as a function of dimensional time t. After an initial transient, h_e is entrained by a large amplitude limit cycle with a dominant frequency near 7.5 Hz. We note that these oscillations are not sinusoidal. The frequency of the h_e oscillations roughly agrees with the clinical observations from a seizing human subject shown in Figure 3.1.

To summarize, we have shown two bifurcation diagrams for the dimensionless ODEs and found that the number of limit points and Hopf bifurcations differ. For $P_{ee} = 11.0$, shown in Figure 3.11(a), there are two limit points at $\Gamma_e = 6.23 \times 10^{-3}$ and $\Gamma_e = 1.09 \times 10^{-3}$, and one Hopf bifurcation at $\Gamma_e = 1.20 \times 10^{-3}$. For $P_{ee} = 548.066$, shown in Figure 3.12(a), there is one limit point at $\Gamma_e = 0.78 \times 10^{-3}$ and two Hopf bifurcations at $\Gamma_e = 0.66 \times 10^{-3}$ and $\Gamma_e = 0.96 \times 10^{-3}$. To determine how the limit points and Hopf bifurcations depend upon the two parameters, we plot the location of each limit point and Hopf bifurcation as a function of Γ_e and P_{ee} in Figure 3.13(a). In this figure, we plot the limit points (solid curve), Hopf bifurcations (dotted curve), and codimension two bifurcations (asterisks) for $-2000 < P_{ee} < 9000$ and $0.0 < \Gamma_e < 0.004$. The only true intersections of the limit point curve and Hopf bifurcation curve occur at the codimension two bifurcations; other crossings in this figure (e.g., near $P_{ee} = 500.0$ and $\Gamma_e = 1.0 \times 10^{-3}$) result from the projection of the full dynamics to the two dimensional (Γ_e, P_{ee})-plane. We note that for $P_{ee} > 600.0$ no limit points occur in the dynamics, and for $\Gamma_e > 3.0 \times 10^{-3}$ no Hopf bifurcations occur.

We can compare the results of the two-parameter variation shown in Figure 3.13(a) with the bifurcation diagrams shown in Figures 3.11(a) and 3.12(a). We plot in Figure 3.13(b) the locations of the limit points and Hopf bifurcations over a limited range of P_{ee} and extended range of Γ_e. In addition, we plot thin, horizontal lines at $P_{ee} = 11.0$ (lower horizontal line) and $P_{ee} = 548.066$ (upper horizontal line.) We find that the lower line at $P_{ee} = 11.0$ crosses the limit point curve twice (at 1.1×10^{-3} and 6.2×10^{-3}) and the Hopf bifurcation curve (at 1.2×10^{-3}) once — in agreement with the number and location of limit points and Hopf bifurcations shown in Figure 3.11(a). In a similar way, we find that the upper line at $P_{ee} = 548.066$ in Figure 3.13(b) crosses the Hopf bifurcation curve twice (at 0.66×10^{-3} and

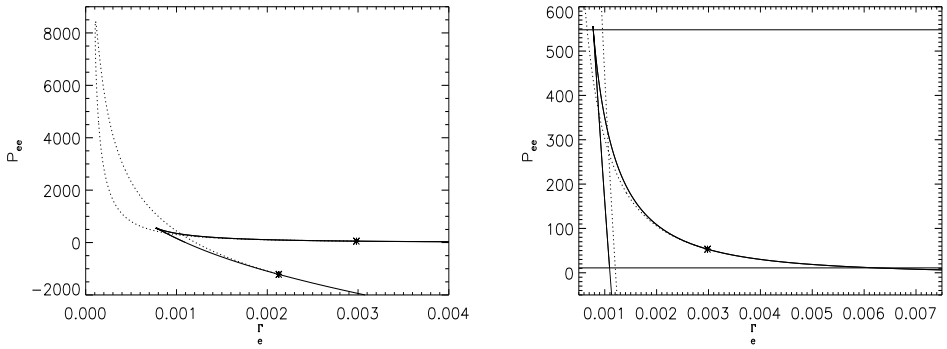

(a) (b)

Figure 3.13: The values of the limit points (solid curve) and Hopf bifurcations (dotted curve) as functions of the parameters Γ_e and P_{ee}. We denote the two codimension two bifurcations with asterisks. (a) The full parameter range, including unphysical negative values of P_{ee}. (b) A limited parameter range in P_{ee} and extended range in Γ_e. We plot thin, horizontal lines at $P_{ee} = 11.0$ and $P_{ee} = 548.066$.

0.96×10^{-3}) and the limit point curve once (at 0.78×10^{-3}), in agreement with the number and position of limit points and Hopf bifurcations shown in Figure 3.12(a).

We also show in Figure 3.13(b) the location of the codimension two bifurcation at $\Gamma_e = 2.98 \times 10^{-3}$ and $P_{ee} = 53.2$. We mark this point with an asterisk. To the left of this codimension two bifurcation one eigenvalue of the limit point is positive, one is zero, and the rest are negative — thus the limit point is unstable. For the Hopf bifurcation, two of the eigenvalues form a complex conjugate pair with zero real part and the rest are negative. As the dynamics approach the codimension two bifurcation from the left (i.e., decreased P_{ee} and increased Γ_e) the positive eigenvalue of the limit point approaches zero. In addition, the purely imaginary complex conjugate pair of eigenvalues of the Hopf bifurcation approach zero along the imaginary axis. At the codimension two bifurcation, the largest eigenvalue of the limit point reaches zero and the purely imaginary eigenvalues of the Hopf bifurcation coalesce at the origin. Here the dynamics linearized at the limit point or Hopf bifurcation possesses two zero eigenvalues; this defines the codimension two bifurcation of Takens-Bogdanov type [77]. To the right of this point (i.e., for $\Gamma_e > 2.98 \times 10^{-3}$ and $P_{ee} < 53.2$) only a stable limit point remains (with one zero eigenvalue and the rest negative.) A second Takens-Bogdanov bifurcation occurs at $\Gamma_e = 2.13 \times 10^{-3}$ and $P_{ee} = -1215.6$; see Figure 3.13(a). We do not consider this bifurcation because the negative value of P_{ee} is unphysical.

At the codimension two bifurcation shown in Figure 3.13(b), where $\Gamma_e = 2.98 \times 10^{-3}$ and $P_{ee} = 53.2$, the distance between the Hopf bifurcation and limit point reaches zero. To examine how the frequency of the limit cycle born at the

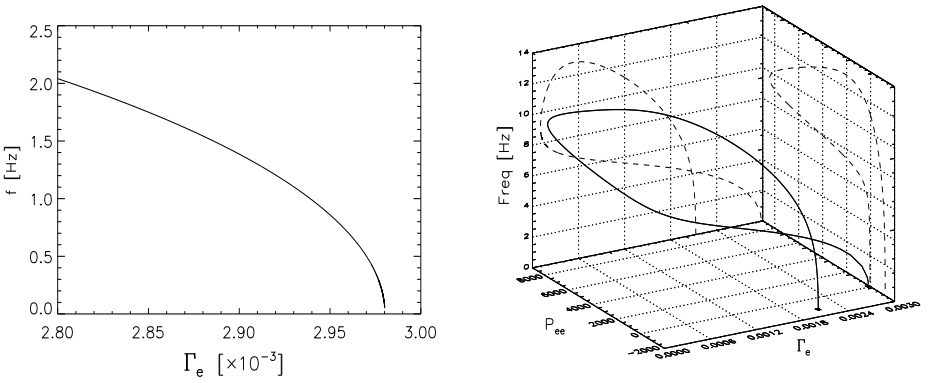

(a) (b)

Figure 3.14: (a) The frequency f of the limit cycles born in the Hopf bifurcation as a function of Γ_e along the curve of Hopf bifurcation near the codimension two point shown in Figure 3.13(b). As $\Gamma_e \to 2.98 \times 10^{-3}$ a codimension two bifurcation occurs and the frequency of the limit cycles approaches zero. (b) The frequency f of the limit cycles born in the Hopf bifurcations as a function of the two parameters P_{ee} and Γ_e. We mark the codimension two bifurcations with asterisks. We plot the projection of frequency versus Γ_e on the f-Γ_e plane, and the projection of frequency versus P_{ee} on the f-P_{ee} planes as dashed lines.

Hopf bifurcation depends upon this distance, we follow the Hopf bifurcation along the solid curve in Figure 3.13(b) for $2.8 \times 10^{-3} < \Gamma_e < 3.0 \times 10^{-3}$ We plot in Figure 3.14(a) the frequency f of the limit cycle born in the Hopf bifurcation as a function of Γ_e along the curve of Hopf bifurcations. We find that, as Γ_e approaches the Takens-Bogdanov bifurcation and the separation between the Hopf bifurcation and limit point approaches zero, f also approaches zero (or the period approaches infinity) as expected.

Away from the codimension two point, we find that the frequency f of the limit cycles born in the Hopf bifurcations depends on both parameters P_{ee} and Γ_e. To illustrate this, we show in Figure 3.14(b) the value of f at both Hopf bifurcations as a function of P_{ee} and Γ_e. We indicate the codimension two points (where $f \to 0$) with asterisks, and show the projections onto the f-P_{ee} and f-Γ_e planes. We find that the limit cycles born in the Hopf bifurcations have frequencies ranging from 0 Hz to 12.8 Hz.

The analysis we show in Figure 3.13(a) does not indicate the stability of the limit cycles born in the Hopf bifurcations, the basins of attraction of the Hopf bifurcations, nor the frequency of the oscillations. Because the true environment of the human cortex is continually changing (for example, in response to sensory stimuli) we require that stable oscillatory activity in h_e occur over extended regions of the parameters P_{ee} and Γ_e. To determine the extent of the stable oscillations in h_e, we compute numerical solutions to the dimensionless ODEs for $11.0 < P_{ee} < 1000.0$ and $0.5 \times 10^{-3} < \Gamma_e < 1.4 \times 10^{-3}$ using the fourth-order Runge-Kutta method with a time step of 0.4 ms. We then

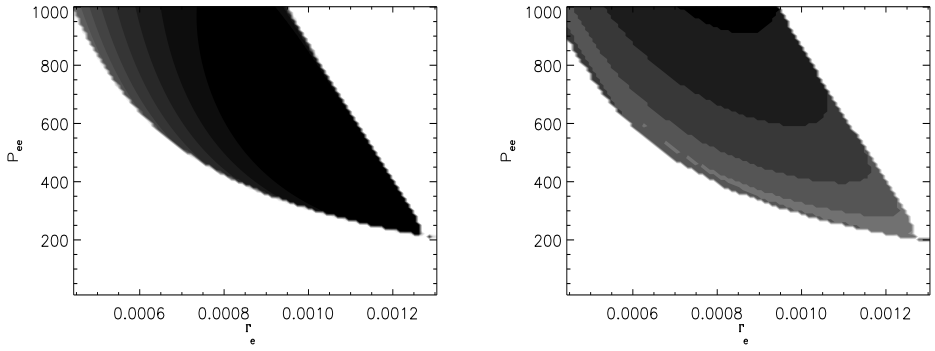

(a) (b)

Figure 3.15: (a) The difference between the maximum and minimum achieved by (the dimensional) h_e in solutions of the dimensionless ODEs for parameters P_{ee} and Γ_e. The difference is plotted in linear greyscale with white representing a 0 mV difference and black representing a 50 mV difference. The dark region corresponds to stable oscillations of h_e and broadens as P_{ee} is increased. The parameter values used to create Figure 3.12(b) ($\Gamma_e = 0.96 \times 10^{-3}$ and $P_{ee} = 548.066$) are near the center of this figure. (b) The frequency of oscillations in h_e in solutions of the dimensionless ODEs for parameters P_{ee} and Γ_e. The frequency is plotted in greyscale with white representing 0 Hz (no oscillations) and black representing 9 Hz and larger.

determine the difference between the maximum and minimum achieved by the solution h_e after transient behavior has decayed. If h_e approaches a fixed point, then the maximum and minimum are nearly equal and their difference approaches zero. But, if h_e is entrained by a limit cycle (see, for example, Figure 3.12(b)) then the difference between the maximum and minimum achieved by h_e is nonzero. In Figure 3.15(a) we plot the difference between the maximum and minimum achieved by h_e as a function of the parameters P_{ee} and Γ_e. The difference is plotted in greyscale with white representing a 0 mV difference and black representing a 50 mV difference. We find that oscillations in h_e (represented by the dark region in Figure 3.15(a)) extend over a broad range of parameter values beginning near $P_{ee} = 250.0$ and $\Gamma_e = 1.3 \times 10^{-3}$. We note that the amplitudes of the oscillations do not approach zero at the boundaries of the dark region in Figure 3.15(a).

To determine the approximate frequency of oscillations in h_e, we again compute numerical solutions to the dimensionless ODEs over the same parameter range and implementing the same numerical method used to create Figure 3.15(a). We then compute the power spectrum of h_e after transient behavior has decayed and determine the frequency of maximum power. We note that the frequency resolution of this calculation is 0.5 Hz, and that the power spectra possess a single, well-defined peak. We show the results of this calculation in Figure 3.15(b). Here white represents a frequency of 0 Hz and black represents frequencies of 9 Hz and higher.

The regions of oscillatory activity in h_e, shown in Figures 3.15(a) and 3.15(b), illustrate the parameter values at which the dimensionless ODEs "seize." We note that increasing P_{ee}, and thus raising the subcortical excitatory input to the model cortex, enlarges the region of Γ_e over which oscillations in h_e occur and increases the frequency of these oscillations.

3.5 Simulation: Dimensionless SPDEs

We have considered in some detail the dimensionless ODEs. For example, we have shown in Section 3.4.2 that the dimensionless ODEs undergo a Hopf bifurcation near $P_{ee} = 548.066$ and $\Gamma_e = 0.96 \times 10^{-3}$, and that oscillations in h_e persist over a broad region of parameter values. Unfortunately, there is no direct conclusion that the analysis of this simplified system allows one to draw for the complete dimensionless SPDEs. The stochastic inputs or the spatially distributed dynamics may destroy the interesting features we observed in the dimensionless ODEs. Here we shall examine whether the full dimensionless SPDEs exhibit similar oscillatory behavior. We will consider three examples. For each example, we compute numerical solutions to the dimensionless SPDEs using the Euler-Maruyama algorithm with fixed steps in space and time, 14 mm and 0.1 ms, respectively [78]. We consider only one spatial dimension $\tilde{x}$; the system can now be visualized as describing a line of closely spaced electrodes, such as the strip of subdural electrodes described in Section 3.2. In each example, we enforce periodic boundary conditions in space, fix Γ_e and α (representing the noisy input from subcortical sources to the cortex) to be uniform in $\tilde{x}$ and $\tilde{t}$, and vary the spatial and temporal dependence of P_{ee}. In the first example, we set the stochastic input $\alpha = 0$ and consider the linear stability of the spatially uniform state for $P_{ee} = 548.066$ fixed and Γ_e varied. We compare the linear stability results with numerical solutions of the dimensionless SPDEs and show that the two agree. In the second example, we solve the dimensionless SPDEs for P_{ee} Gaussian in space and constant in time. In the third, we solve the dimensionless SPDEs for P_{ee} Gaussian in space and nonuniform in time. We compare in Section 3.6 the results of these simulations with the clinical seizure data.

We start by setting the stochastic input $\alpha = 0$ and considering the linear stability of the uniform steady state. To

do so, we first introduce six new variables $(\tilde{J}_{ee}, \tilde{J}_{ei}, \tilde{J}_{ie}, \tilde{J}_{ii}, \tilde{\psi}_e, \tilde{\psi}_i)$ and write (3.1) as fourteen PDEs first-order in time.

$$\frac{\partial \tilde{h}_e}{\partial \tilde{t}} = 1 - \tilde{h}_e + \Gamma_e\left(h_e^0 - \tilde{h}_e\right)\tilde{I}_{ee} + \Gamma_i\left(h_i^0 - \tilde{h}_e\right)\tilde{I}_{ie} \tag{3.5a}$$

$$\frac{\partial \tilde{h}_i}{\partial \tilde{t}} = 1 - \tilde{h}_i + \Gamma_e\left(h_e^0 - \tilde{h}_i\right)\tilde{I}_{ei} + \Gamma_i\left(h_i^0 - \tilde{h}_i\right)\tilde{I}_{ii} \tag{3.5b}$$

$$\frac{\partial \tilde{I}_{ee}}{\partial \tilde{t}} = \tilde{J}_{ee} \tag{3.5c}$$

$$\frac{\partial \tilde{J}_{ee}}{\partial \tilde{t}} = -2T_e\tilde{J}_{ee} - T_e^2\tilde{I}_{ee} + T_e\left(N_e^\beta \tilde{S}_e[\tilde{h}_e] + \tilde{\phi}_e + P_{ee} + \tilde{\Gamma}_1\right) \tag{3.5d}$$

$$\frac{\partial \tilde{I}_{ei}}{\partial \tilde{t}} = \tilde{J}_{ei} \tag{3.5e}$$

$$\frac{\partial \tilde{J}_{ei}}{\partial \tilde{t}} = -2T_e\tilde{J}_{ei} - T_e^2\tilde{I}_{ei} + T_e\left(N_e^\beta \tilde{S}_e[\tilde{h}_e] + \tilde{\phi}_i + P_{ei} + \tilde{\Gamma}_2\right) \tag{3.5f}$$

$$\frac{\partial \tilde{I}_{ie}}{\partial \tilde{t}} = \tilde{J}_{ie} \tag{3.5g}$$

$$\frac{\partial \tilde{J}_{ie}}{\partial \tilde{t}} = -2T_i\tilde{J}_{ie} - T_i^2\tilde{I}_{ie} + T_i\left(N_i^\beta \tilde{S}_i[\tilde{h}_i] + P_{ie} + \tilde{\Gamma}_3\right) \tag{3.5h}$$

$$\frac{\partial \tilde{I}_{ii}}{\partial \tilde{t}} = \tilde{J}_{ii} \tag{3.5i}$$

$$\frac{\partial \tilde{J}_{ii}}{\partial \tilde{t}} = -2T_i\tilde{J}_{ii} - T_i^2\tilde{I}_{ii} + T_i\left(N_i^\beta \tilde{S}_i[\tilde{h}_i] + P_{ii} + \tilde{\Gamma}_4\right) \tag{3.5j}$$

$$\frac{\partial \tilde{\phi}_e}{\partial \tilde{t}} = \tilde{\psi}_e \tag{3.5k}$$

$$\frac{\partial \tilde{\psi}_e}{\partial \tilde{t}} = -2\lambda_e\tilde{\psi}_e - \lambda_e^2\tilde{\phi}_e + \frac{\partial^2 \tilde{\phi}_e}{\partial \tilde{x}^2} + \lambda_e N_e^\alpha \frac{\partial \tilde{S}_e[\tilde{h}_e]}{\partial \tilde{t}} + \lambda_e^2 N_e^\alpha \tilde{S}_e[\tilde{h}_e] \tag{3.5l}$$

$$\frac{\partial \tilde{\phi}_i}{\partial \tilde{t}} = \tilde{\psi}_i \tag{3.5m}$$

$$\frac{\partial \tilde{\psi}_i}{\partial \tilde{t}} = -2\lambda_i\tilde{\psi}_i - \lambda_i^2\tilde{\phi}_i + \frac{\partial^2 \tilde{\phi}_i}{\partial \tilde{x}^2} + \lambda_i N_i^\alpha \frac{\partial \tilde{S}_e[\tilde{h}_e]}{\partial \tilde{t}} + \lambda_i^2 N_i^\alpha \tilde{S}_e[\tilde{h}_e]. \tag{3.5n}$$

$$\tag{3.5o}$$

Next we define the $14-$dimensional vector $\mathbf{u} = \{\tilde{h}_e, \tilde{h}_i, \tilde{I}_{ee}, \tilde{J}_{ee}, \tilde{I}_{ei}, \tilde{J}_{ei}, \tilde{I}_{ie}, \tilde{J}_{ie}, \tilde{I}_{ii}, \tilde{J}_{ii}, \tilde{\phi}_e, \tilde{\psi}_e, \tilde{\phi}_i, \tilde{\psi}_i\}$ and write (3.5) as,

$$\frac{\partial \mathbf{u}}{\partial \tilde{t}} = \mathbf{G}[\mathbf{u}, \frac{\partial^2 \mathbf{u}}{\partial \tilde{x}^2}, \mathbf{P}], \tag{3.6}$$

where $\mathbf{G}$ is the vector representation of the right-hand side of (3.5), and $\mathbf{P}$ is a vector containing the 20 parameters. We express the linear approximation to the dynamics in (3.6) about the uniform steady state as,

$$\frac{\partial \mathbf{u}}{\partial \tilde{t}} \approx \mathbf{D}_0 \cdot \mathbf{u}. \tag{3.7}$$

Here $\mathbf{D}_0$ is the Jacobian of $\mathbf{G}$ evaluated at the uniform steady state for all parameters fixed at the typical values except $P_{ee} = 548.066$ and Γ_e. To study the response of the linear dynamics to Fourier mode perturbations, we define the wave vector,

$$\mathbf{u}[\tilde{x},\tilde{t}] = \mathbf{u}_0 \exp[\imath q\tilde{x} + \sigma\tilde{t}]. \tag{3.8}$$

Here $\mathbf{u}_0$ is the value of each dynamical variable ($\tilde{h}_e$, $\tilde{h}_i$, $\tilde{I}_{ee}$, $\tilde{J}_{ee}$, $\tilde{I}_{ei}$, $\tilde{J}_{ei}$, $\tilde{I}_{ie}$, $\tilde{J}_{ie}$, $\tilde{I}_{ii}$, $\tilde{J}_{ii}$, $\tilde{\phi}_e$, $\tilde{\psi}_e$, $\tilde{\phi}_i$, and $\tilde{\psi}_i$) in the uniform state solution. We note that these uniform states correspond to the fixed points of the dimensionless ODEs (shown for $h_e = -70$ mV $\times\tilde{h}_e$ in Figure 3.12(a), for example) with $\tilde{J}_{ee} = \tilde{J}_{ei} = \tilde{J}_{ie} = \tilde{J}_{ii} = \tilde{\psi}_e = \tilde{\psi}_i = 0$. The spatial and temporal dependence of $\mathbf{u}$ occurs in the exponential. The parameters q and σ correspond to the complex (dimensionless) wavelength and frequency, respectively. To determine the stability of the uniform state to Fourier mode perturbations we substitute (3.8) into (3.7) and solve for σ as a function of q and Γ_e. The resulting values of σ correspond to the eigenvalues of $\mathbf{D}_0$. Of the 14 values for σ, we focus on the one with largest real part, which we denote Max[σ]. In Figure 3.16 we plot Max[σ] as a function of q for four values of Γ_e. At $\Gamma_e = 0.970\times10^{-3}$, Max[$\sigma$] < 0 for all q. Thus, at this value of Γ_e, the uniform state is stable to the Fourier mode perturbations. For $\Gamma_e = 0.961\times10^{-3}$, Max[$\sigma$] > 0 and largest at $q = \pm 6$. Here, the uniform state is unstable to Fourier-mode spatial perturbations in the positive bands of Max[σ] surrounding $q = \pm 6$. We note that at $q = \pm 6$ the eigenvalue Max[σ] is complex with imaginary part -3.28. Therefore, the instability is oscillatory in time, and is called a Type I_0 linear instability [79]. We compute the (dimensionless) temporal frequency and (dimensionless) velocity from σ and q/σ, respectively, and determine the corresponding dimensional quantities 13 Hz and 3.8 m/s, respectively. At $\Gamma_e = 0.957\times10^{-3}$, we find an instability sets in at $q = 0$, and the uniform state itself becomes unstable. Here the imaginary part of Max[σ] at $q = 0$ is -3.03. Thus a spatially uniform perturbation will set the uniform state oscillating in time. This is called a Type III_0 linear instability [79]. We note that the value of Γ_e at the Type III_0 instability (determined from the dimensionless SPDEs with $\alpha = 0$) corresponds to the value of Γ_e at the rightmost Hopf bifurcation determined from the dimensionless ODEs— see Figure 3.12(a). In this way, the linear stability analysis relates the dimensionless SPDEs model to the simpler dimensionless ODEs model. Finally, we show in Figure 3.16 the value of Max[σ] for $\Gamma_e = 0.955\times10^{-3}$. Here the uniform state is unstable to Fourier-mode perturbations for wavelengths $-10.5 < q < 10.5$.

To confirm the results of the linear stability analysis, we compute numerical solutions to the dimensionless SPDEs. For this analysis, we fix all of the parameters at the typical values, except $P_{ee} = 548.066$ and Γ_e, both of which we make uniform in space and constant throughout the duration of each computation. In the three numerical solutions that follow, we perturb the uniform steady state by setting $\alpha = 0.001$ at $x = 350$ mm for the initial 10 ms of the simulation; otherwise, we set $\alpha = 0.0$. For the first two simulation results, we plot (dimensional) space on the horizontal axis, (dimensional) time on the vertical axis, and the value of h_e in linear greyscale with values of $h_e = -55$ mV and $h_e = -52$ mV shown in white and black, respectively. We show in Figure 3.17(a) the numerical solution of the

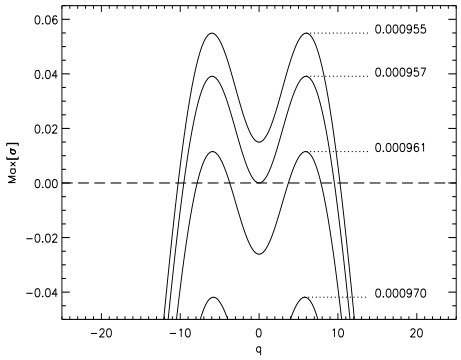

Figure 3.16: The eigenvalues of the linearized PDEs with largest real part — Max[σ] — as a function of the (dimensionless) wave vector q. The value of $P_{ee} = 548.066$ is the same for all curves. The value of Γ_e differs for each curve; we indicate the value of Γ_e to the right of the maximum of each curve. Max[σ] becomes positive for $\Gamma_e < 0.96 \times 10^{-3}$.

dimensionless SPDEs for $\Gamma_e = 0.970 \times 10^{-3}$. We find that oscillations initially occur in h_e, but quickly decay, in agreement with the linear stability analysis. In Figure 3.17(b), we plot the numerical solution of h_e for $\Gamma_e = 0.961 \times 10^{-3}$. Here we find that oscillations persist in h_e. These oscillations appear as the repeated light and dark ridges in Figure 3.17(b). We note that these oscillations occur in both time and space; careful inspection reveals the ridges are tilted with respect to the horizontal. We calculate the wave speed along each ridge for 100 mm $< x <$ 330 mm and 50 ms $< t <$ 440 ms, and find $v = -3.0 \pm 0.8$ m/s. We also compute the temporal frequency of maximum power for fixed spatial positions between 224 mm and 476 mm. We find $f_0 = 12.0 \pm 0.7$ Hz. Both results v and f_0 are in approximate agreement with the linear stability analysis.

In Figure 3.17(b) we illustrate the initial, transient state of the dynamics where the linear approximation (3.7) is valid. Continuing the numerical integration, we find that standing waves (SW) develop in the dynamics. We show these SW in Figures 3.18(a) and 3.18(b). The colorscale we use in both figures is identical to that used in Figure 3.17(b). We find that the SW increase in amplitude until traveling waves (TW) dominate the dynamics. We show this transition in Figure 3.18(c). Here we plot the value of h_e in linear greyscale over space-time with $h_e = -100$ mV in white and $h_e = 0.0$ mV in black. Initially the TW exhibit oscillations in both space and time. In the final state, shown in Figure 3.18(d), we find that the TW oscillate only in time.

As a last check of the linear stability analysis, we consider numerical solutions to the dimensionless SPDEs for $P_{ee} = 548.066$ and $\Gamma_e = 0.955 \times 10^{-3}$. We note that this value of Γ_e corresponds to the uppermost curve shown in Figure 3.16. To compute this numerical solution, we chose as initial conditions the uniform steady state values of the dimensionless SPDEs for $\Gamma_e = 0.970 \times 10^{-3}$ and $\alpha = 0.0$ for all space and time (i.e., no stochastic input.) We determined these uniform steady state values numerically. We then set $\Gamma_e = 0.955 \times 10^{-3}$ and solved the dimension-

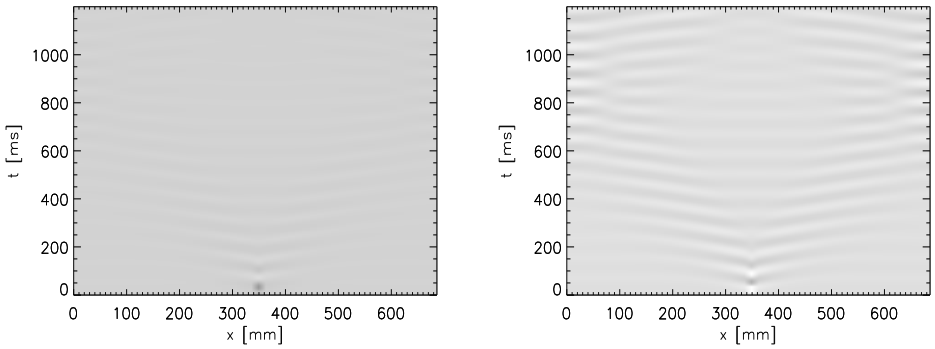

(a) (b)

Figure 3.17: Numerical solution to the dimensionless SPDEs with $P_{ee} = 548.066$, and periodic boundary conditions in space. Space (in mm) and time (in ms) are plotted along the horizontal and vertical axes, respectively. The value of h_e is plotted in linear greyscale over space-time with $h_e = -55$ mV in white and $h_e = -52$ mV in black. We perturb the dynamics by setting the noise term $\alpha = 0.001$ at $x = 350$ mm for 10 ms. We set $\alpha = 0.0$ otherwise. (a) Here $\Gamma_e = 0.970 \times 10^{-3}$. The oscillations in h_e are transient. (b) Here $\Gamma_e = 0.961 \times 10^{-3}$. Traveling waves develop in h_e with speed -3.0 ± 0.8 m/s and temporal frequency of 12.0 ± 0.7 Hz.

less SPDEs in the standard way. The initial conditions (determined at $\Gamma_e = 0.970 \times 10^{-3}$) act as spatially uniform perturbations to the steady state values of the dimensionless SPDEs for $\Gamma_e = 0.955 \times 10^{-3}$. In Figure 3.19(a), we plot this numerical solution of h_e for $\Gamma_e = 0.955 \times 10^{-3}$ and no stochastic input (i.e., $\alpha = 0.0$.) We plot (dimensional) space on the horizontal axis, (dimensional) time on the vertical axis, and the value of h_e in linear greyscale with values of $h_e = -100$ mV and $h_e = 0$ mV shown in white and black, respectively. After an initial transient, we find that h_e oscillates in time but not in space; the black and white ridges in the figure are horizontal. In Figure 3.19(b), we again plot the numerical solution of h_e for $\Gamma_e = 0.955 \times 10^{-3}$. But, in this simulation we include weak stochastic input ($\alpha = 0.0002$) uniform in space and time. We note that for the typical parameter values $\Gamma_e = 1.42 \times 10^{-3}$ and $P_{ee} = 11.0$, a stochastic input of $\alpha = 0.0002$ results in a standard deviation of 0.13 mV in h_e. The initial conditions used to compute this solution are identical to those used to create Figure 3.19(a). We find that h_e oscillates in both space and time; the light and dark ridges in this figure tilt toward increasing x.

We can employ the linear stability analysis to understand the results shown in Figures 3.19(a) and 3.19(b). For $\Gamma_e = 0.955 \times 10^{-3}$, we show in Figure 3.16 that the uniform steady state is unstable to a spatially uniform perturbation (i.e., Max$[\sigma] > 0$ at $q = 0$) and that a Type III$_0$ instability occurs. In the computation we use to create Figure 3.19(a), the initial conditions act as spatially uniform perturbations to this uniform steady state, and we find that temporal (but not spatial) oscillations occur in h_e. This corresponds to the Type III$_0$ instability determined from the linear

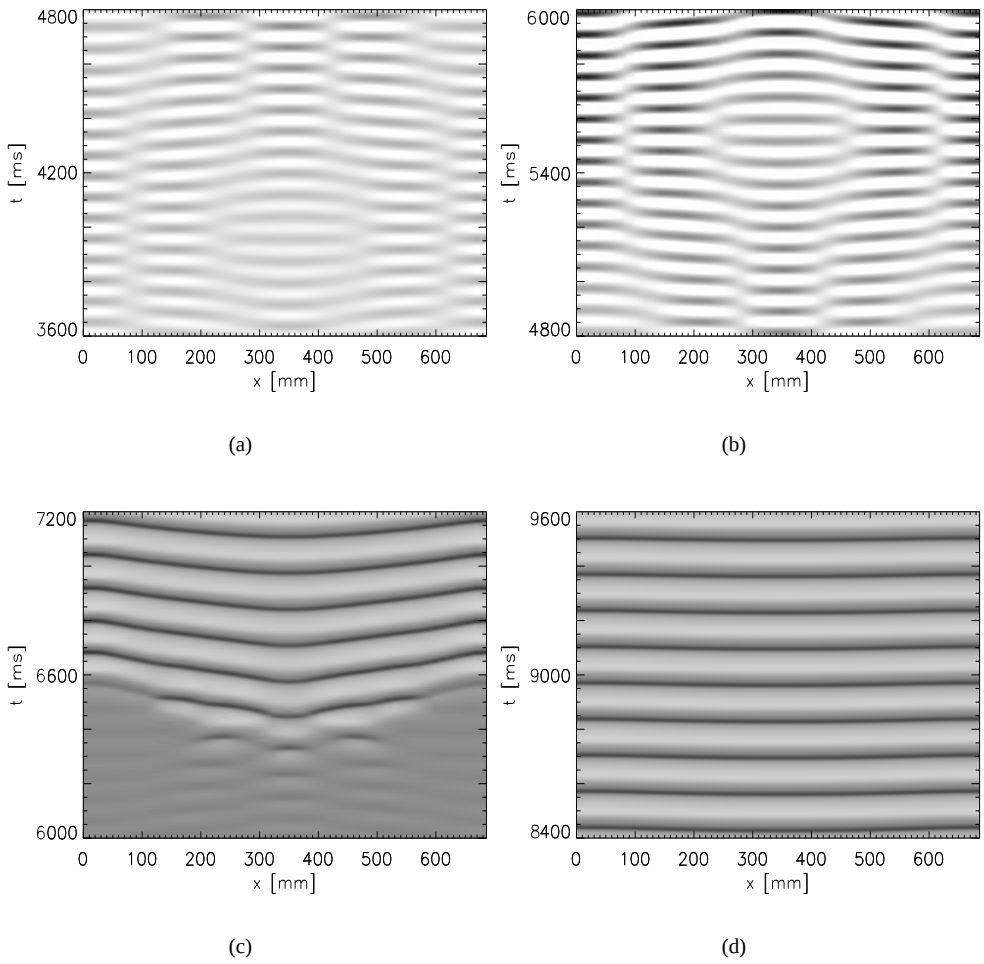

Figure 3.18: Continuation of the numerical solutions shown in Figure 3.17(b). (a)-(b) Here we show value of h_e for 3600 ms $< t <$ 6000 ms in linear greyscale over space-time with $h_e = -55$ mV in white and $h_e = -52$ mV in black. A pattern of standing waves occurs. (c)-(d) Here we show value of h_e for 6000 ms $< t <$ 7200 ms and 8400 ms $< t <$ 9600 ms in linear greyscale over space-time with $h_e = -100$ mV in white and $h_e = 0.0$ mV in black. Here traveling waves dominate the dynamics.

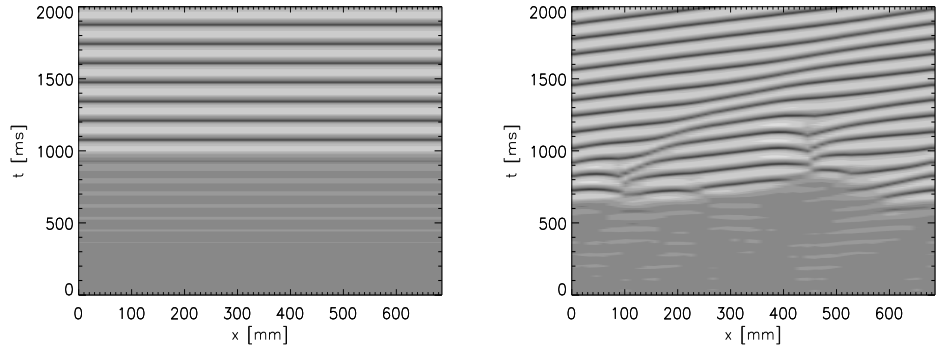

(a) (b)

Figure 3.19: Numerical solution to the dimensionless SPDEs with $P_{ee} = 548.066$, $\Gamma_e = 0.955 \times 10^{-3}$, and periodic boundary conditions in space. Space (in mm) and time (in ms) are plotted along the horizontal and vertical axes, respectively. The value of h_e is plotted in linear greyscale over space-time with $h_e = 0$ mV in black and $h_e = -100$ mV in white. Both figures start with the same initial conditions. (a) Here $\alpha = 0.0$. Oscillations in h_e occur in time, but not in space. (b) Here $\alpha = 0.0002$. Oscillation in h_e occur in both time and space.

analysis. To create Figure 3.19(b) we add stochastic input to the dynamics. This destroys the spatially uniformity of the perturbation. We therefore expect the uniform state to destabilize in a Type I_0 linear instability, and both spatial and temporal waves to occur in h_e. We indeed show that this occurs in Figure 3.19(b).

We have shown in numerical simulations that stable TW occur in the model dynamics. We expect that near a Hopf bifurcation on the line with periodic boundary conditions both TW and SW occur, and that at most one can be stable [80]. We showed in Figures 3.18(b) and 3.18(c) an example of transient SW in the model dynamics. Here we show another example of SW in the dynamics and that these waves are unstable to small perturbations. To do so we compute a numerical solution to the dimensionless SPDEs with $P_{ee} = 548.066$, $\Gamma_e = 0.961 \times 10^{-3}$ — near the Hopf bifurcation in the ODEs. We have already computed the linear stability analysis of the uniform state at these parameter values and found that the uniform state is unstable. We showed this result in Figure 3.15 (the second curve from the bottom.) To produce a SW in the dynamics we first set the noise to zero ($\alpha = 0.0$), and make the boundary conditions periodic. As initial conditions we set h_e to be a sinusoidal perturbation of the uniform state with period 199 mm and amplitude 5 mV. We note that this period corresponds to the (dimensionless) wavelength $q = 8.8$ defined in (3.8) and that this value lies near the rightmost positive value of Max[σ] we show in Figure 3.15. We calculate the solution for 8000 s and show the results for the last 2000 s in Figure 3.20(a). Here we plot h_e in linear greyscale with values of $h_e = -55$ mV in white and $h_e = -54$ mV in black. We find a standing wave pattern with spatial period 199 mm (identical to the initial perturbation,) temporal period near 75 ms, and amplitude less than 1 mV.

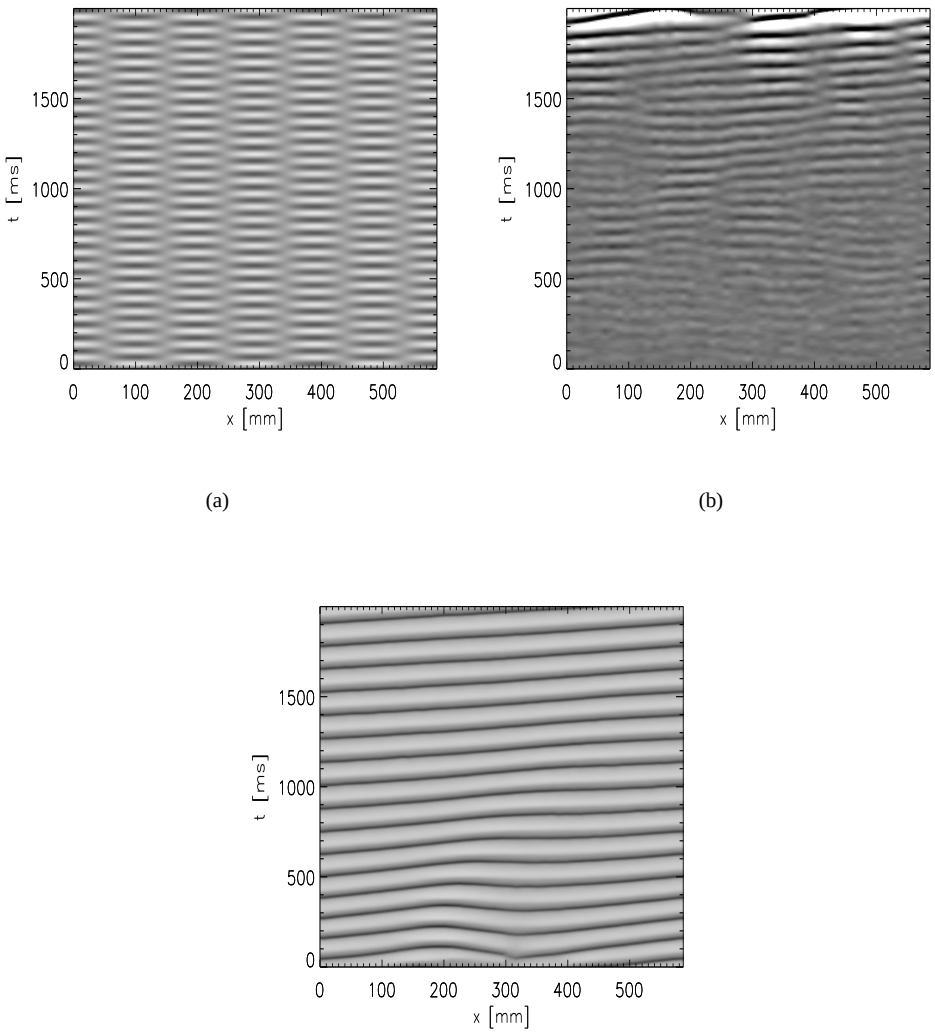

(a)

(b)

(c)

Figure 3.20: Numerical solutions to the dimensionless SPDEs with $P_{ee} = 548.066$ and $\Gamma_e = 0.961 \times 10^{-3}$. (a) Standing waves. The last 2000 ms of a numerical simulation lasting 8000 ms with no stochastic input. We set the initial conditions in h_e to be sinusoidal with period 199 mm (one-third of the entire spatial domain.) The value of h_e is plotted in linear greyscale with $h_e = -55$ mV in white and $h_e = -54$ mV in black. (b) Noise destroys the standing waves. As initial conditions we choose the values of the fourteen dynamical variables at the end of the simulation ($t = 2000$ ms) shown in (a) and fix $\alpha = 0.0002$. The value of h_e is plotted in linear greyscale with $h_e = -60$ mV in white and $h_e = -50$ mV in black. (c) Continuation of (b). The value of h_e is plotted in linear greyscale with $h_e = -100$ mV in white and $h_e = 0.0$ mV in black. Stable TW persist.

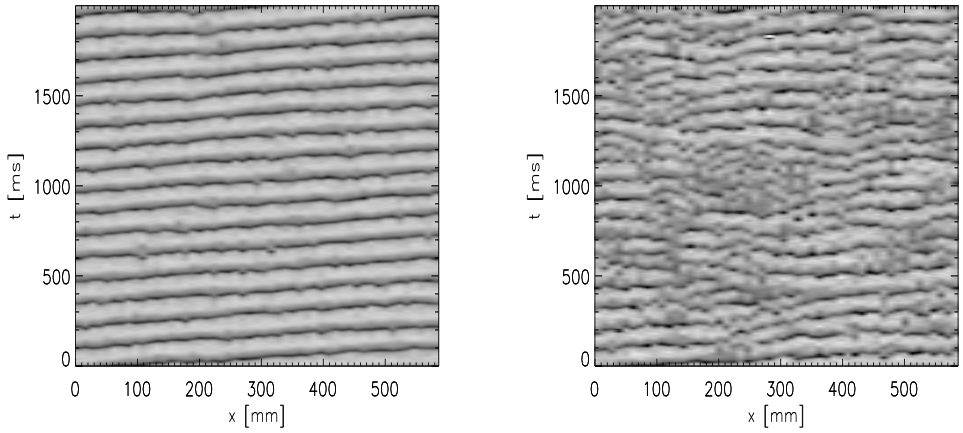

(a) (b)

Figure 3.21: Numerical solutions to the dimensionless SPDEs with $P_{ee} = 548.066$, $\Gamma_e = 0.961 \times 10^{-3}$, and initial conditions fixed by the final values (at $t = 2000$ ms) of the simulation shown in Figure 3.20(c). (a) $\alpha = 0.002$. TW persist. (b) $\alpha = 0.005$. Careful inspection reveals transient traveling waves.

To test the stability of the SW, we add low amplitude noise to the dynamics shown in Figure 3.20(a). We use the same parameter values and boundary conditions as those used to create the SW pattern, and set the noise term $\alpha = 0.0002$. We show the results of this numerical simulation in Figure 3.20(b). Here we plot h_e in linear greyscale with values of $h_e = -60$ mV in black and $h_e = -50$ mV in white. On this scale, the SW near $t = 0$ ms are not visible. We find that after an initial transient, TW of large amplitude develop near $t = 1800$ ms. We show the continuation of this simulation in Figure 3.20(c). Here we plot h_e in linear greyscale with values of $h_e = -100$ mV in black and $h_e = 0$ mV in white. In this figure the TW are clear.

To show that the TW are stable, we increase the noise term by a factor of 10 (i.e., we set $\alpha = 0.002$) and continue the simulation shown in Figure 3.20(c) where the stochastic input was weak. (We continue the simulation by using the fourteen variables at the last time step ($t = 2000$ ms) in Figure 3.20(c) as initial conditions for the fourteen variables in this simulation.) We show the results in Figure 3.21(a); we find that the TW persists. When we fix $\alpha = 0.005$ (an increase in the noise by a factor of 25) and continue the simulation with weak stochastic input, we find that noise dominates the dynamics. We show this result in Figure 3.21(b). Careful inspection reveals transient TW that propagate to the left and the right. Thus, even with large stochastic input, (rough) TW still persist.

We conclude that both TW and SW occur near the Hopf bifurcation. We find that the SW are unstable to weak stochastic inputs which perturb the SW to a TW. We have computed numerous realizations (here and in the rest

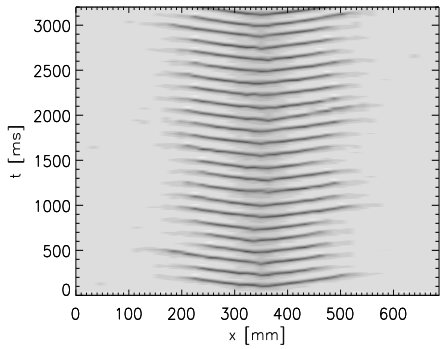

Figure 3.22: Numerical solution to the dimensionless SPDEs with parameters: $\Gamma_e = 0.87 \times 10^{-3}$, $\alpha = 0.001$, P_{ee} a Gaussian function in space with maximum 548.066 at $x = 350$ mm and full width at half maximum 46 mm, and periodic boundary conditions in space. Space (in mm) and time (in ms) are plotted along the horizontal and vertical axes, respectively. The value of h_e is plotted in linear greyscale with $h_e = -100$ mV in white and $h_e = 0.0$ mV in black. Waves in h_e travel outward from the region of hyperexcitation near $x = 350$ mm with approximate speed 1.2 m/s and approximate frequency 7.5 Hz.

of this work) of the dimensionless SPDEs, and found many occurrences of TW. In this section, we showed that the TW are stable to much larger (by a factor of 10 to 25) stochastic inputs than are the SW. In our application of interest — modeling the human cortex — we expect stochastic input always occurs. This input may represent a true stochastic process (e.g., the diffusion of synaptic vesicles across a synaptic cleft) or an approximation to an unknown deterministic process. We conclude that TW — which are robust to stochastic input — are more important than the unstable SW for modeling cortical electrical activity during seizure.

Having computed the linear stability analysis for four values of Γ_e, we state three important results. First, the agreement between the linear stability analysis with the numerical simulations instills confidence that the numerical calculations are correct. Second, in the linear stability analysis we relate the solutions of the simplified dimensionless ODEs to uniform state solutions of the dimensionless SPDEs. We find that a Hopf bifurcation in the dimensionless ODEs correspond to a destabilization of the uniform state in the dimensionless SPDEs. Third, we use the linear stability analysis to identify the types of instabilities (Type I_0 and Type III_0) that develop. In what follows we compare the frequency (~ 12 Hz) and wave speed (~ 3 m/s) determined here with the clinical ECoG data. Before doing so, we compute two more numerical solutions to the dimensionless SPDEs for different spatial and temporal distributions of P_{ee}.

We start by computing numerical solutions to the dimensionless SPDEs for P_{ee} nonuniform in space and constant in time. Here we set P_{ee} to be a Gaussian function in x with maximum $P_{ee}^* = 548.066$ at $x = 350$ mm, full width at half maximum of 46 mm, and minimum $P_{ee} = 11.0$. The localized region of hyperexcitation near $x = 350$ mm may

be thought of as the seizure focus in our simple model. We solve the dimensionless SPDEs with $\Gamma_e = 0.87 \times 10^{-3}$, $\alpha = 0.001$ (both uniform in space and time) and show the solution in Figure 3.22. We find that localized oscillations (the dark ridges in Figure 3.22) emerge from the region of hyperexcitation near $x = 350$ mm, travel outward with approximate speed 1.2 m/s and approximate frequency 7.5 Hz, and then dissolve in the regions of lower excitation, where $P_{ee} \to 11.0$. This localized oscillatory activity is more representative of a localized seizure than the global oscillations illustrated in Figure 3.17(b). We note that this pattern of spatially confined traveling waves is also found to occur in other dynamical systems with spatially uniform parameter values [81, 82].

In the final example, we compute numerical solutions to the dimensionless SPDEs for P_{ee} nonuniform in space and time. As in the previous example, we fix $\Gamma_e = 0.87 \times 10^{-3}$ and $\alpha = 0.001$ (both uniform in space and time.) But, unlike the previous example, we vary P_{ee} in time. At $t = \{0, 5000\}$ ms, we fix $P_{ee} = 11.0$ uniform in space. For 500 ms $< t <$ 5000 ms, we set P_{ee} to be a Gaussian function in x with maximum P^*_{ee} at $x = 350$ mm, full width at half maximum of 46 mm, and minimum $P_{ee} \to 11.0$. At $t = \{500, 1000, 1500, 2000, 2500\}$ ms we increase P^*_{ee} in steps of 100 so that $P^*_{ee} = \{110, 210, 310, 410, 510\}$, respectively. These increases are marked by the solid vertical lines in Figure 3.23(a). We then decrease P^*_{ee} in steps of 100 so that for $t = \{3000, 3500, 4000, 4500\}$ ms, $P^*_{ee} = \{410, 310, 210, 110\}$, respectively. These decreases are marked by the dashed lines in Figure 3.23(b). We show in Figure 3.23 that localized oscillations in h_e (the dark ridges) begin at $t = 1900$ ms, where $P^*_{ee} = 310$. The frequency of these oscillations increase when we increase P^*_{ee} to 510 at $t = 2500$ ms. Then, as we decrease P^*_{ee} between 3000 ms $< t <$ 5000 ms, the oscillations in h_e decrease in frequency and eventually disappear.

Waves in continuum models of the human cortex are not new. In [61], the authors investigate the *dimensional* SPDEs and show that spatial modes develop when the corticortical $e \to i$ diffusivity dominates the corticortical $e \to e$ diffusivity. In [83] the authors show that spatiotemporal patterns (reminiscent of the seizing cortex) occur in a continuum model of cortical electrical activity with a single inhomogeneous connection. By adjusting the extent of this inhomogeneous connection, the stability of the spatiotemporal patterns changes. Also, in [52] the authors show how traveling waves may develop in a model derived from the physiology of a neocortical slice.

Waves in continuum models of the human cortex are not new. In [61], the authors investigate the *dimensional* SPDEs and show that spatial modes develop when the corticocortical $e \to i$ diffusivity dominates the corticocortical $e \to e$ diffusivity. In [83] the authors show that spatiotemporal patterns (reminiscent of the seizing cortex) occur in a continuum model of cortical electrical activity with a single inhomogeneous connection. By adjusting the extent of this inhomogeneous connection, the stability of the spatiotemporal patterns changes. Also, in [52] the authors show how traveling waves may develop in a model derived from the physiology of a neocortical slice.

The last example provides a crude model for the evolution of the seizing cortex. At normal levels of subcortical

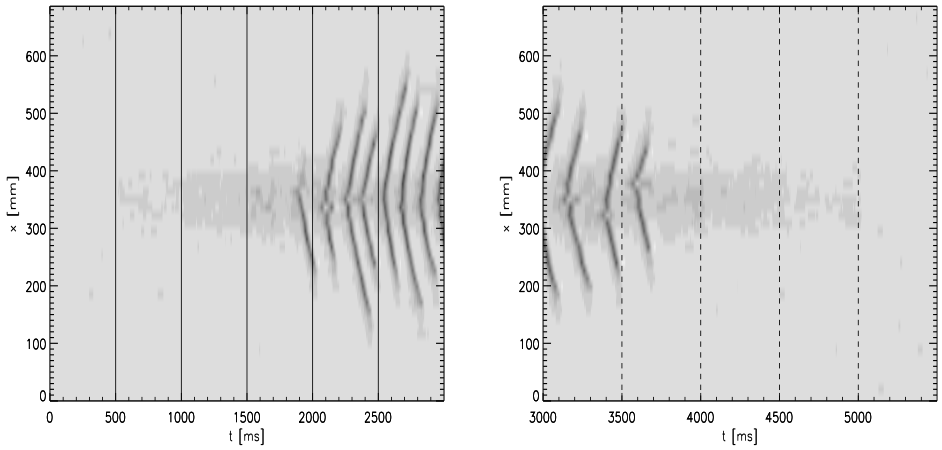

(a) (b)

Figure 3.23: Numerical solution to the dimensionless SPDEs with parameters $\Gamma_e = 0.87 \times 10^{-3}$, $\alpha = 0.001$, and periodic boundary conditions in space. At $t = \{0, 5000\}$, $P_{ee} = 11.0$ uniform in space. For 500 ms $< t <$ 5000 ms P_{ee} is a Gaussian function in space with maximum P^*_{ee} at $x = 350$ mm and full width at half maximum 46 mm. In subfigure (a), the maximum $P^*_{ee} = \{110.0, 210.0, 310.0, 410.0, 510.0\}$ at $t = \{500, 1000, 1500, 2000, 2500\}$ ms, respectively. These increases in P^*_{ee} are denoted by the solid vertical lines. In subfigure (b), the maximum $P^*_{ee} = \{410.0, 310.0, 210.0, 110.0\}$ at $t = \{3000, 3500, 4000, 4500\}$ ms, respectively. These decreases in P^*_{ee} are denoted by the dashed vertical lines. Space (in mm) and time (in ms) are plotted along the vertical and horizontal axes, respectively. The value of h_e is plotted in linear greyscale with $h_e = -100$ mV in white and $h_e = 0.0$ mV in black. Waves in h_e are localized in space and time to the region of hyperexcitation near $x = 350$ mm for 1800 ms $< t <$ 3800 ms.

excitation ($P_{ee} = 11.0$) there exist only disorganized spatiotemporal fluctuations in h_e and no pathological oscillatory activity. Only when P^*_{ee} exceeds a threshold level do localized oscillations in h_e appear. As the subcortical excitation is increased further, the frequency of the oscillations increases. Then, as P^*_{ee} is decreased, the oscillations slow and eventually disappear. In the next section we compare frequencies and waves speeds determined here for the dimensionless ODEs and dimensionless SPDEs to those determined from the clinical ECoG data.

3.6 Results

In Section 3.2 we analyzed ECoG data recorded from four human subjects during seizure, and in Sections 3.3 - 3.5 we determined numerical solutions to a continuum model of cortical electrical activity. We compared the observational and model results by computing two quantities: f_0 and v. To summarize the observational results, we average f_0 and the magnitude of v over the electrodes considered for each subject (i.e., over two electrodes for Subject 1, three electrodes for Subject 2, and nine electrodes for Subject 3 and Subject 4.) We tabulate these results in Table 3.5. We also list the results for the simulated data in Table 3.6. We note that, in general, the results of the simulations agree with the observed data for f_0 (within a factor of two) and v in I1 and I2 (within a factor of four.)

The first goal in this chapter was to consider the potential of the SPDEs to provide a model of the mesoscopic electrical activity on the seizing cortex. In our analysis of the dimensionless ODEs we have shown that there do exist limit cycles in h_e associated with Hopf bifurcations in the dynamics. We have also shown that the simpler dimensionless ODEs suggest behavior in the complicated dimensionless SPDEs that is consistent with the clinical seizure data. Specifically, we have shown that at typical parameter values $\Gamma_e = 1.42 \times 10^{-3}$ and $P_{ee} = 11.0$, a reduction in Γ_e (to $\Gamma_e = 1.20 \times 10^{-3}$) produced oscillatory behavior in h_e. But this oscillatory behavior was transient and did not produce the large amplitude, stable oscillations characteristic of the seizing cortex. Moreover, this oscillatory behavior occurred at a single value of Γ_e. Thus the parameter values of the model cortex would have to be carefully tuned to reach this point.

To increase the excitability of the model cortex and make it "seize", we increased P_{ee}. We show in Figures 3.12(a) and 3.15(a) that for $P_{ee} > 250.0$ there exist stable, large amplitude limit cycles in h_e over a wide range of Γ_e. We show in Section 3.5 that these oscillations are associated with traveling wave dynamics in the dimensionless SPDEs. Thus to produce behavior in h_e consistent with that observed in the seizing cortex, we must: 1) increase P_{ee}, and 2) decrease Γ_e in the dimensionless SPDEs. In dimensional terms, we must increase the subcortical excitation p_{ee} or decrease the maximum firing rate S^{max}, and we must increase the EPSP neurotransmitter rate constant γ_e or the difference between the reversal and resting potentials $|h_e^{\rm rev} - h^{\rm rest}|$, or decrease the peak excitatory postsynaptic potential G_e or S^{max}.

That we must decrease Γ_e to induce a seizure seems counterintuitive. We expect that an increase in the strength of excitatory inputs would promote seizing activity. But, the decrease in Γ_e, from 1.42×10^{-3} to 0.87×10^{-3} used to create Figure 3.23, represents only a 39% change. The change in P_{ee} required to induce a seizure is much larger; we show in Figure 3.23 that this parameter must increase by at least 2700%. We may interpret the changes in these two parameters required for seizure induction following the models in [75]. Alterations of the epileptic brain, due to genetic or environmental (e.g., injury) effects, for example, predispose it to seizures. In modeling the epileptic cortex we may interpret this predisposition as a permanent (model I) or a gradual (model II or model III) change of a model parameter. The results shown in Figure 3.23 illustrate the latter case; with Γ_e fixed, a gradual increase in P_{ee} induces seizing activity in h_e. Because the change in P_{ee} is gradual and effects the dynamics of h_e we could try to anticipate these types of seizures. We may also interpret these results following the model I framework. For example, consider a permanent increase of P_{ee} from 11.0 to 310.0. When modeling the cortical activity of any individual (either healthy or epileptic), we may assume that the model parameters undergo routine fluctuations in their normal values. In healthy individuals (with the typical parameter value $P_{ee} = 11.0$) a small negative fluctuation in the model parameter Γ_e may induce a harmless, transient oscillation (like that shown in Figure 3.11) but not a seizure. This same fluctuation in Γ_e will cause the predisposed epileptic cortex to seize. In this case, the increased value of P_{ee} allows the dynamics to cross the separatrix (or boundary) between the normal and seizing states [84]. Thus, only a small change in Γ_e is necessary to produce pathological oscillations in h_e. Because a random fluctuation in Γ_e induces the seizure, these types of seizures cannot be anticipated. From the results presented here we suggest a large change in P_{ee} and a small change in Γ_e may provide a model of the seizing cortex.

In Tables 3.5 and 3.6 we compute two results, the average peak frequency f_0 and the average propagation speed v, derived from clinical ECoG recordings and solutions to the SPDEs. We find that the values derived from the observational and model data approximately agree (f_0 within a factor of 2, and v in I1 within a factor of 4) but note the following important issues. First, the subdural electrode strips and electrode grids used in the clinical recordings consist of electrodes separated by 10 mm. Thus, the spatial sampling of the cortex is poor and we cannot observe detailed wave behavior in the voltage. It may be true that two electrodes lie on either side of a sulcus (a groove or furrow in the cortex); the precise electrode locations are not known. It may also be true that a wave in electrical potential is propagating obliquely with respect to the shortest path between two electrodes. Future recordings that utilize high density electrode grids with small inter-electrode spacing would provide better results to compare with the theory. Second, the lead/lag relationships determined from the WCC are ambiguous. For example, we showed in Figure 3.3 that for 17.5 s $< t <$ 27 s, the oscillations at electrode X lead the oscillations at electrode Y by approximately 25 ms. During this interval, these time series are nearly sinusoidal with a well defined frequency near 4 Hz; see the data in Figure 3.1(b) or the WPS in Figure 3.2. The cross correlation of two sinusoids is itself a sinusoid, and therefore

ambiguous; although we suggest X leads Y by approximately 25 ms, it is also true that Y leads X by approximately 225 ms (the period of the 4 Hz cycle minus 25 ms.) We chose the case X leads Y for two reasons: 1) the amplitude of oscillations in X is bigger than in Y, and 2) a correlation at 25 ms between two closely spaced electrodes is more reasonable than a correlation of 225 ms. It does not seem possible to resolve this ambiguity of the cross correlation. Third, we have assumed that the same voltage wave front passes through neighboring electrodes. If the wave source lies between two electrodes, this assumption is incorrect. Smaller electrode spacing may help locate the wave source more accurately. Fourth, given such a complicated model (14 nonlinear first order stochastic differential equations and 20 parameters) we could, perhaps, produce any desired behavior in h_e by properly tuning the parameters. Here we chose to adjust two parameters, both related to the excitation of the model cortex; in this way, we used the physiology of the seizing cortex to constrain the adjustable parameters in the model. In Section 3.8 we show other parameter changes that results in seizure-like oscillations in the model. Finally, we do not mean to suggest that the SPDEs provide an accurate model of all human cortical seizure activity. Here we have only compared the model results with data collected from four subjects, and shown that the model and observational data agree in an approximate way.

Although confounding factors exist both in the model and observations, these results still illustrate an important use of the SPDEs and other continuum models: establishing links between the known ECoG data and unknown cortical physiology. In most clinical analysis no attempt is made to link the changes observed in ictal ECoG time series with corresponding changes in cortical physiology. Continuum models of cortical electrical activity allow one to consider such links in a quantitative way. This is especially important for human cortical data, where invasive procedures are inappropriate. For example, in [84] the authors consider an ODE model of the corticothalamic network; unlike the SPDEs model presented here, these models explicitly include the interactions of cortical neurons with the thalamus. The authors show that the model can produce the $3-$Hz spike wave characteristic of absence seizures and how the model parameters relate to the period of the seizures. In this chapter we relate the emergence of pathological oscillations in the measured cortical voltage to changes in two parameters: a small decrease in Γ_e and a large increase in P_{ee}. In this way, we suggest a link between the ECoG data and the physiology of the cortex. In the next section, we use the mathematical model to suggest two methods for aborting seizure-like oscillations in the dynamics.

3.7 Bifurcation control of the seizing cortex

In Section 3.6 we established the validity of the dimensionless SPDEs as an approximate model of the electrical activity of the seizing human cortex. We compared two quantities — f_0 and v — determined from ictal ECoG data recorded from four human subjects and from the results of the dimensionless SPDEs, and showed that the observed and

simulated results agree. We concluded that the model system — derived from human cortical physiology — provides an accurate approximation to the propagation of electrical signals in the seizing human cortex. In this section, we use the dimensionless SPDEs to explore two methods for controlling the seizing cortex.

For most epileptics invasive, electrical control is unnecessary. Unfortunately, an estimated 20% of people with epilepsy do not respond to medications prescribed to control seizures [85]. For these patients, treatment options are more invasive. Some patients may choose to undergo resective surgery, in which surgeons remove the epileptogenic zone. When the epileptogenic zone includes eloquent cortex (e.g. motor or speech cortex) resective surgery may not be safe, and the patient must consider alternative treatments. Brain electrical stimulation (BES) represents an important new treatment for intractable epilepsy. The most common — and only FDA approved — BES method is vagus nerve stimulation. In this method, electrodes (attached to a battery powered computer implanted subcutaneously on the patient's chest wall) periodically deliver electrical pulses to the vagus nerve. This chronic stimulation of the vagus nerve is thought to affect brain regions (e.g., the thalamus) that might, in theory, increase cortical inhibition and thereby lessen or modulate seizures. Other, as yet experimental, BES methods target brain regions such as the cerebellum, caudate nucleus, and thalamus. The physiological mechanisms by which these BES methods prevent or reduce seizures are unknown.

Seizures may also be aborted by direct electrical stimulation of the cortex. For example, cortical afterdischarges (seizure-like activity elicited by direct cortical electrical stimulation used for brain mapping) may be arrested by applying brief bursts (0.3 s $-$2.0 s) of pulse stimulation (0.3 ms duration biphasic pulses delivered 50 times per second at 1.0 mA $-$15.0 mA) to the cortex [86, 87]. Others have found that biphasic pulses delivered at high frequencies (e.g., 200 Hz in [88]), moderate frequencies (e.g., 50 Hz in [89]), and low frequencies (e.g., 0.9 Hz in [89]) can reduce seizure activity. However, not all stimulation frequencies are appropriate. Moderate frequency (5 Hz $-$20 Hz) stimulation delivered for 5 s $-$12 s may, in fact, increase baseline epileptiform activity [90].

For cortical BES, there may exist optimal stimulation sites, transducers, and parameters for terminating seizures. Of course, the most important consideration for physicians and researchers is patient safety. Animal models of epilepsy may allow researchers to explore different BES methods that may pose unacceptable risks to human subjects. For example, in [91] the authors show that small, uniform electric fields — directed from the soma to the apical dendrites — transiently suppress epileptiform activity in rat hippocampal slices *in vitro*. An improvement to this method is reported in [92], where the authors apply time varying electric fields via a continuous, proportional feedback algorithm to rat hippocampal slices *in vitro*. They find that this feedback controller reduces seizure-like activity with more success than the uniform electric fields.

Our goal in this section is a theoretical exploration of new BES techniques. In what follows, we apply two feed-

back controllers — a proportional controller and a differential controller, — to the dimensionless SPDEs. Others have employed mathematical systems to model the effects of BES [93, 94]. In those works, the authors considered the activity of individual neurons and networks of neurons. Here we study the model of mesoscale cortical electrical activity defined in Section 3.3. In subsection 3.7.1 we apply the linear proportional feedback controller to the (dimensionless) model variable $\tilde{h}_e$ — the spatially averaged soma membrane potential of excitatory cortical neurons. We show that, when the controller gain exceeds a threshold value, the controller suppresses seizure-like oscillations occurring in the dynamics. The controller works through control of bifurcations; to make the discussion precise we utilize the taxonomy introduced in [76]. We discuss the types of bifurcations that both produce (subHopf/fold cycle) and destroy the large amplitude, stable oscillations characteristic of a seizure. In subsection 3.7.2 we apply a differential controller to the dynamics. Here we do not attempt to apply rigorous control theory. (The literature is vast; see, for example, [95].) Instead, we illustrate the effects of each controller on the bifurcations present in the dynamics. We show that both controllers suppress seizure-like oscillations — although bifurcation analysis is not as readily performed for these controllers. In Section 3.7.4 we discuss the results and possible future applications.

In what follows, in the interest of simplicity, we do not employ the full dimensionless SPDEs. Instead, we ignore the spatial dependence and stochastic input of the dimensionless SPDEs, and consider a simpler system of ODEs. We examined these dimensionless ODEs in Section 3.4 to gain insight into the complete system and in Section 3.5 found that Hopf bifurcations in the dimensionless ODEs correspond to traveling waves in the complete dimensionless

SPDEs. We state the dimensionless ODEs here:

$$\frac{\partial \tilde{h}_e}{\partial \tilde{t}} = 1 - \tilde{h}_e + \Gamma_e\left(h_e^0 - \tilde{h}_e\right)\tilde{I}_{ee} + \Gamma_i\left(h_i^0 - \tilde{h}_e\right)\tilde{I}_{ie} \tag{3.9a}$$

$$\frac{\partial \tilde{h}_i}{\partial \tilde{t}} = 1 - \tilde{h}_i + \Gamma_e\left(h_e^0 - \tilde{h}_i\right)\tilde{I}_{ei} + \Gamma_i\left(h_i^0 - \tilde{h}_i\right)\tilde{I}_{ii} \tag{3.9b}$$

$$\frac{\partial \tilde{I}_{ee}}{\partial \tilde{t}} = \tilde{J}_{ee} \tag{3.9c}$$

$$\frac{\partial \tilde{J}_{ee}}{\partial \tilde{t}} = -2T_e\tilde{J}_{ee} - T_e^2\tilde{I}_{ee} + T_e\left(N_e^\beta \tilde{S}_e[\tilde{h}_e] + \tilde{\phi}_e + P_{ee}\right) \tag{3.9d}$$

$$\frac{\partial \tilde{I}_{ei}}{\partial \tilde{t}} = \tilde{J}_{ei} \tag{3.9e}$$

$$\frac{\partial \tilde{J}_{ei}}{\partial \tilde{t}} = -2T_e\tilde{J}_{ei} - T_e^2\tilde{I}_{ei} + T_e\left(N_e^\beta \tilde{S}_e[\tilde{h}_e] + \tilde{\phi}_i + P_{ei}\right) \tag{3.9f}$$

$$\frac{\partial \tilde{I}_{ie}}{\partial \tilde{t}} = \tilde{J}_{ie} \tag{3.9g}$$

$$\frac{\partial \tilde{J}_{ie}}{\partial \tilde{t}} = -2T_i\tilde{J}_{ie} - T_i^2\tilde{I}_{ie} + T_i\left(N_i^\beta \tilde{S}_i[\tilde{h}_i] + P_{ie}\right) \tag{3.9h}$$

$$\frac{\partial \tilde{I}_{ii}}{\partial \tilde{t}} = \tilde{J}_{ii} \tag{3.9i}$$

$$\frac{\partial \tilde{J}_{ii}}{\partial \tilde{t}} = -2T_i\tilde{J}_{ii} - T_i^2\tilde{I}_{ii} + T_i\left(N_i^\beta \tilde{S}_i[\tilde{h}_i] + P_{ii}\right) \tag{3.9j}$$

$$\frac{\partial \tilde{\phi}_e}{\partial \tilde{t}} = \tilde{\psi}_e \tag{3.9k}$$

$$\frac{\partial \tilde{\psi}_e}{\partial \tilde{t}} = -2\lambda_e\tilde{\psi}_e - \lambda_e^2\tilde{\phi}_e + \lambda_e N_e^\alpha \frac{\partial \tilde{S}_e[\tilde{h}_e]}{\partial \tilde{t}} + \lambda_e^2 N_e^\alpha \tilde{S}_e[\tilde{h}_e] \tag{3.9l}$$

$$\frac{\partial \tilde{\phi}_i}{\partial \tilde{t}} = \tilde{\psi}_i \tag{3.9m}$$

$$\frac{\partial \tilde{\psi}_i}{\partial \tilde{t}} = -2\lambda_i\tilde{\psi}_i - \lambda_i^2\tilde{\phi}_i + \lambda_i N_i^\alpha \frac{\partial \tilde{S}_e[\tilde{h}_e]}{\partial \tilde{t}} + \lambda_i^2 N_i^\alpha \tilde{S}_e[\tilde{h}_e]. \tag{3.9n}$$

These fourteen differential equations are similar to those in (3.5) except that we have ignored the spatial derivatives in (3.5l) and (3.5n), and the stochastic inputs ($\tilde{\Gamma}_1$, $\tilde{\Gamma}_2$, $\tilde{\Gamma}_3$, and $\tilde{\Gamma}_4$) in (3.5d), (3.5f), (3.5h), and (3.5j). In what follows we apply a linear and differential feedback controller to the dynamics in subsections 3.7.1 and 3.7.2, respectively. We show that both controllers can prevent seizures (i.e., the large amplitude oscillations illustrated in Figure 3.12(b)) from occurring in the dynamics.

3.7.1 Linear controller

We could attempt to control the model system through many different methods; a controller may depend on any of the 14 variables or 20 parameters, and may apply to any of the 14 differential equations in (3.9). Here we employ

practical considerations to constrain the form of the controller. Most of the model variables and parameters (e.g., $\tilde{\phi}_e$ — the corticocortical input to excitatory cortical neurons, or N_e^{α} — the total number of synaptic connections from distant excitatory neurons to excitatory cortical neurons) are difficult to observe and perhaps impossible to manipulate in practice. The main observable in the model is $\tilde{h}_e$ which is proportional to the (dimensional) voltage h_e recorded in the ECoG. In practice, it is possible to manipulate cortical voltages through applied electric fields: an applied electric field polarizes the excitatory (i.e., pyramidal) neurons and thus alters the transmembrane potentials [96, 97]. Following these practical considerations, we implement a controller that depends only on the variable $\tilde{h}_e$ and effects only (3.9a).

We must still choose the form of the controller. In this section, we set the controller to be linear in $\tilde{h}_e$. Linear feedback controllers have been shown to ameliorate seizures in rat hippocampal brain slices *in vitro* [92]. To apply the linear controller, we redefine (3.9a) as,

$$\frac{\partial \tilde{h}_e}{\partial \tilde{t}} = 1 - \tilde{h}_e + \Gamma_e\left(h_e^0 - \tilde{h}_e\right)\tilde{I}_{ee} + \Gamma_i\left(h_i^0 - \tilde{h}_e\right)\tilde{I}_{ie} + a\,\tilde{h}_e, \tag{3.10}$$

where the controller is the last term in the equation, and the parameter a represents the controller gain.

To determine how the controller affects the dynamics, we compute bifurcation diagrams of (3.9) with (3.9a) replaced by (3.10). We compute each bifurcation diagram with all parameters fixed at the typical values (listed in Table 3.4) except for P_{ee} and Γ_e. In each bifurcation diagram, we plot the (dimensional) variable h_e as a function of the (dimensionless) parameter Γ_e. We note that the typical values of P_{ee} and Γ_e are 11.0 and 1.42×10^{-3}, respectively. In the next subsection we consider the "hyper-excited" model for which we set $P_{ee} = 548.066$ (at nearly fifty times the typical value.) We will show that, without the feedback controller, the variable h_e undergoes large amplitude oscillations characteristic of a seizure at a pathological combination of parameters. However, by setting an appropriate value for the controller gain a it is possible to abort these oscillations.

The pathological case of hyper-excitation: $P_{ee} = 548.066$

Here we set the parameter $P_{ee} = 548.066$; we found in Section 3.6 that this value of P_{ee} produced dynamics in h_e similar (in frequency and wave speed) to ictal ECoG data. We showed in Figure 3.12(a) a bifurcation diagram of (3.9) without the applied controller (i.e., $a = 0$ in (3.10).) We found two Hopf bifurcations in that figure and determined that the model "seizes" — large amplitude oscillations occur in h_e — for values of Γ_e between the two saddle node bifurcations of limit cycles (i.e., $0.67 \times 10^{-3} < \Gamma_e < 1.1 \times 10^{-3}$.) We show these large amplitude oscillations in h_e in Figure 3.12(b).

Having considered the uncontrolled dynamics ($a = 0.0$), we now consider the controlled case. In Figure 3.24 we

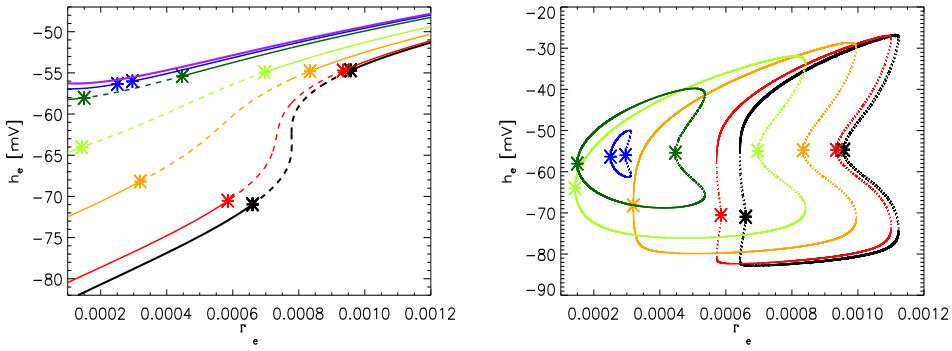

(a) (b)

Figure 3.24: Bifurcation diagrams for the uncontrolled and controlled dynamics with pathological hyper-excitation ($P_{ee} = 548.066$). (a) The parameter Γ_e is varied and the stable fixed points (solid curves), unstable fixed points (dashed curves), and Hopf bifurcations (asterisks) in h_e for the uncontrolled dynamics ($a = 0$ in black) and linearly controlled dynamics ($a < 0$ in color) are shown. (b) The Hopf bifurcations (asterisks) and maxima and minima in h_e achieved during the stable (solid curves) and unstable (dotted curves) limit cycle oscillations as Γ_e is varied. We plot the uncontrolled dynamics in black and the controlled dynamics in color. Both subfigures use the following color scheme: black $a = 0.0$, red $a = -0.1$, orange $a = -0.5$, light green $a = -1.0$, dark green $a = -1.67$, blue $a = -1.86$, and purple $a = -1.96$. For (a), the curves progress from rightmost and least in h_e for $a = 0.0$, to leftmost and greatest in h_e for $a = -1.96$. For (b), the right Hopf bifurcation of each curve (i.e., the Hopf bifurcation of greater Γ_e) progress from the right of the figure for $a = 0.0$ to the left of the figure for $a = -1.86$.

show the bifurcation diagrams of (3.9) with (3.9a) replaced by (3.10) for six values of the gain a. To help visualize these results, we plot in Figure 3.24(a) only the stable and unstable fixed points as solid and dashed curves, respectively, and denote the Hopf bifurcations as asterisks. We plot the results for the uncontrolled dynamics in black, and the controlled dynamics in color. We note that the bifurcation diagram for the uncontrolled dynamics is also shown in Figure 3.12(a). The colors in Figure 3.24 correspond to the controller gain as follows: red $a = -0.1$, orange $a = -0.5$, light green $a = -1.0$, dark green $a = -1.67$, blue $a = -1.86$, and purple $a = -1.96$. We find that for small negative gains the two Hopf bifurcations originally separated by 0.28×10^{-3} in Γ_e, separate further; for $a = -1.0$ (the light green curve — fourth from the top) the separation between the Hopf bifurcations is 0.55×10^{-3}. As we reduce a toward -1.96, the Hopf bifurcations approach one another and coalesce. At $a = -1.96$ (the purple curve — the uppermost curve) no Hopf bifurcations occur and only stable fixed points remain.

To investigate the limit cycles born in the Hopf bifurcations, we plot in Figure 3.24(b) the maxima and minima of h_e achieved during the stable (solid curves) and unstable (dotted curves) limit cycles. We note that the solid curves in this figure correspond to the extrema of stable limit cycles, and not to stable fixed points. The color scheme is identical to that in Figure 3.24(a); the black and color curves correspond to the uncontrolled and controlled dynamics, respectively. We denote the Hopf bifurcations with asterisks; the values of the Hopf bifurcations are identical in Figures 3.24(a) and 3.24(b). We find that for $a = -0.1$ (the red curve — second from the right) both Hopf bifurcations are subcritical; the limit cycles born in both Hopf bifurcations are unstable. At $a = -0.5$ (the orange curve — third from the right), the left Hopf bifurcation at $\Gamma_e = 0.32 \times 10^{-3}$ is supercritical, and the right Hopf bifurcation at $\Gamma_e = 0.83 \times 10^{-3}$ remains subcritical. The stabilities of the limit cycles born in the two Hopf bifurcations are preserved for more negative gains. For $a = -1.86$ (the blue curve of smallest extent in h_e), the two Hopf bifurcations are close in both h_e and Γ_e, and the amplitudes of the limit cycles are small. Finally, for $a = -1.96$ we find that neither the subcritical nor supercritical Hopf bifurcations remain. The transition between the state with two Hopf bifurcations (as for $a = -1.86$) and no Hopf bifurcations (as for $a = -1.96$) can be quite involved (see, for example, Figure 4.6 of [98].) One might investigate the details of this transition by determining the normal form of the dynamics near the values of a and Γ_e at which the Hopf bifurcations approach (i.e., near $a = -1.864$ and $\Gamma_e = 0.273 \times 10^{-3}$.) Of course, this calculation would be quite involved for the system of ODEs stated in (3.1). Here we are not concerned with the bifurcations that eliminate the Hopf bifurcations. Instead, our goal is more practical and modest: the elimination of seizure-like oscillations from the dynamics.

We now consider how the left Hopf bifurcations shown in Figures 3.24(a) and 3.24(b) change from subcritical to supercritical. We plot in Figure 3.25 bifurcation diagrams for values of the gain a between -0.44 (the leftmost curve) and -0.40 (the rightmost curve.) For $a = -0.40$, the Hopf bifurcation is subcritical. The unstable limit cycle born in this Hopf bifurcation undergoes a saddle node bifurcation and stabilizes. We note that this saddle node bifurcation of

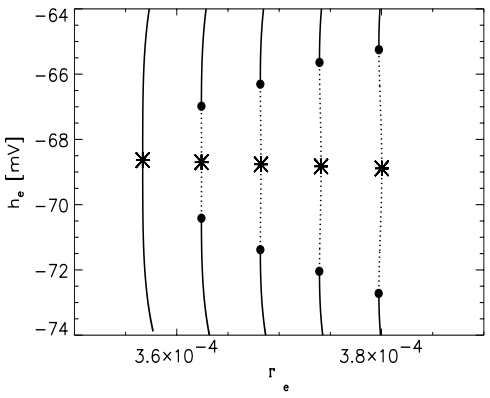

Figure 3.25: The bifurcation diagrams near the Bautin bifurcation for the hyper-excited ($P_{ee} = 548.066$) dynamics. For the five curves, we fix $a = -0.44$, -0.43, -0.42, -0.41, and -0.40, going from left to right in the figure. We show the Hopf bifurcations (asterisks) and maxima and minima achieved in the unstable (dotted curves) and stable (solid curves) limit cycles. We denote the saddle node bifurcations of limit cycles with filled circles. The Bautin bifurcation occurs near the leftmost curve ($a = -0.44$.)

limit cycles — or fold limit cycle bifurcation — occurs in the figure at the intersection of the dotted and solid curves (i.e., near -65 mV and -72.5 mV for $a = -0.40$.) We mark the saddle node bifurcations of limit cycles with filled circles. As we decrease the gain, the fold limit cycle bifurcation approaches the subcritical Hopf bifurcation. Near $a = -0.44$, the fold limit cycle bifurcation and subcritical Hopf bifurcation coalesce in a co-dimension two Bautin bifurcation. As a result, the controlled system (for values of the gain $-1.96 < a < -0.44$) is of the subHopf/Hopf bursting type [76].

Our goal in implementing the feedback controller is to eliminate large amplitude oscillations in $\tilde{h}_e$ (i.e., seizures) from the model dynamics. We have used the results shown in Figures 3.24(a) and 3.24(b) to suggest that the Hopf bifurcations approach and coalesce near $a = -1.96$. To further illustrate this result, we plot in Figure 3.26 the value of Γ_e for each Hopf bifurcation as a function of the gain a. At $a = 0$ we mark with asterisks the two Hopf bifurcations for the uncontrolled dynamics. As we decrease the gain a, the Hopf bifurcations initially separate in Γ_e. Near $a = -0.4$ a Bautin bifurcation occurs (denoted by a square) and one Hopf bifurcation (the lower one in this figure) becomes supercritical. We indicate the subcritical and supercritical Hopf bifurcations as dotted and solid curves, respectively. As we decrease a further past the Bautin bifurcation, the two Hopf bifurcations approach and at $a = -1.96$ neither Hopf bifurcation remains. Thus, for values of the gain $a \leq -1.96$, we expect no large amplitude, limit cycle dynamics.

To show how the controller effects the dynamics, we compute a numerical solution to (3.9) with (3.9a) replaced by (3.10). Here we use the same parameters ($P_{ee} = 548.066$ and $\Gamma_e = 0.8 \times 10^{-3}$) and algorithm (fourth-order Runge-Kutta with time step 0.4 ms) we used to create Figure 3.12(b). In that figure, we fixed $a = 0.0$. Here we set $a = -1.96$

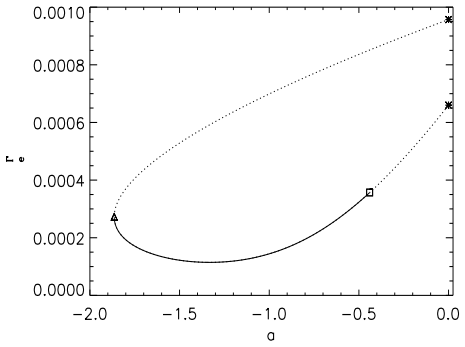

Figure 3.26: Two parameter continuation of the Hopf bifurcations for the hyper-excited ($P_{ee} = 548.066$) cortex. We plot the value of Γ_e for each Hopf bifurcation as a function of the gain a. We mark the two Hopf bifurcations from the uncontrolled dynamics ($a = 0.0$) with asterisks. The solid and dotted curves denote supercritical and subcritical Hopf bifurcations, respectively. In creating this figure, we compute the criticality for only a sample of Hopf bifurcations and deduce a change in criticality only at the Bautin bifurcation labeled with the square. We note that for $a \leq -1.96$ neither Hopf bifurcation remains; we label this point with a triangle. We do not indicate how the transition from two Hopf bifurcations to none occurs.

for 1 s $< t <$ 3 s, and $a = 0.0$ otherwise. We plot the results in Figure 3.27. Initially, in the uncontrolled state, h_e undergoes large amplitude oscillations. At $t = 1$ s, we turn on the controller and within 0.2 s the oscillations cease and h_e approaches a stable fixed point. When we turn off the controller at $t = 3$ s, oscillations in h_e immediately develop. We note that Gluckman *et al* find a similar seizure-after-release effect in their experimental work on rat hippocampal slices [92].

With the simple linear feedback controller, we cannot avoid the seizure-after-release phenomenon. Upon changing from the controlled (e.g., $a = -1.96$) to the uncontrolled ($a = 0.0$) dynamics, the bifurcation diagram reverts to that shown in Figure 3.12(a). Because we have kept the parameters $P_{ee} = 548.066$ and $\Gamma_e = 0.8 \times 10^{-3}$ fixed, h_e becomes entrained by the large amplitude, stable limit limit cycle shown in Figure 3.12(b). To eliminate the seizure-after-release phenomenon, we could change one of these parameters before returning to the uncontrolled state. For example, we could increase Γ_e from 0.8×10^{-3} to 1.3×10^{-3} while the controller was active. Then, upon disabling the controller, h_e would approach a stable fixed point instead of entering a stable limit cycle. We discuss this mechanism further in Section 3.7.4. In the next subsection, we set P_{ee} to the typical value of 11.0 and show how the controller effects the model dynamics.

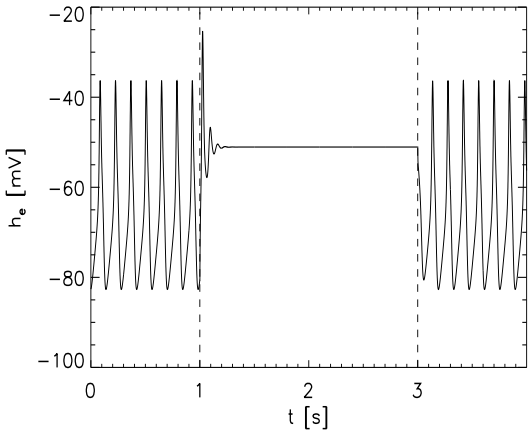

Figure 3.27: Numerical solution to the dimensionless ODEs with the applied linear controller. We set parameters to the pathological values $P_{ee} = 548.066$, $\Gamma_e = 0.80 \times 10^{-3}$, and the controller gain $a = -1.96$ for 1 s $< t <$ 3 s, and $a = 0.0$ otherwise. We plot dimensional h_e as a function of dimensional time t. At $t = 1$ s (indicated by the left vertical dashed line) the active controller rapidly terminates the oscillations in h_e. At $t = 3$ s (indicated by the right vertical dashed line) the controller becomes inactive and oscillations immediately develop.

The case of normal excitation: $P_{ee} = 11.0$

In the previous section we showed that the linear controller can eliminate oscillations in the (dimensional) model variable h_e. To induce these oscillations, we increased the parameter P_{ee} to nearly fifty times its normal value (i.e., we set $P_{ee} = 548.066$.) We now set P_{ee} to its typical value (i.e., $P_{ee} = 11.0$) and show how the controller effects the normal model dynamics. This case is of practical importance; should the controller incorrectly activate during normal brain activity, it must not induce a seizure.

To start, we fix $P_{ee} = 11.0$ and compute bifurcation diagrams of (3.9) with (3.9a) replaced by (3.10). In Figure 3.28(a) we plot the stable (solid curves) and unstable (dashed curves) fixed points and Hopf bifurcations (asterisks) for five values of the gain a. We denote the values of a as follows: black $a = 0.0$, red $a = -0.3$, orange $a = -1.0$, light-green $a = -1.96$, and purple $a = -2.2$. We note that the color scheme in Figures 3.24(a) and 3.28(a) are different. For $a = 0.0$, the black curve, we find only one Hopf bifurcation at $\Gamma_e = 1.21 \times 10^{-3}$. At $a = -0.3$ (the red curve,) a second Hopf bifurcation appears at $\Gamma_e = 2.07 \times 10^{-3}$. As we decrease the gain a to -1.0 and -1.96, we find that the two Hopf bifurcations approach in Γ_e and neither Hopf bifurcation remains at $a = -2.2$.

The Hopf bifurcations shown in Figure 3.28(a) affect the dynamics differently. To illustrate these effects, we plot in Figure 3.28(b) the maxima and minima achieved by h_e during stable (solid curves) and unstable (dotted curves) limit cycles. For $a = 0.0$ (the black asterisk without limit cycles,) the Hopf bifurcation is supercritical. The unstable

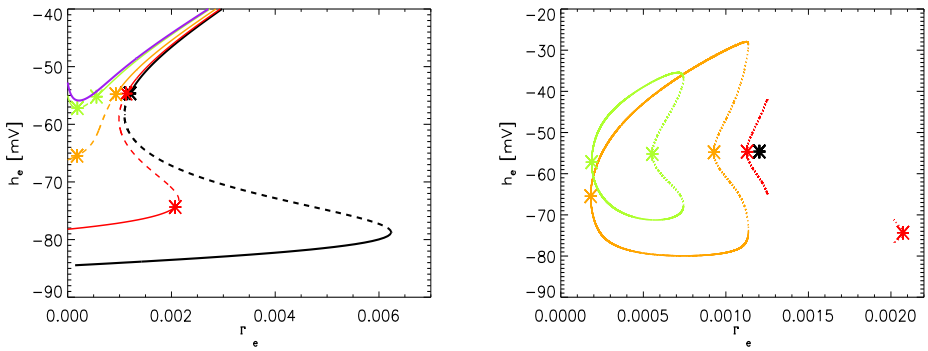

(a) (b)

Figure 3.28: Bifurcation diagrams for the uncontrolled and controlled typical ($P_{ee} = 11.0$) dynamics. (a) The parameter Γ_e is varied and the stable fixed points (solid lines), unstable fixed points (dashed lines), and Hopf bifurcations (asterisks) in h_e for the uncontrolled dynamics ($a = 0$ in black) and linearly controlled dynamics ($a < 0$ in color) are shown. (b) The Hopf bifurcations (asterisks) and maxima and minima in h_e achieved during the stable (solid curves) and unstable (dotted curves) limit cycle oscillations as Γ_e is varied. We plot the uncontrolled dynamics in black and the controlled dynamics in color. Both subfigures use the following color scheme: black $a = 0.0$, red $a = -0.3$, orange $a = -1.0$, light-green $a = -1.96$, and purple $a = -2.2$. For (a), the curves progress from rightmost and least in h_e for $a = 0.0$, to leftmost and greatest in h_e for $a = -2.2$. For (b): the Hopf bifurcation without a limit cycle denotes the $a = 0.0$ case, the two subcritical Hopf bifurcations without a saddle node bifurcation of limit cycles denotes that $a = -0.3$ case, the subcritical and supercritical Hopf bifurcations connected by saddle node bifurcation of limit cycles of large amplitude denotes that $a = -1.0$ case, and the subcritical and supercritical Hopf bifurcations connected by saddle node bifurcation of limit cycles of smaller amplitude denotes that $a = -1.96$ case.

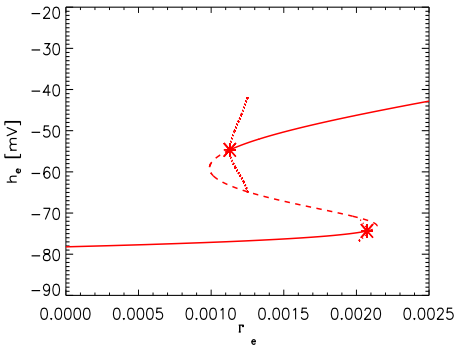

Figure 3.29: Bifurcation diagram for the controlled dimensionless ODEs at $P_{ee} = 11.0$ and gain $a = -0.3$. The parameter Γ_e is varied and the stable (solid curve) and unstable (dashed curve) fixed points in h_e are shown. The asterisks denote the two Hopf bifurcations. The dotted curves denote the maximum and minimum values of h_e achieved during the unstable limit cycles. Both unstable limit cycles intersect the curve of unstable fixed points and terminate in a global bifurcation. The bifurcation diagram in this figure corresponds to red curves shown in Figures 3.28(a) and 3.28(b).

limit cycle born in this Hopf bifurcation increases in amplitude, and immediately crosses the branch of unstable fixed points in h_e. This transition is so abrupt that we cannot show the unstable limit cycle branch in Figure 3.28(b). We illustrated the dynamics near this Hopf bifurcationin Figure 3.11(c). In that figure, we plotted a numerical solution to (3.9) with $\Gamma_e = 1.21 \times 10^{-3}$, near the Hopf bifurcation and no stochastic input. We found that oscillations in h_e increased in amplitude until h_e reached a threshold value. Upon reaching this threshold, the oscillations in h_e ceased and the dynamics approached a stable fixed point. These low amplitude, transient oscillations do not mimic the large amplitude, persistent oscillations we observe in ECoG data recorded during seizure. Thus we do not require that the controller eliminate this low amplitude, oscillatory behavior and its subsequent transition to a stable fixed point.

With this understanding of the uncontrolled ($a = 0.0$) dynamics, we now consider the controlled behavior. For $a = -0.3$ (the red curves plotted in Figures 3.28(a) — second from the bottom — and 3.28(b)), we find two Hopf bifurcations, one at $\Gamma_e = 1.13 \times 10^{-3}$ — near the Hopf bifurcation found for the $a = 0.0$ case — and the other at $\Gamma_e = 2.07 \times 10^{-3}$. Both Hopf bifurcations are subcritical and produce unstable limit cycles. The limit cycles increase in amplitude and intersect the curve of unstable fixed points. To illustrate this behavior, we show in Figure 3.29 the complete bifurcation diagram for gain $a = -0.3$. We note that the (red) curves in this figure correspond to the (red) curves shown in Figures 3.28(a) and 3.28(b). The Hopf bifurcations give rise to unstable limit cycles. The amplitudes and periods of the oscillations (dotted curves) increase until the limit cycles reach the branch of unstable fixed points (dashed curves) near $\Gamma_e = 1.25 \times 10^{-3}$ and $\Gamma_e = 2.02 \times 10^{-3}$. At these intersections the oscillations in h_e cease in a global bifurcation and h_e approaches a stable fixed point, similar to the results found for the $a = 0.0$ case and shown in

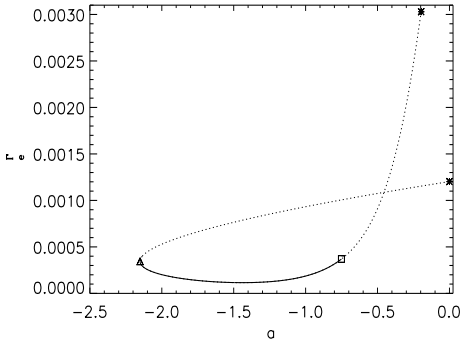

Figure 3.30: Two parameter continuation of the Hopf bifurcations for the cortex with typical excitation ($P_{ee} = 11.0$.) We plot the value of Γ_e for each Hopf bifurcation as a function of the gain a. We mark with asterisks the Hopf bifurcation present in the uncontrolled dynamics ($a = 0.0$) and a Hopf bifurcation that appears at $a = -0.2$. The solid and dotted curves denote supercritical and subcritical Hopf bifurcations, respectively. We label the the Bautin bifurcation with a square. We note that for $a \leq -2.15$ neither Hopf bifurcation remains; we label this point with a triangle. We do not indicate how the transition from two Hopf bifurcations to none occurs.

Figure 3.12(a). Thus, for small negative gains, the controlled dynamics enter unstable, low amplitude limit cycles, not the high amplitude stable limit cycles characteristic of a seizure. As we decrease a further we find, but do not show, that the Hopf bifurcation with a lower value of h_e undergoes a Bautin bifurcation near $a = -0.75$. The stable limit cycles born in the supercritical Hopf bifurcations undergo a saddle node bifurcation of limit cycles with the unstable limit cycles born in the subcritical Hopf bifurcation. We illustrate this limit cycle behavior in Figure 3.28(b) for $a = -1.0$ (orange curve — large amplitude, stable oscillation) and $a = -1.96$ (light-green curve — moderate amplitude, stable oscillations). We note that with gain $a = -1.96$ the controller successfully terminates seizures in the hyper-excited ($P_{ee} = 548.066$) model cortex as we show in Figure 3.27. Unfortunately, the same controller and gain induces large amplitude stable oscillations in h_e characteristic of seizures for $P_{ee} = 11.0$, the typical value of subcortical excitation.

To summarize how the Hopf bifurcations depend on the gain a and parameter Γ_e for $P_{ee} = 11.0$ (the typical value), we plot in Figure 3.30 the value of Γ_e for each Hopf bifurcation as a function of the gain a. We create this figure and Figure 3.26 in a similar way. Namely, we determine whether the Hopf bifurcations are subcritical (dotted curves) or supercritical (solid curve) by computing the limit cycle stability at a sample of points. At $a = 0.0$, we find only one Hopf bifurcation at $\Gamma_e = 1.21 \times 10^{-3}$ marked with an asterisk. Decreasing a, we find a second Hopf bifurcation at $a = -0.2$. This Hopf bifurcation undergoes a Bautin bifurcation (marked by a square) at $a = -0.75$ and the limit cycle stabilizes. The supercritical and subcritical Hopf bifurcations approach and coalesce at $a = -2.15$. We note that the apparent crossing of the subcritical Hopf bifurcations at $a = -0.45$ results from projecting the dynamics onto this two-dimensional space.

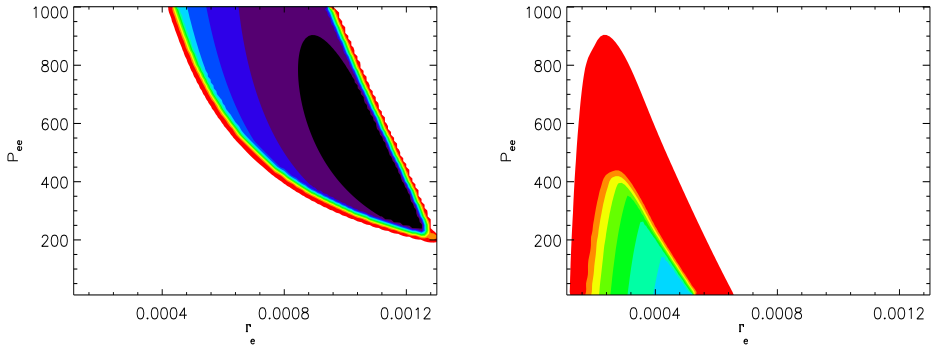

(a) (b)

Figure 3.31: The difference between the maximum and minimum achieved by (the dimensional) h_e in solutions of the dimensionless ODEs for parameters P_{ee} and Γ_e. The difference is plotted in a linear color (grey) scale with white representing a 0 mV difference and purple (black) representing a 50 mV difference. (a) Gain $a = 0.0$, the uncontrolled system. The dark region corresponds to stable, seizure-like oscillations in h_e and broadens as P_{ee} is increased. (b) Gain $a = -1.96$. Stable, seizure-like oscillations in h_e occur for $P_{ee} \approx 11.0$ (the typical value of P_{ee}) but at lower than the typical value of Γ_e.

We have shown that with gain $a = -1.96$, the controller eliminates seizures from the hyper-excited ($P_{ee} = 548.066$) model cortex. Unfortunately, the same controller induces seizures in the model cortex with typical excitation ($P_{ee} = 11.0$.) We do not consider such a controller successful. Should the controller activate during near-normal activity — requiring a 40% decrease in the typical value of Γ_e — the controller may induce a seizure. To avoid this unwanted behavior, we set the gain $a = -2.4$. At this gain, we do not find any Hopf bifurcations in the hyper-excited or typical dynamics; see Figures 3.26 and 3.30. To verify this result, we compute numerical solutions to the dimensionless ODEs for $11.0 < P_{ee} < 1000.0$, $0.11 \times 10^{-3} < \Gamma_e < 1.4 \times 10^{-3}$, and $a = 0.0$, $a = -1.96$, and $a = -2.2$. We use the fourth-order Runge-Kutta method with a (dimensional) time step of 0.4 ms. We then determine the difference between the maximum and minimum achieved by the solution h_e after transient behavior has decayed. If h_e approaches a fixed point, then the maximum and minimum are nearly equal and their difference approaches zero. But, if h_e is entrained by a limit cycle then the difference between the maximum and minimum achieved by h_e is nonzero. In Figure 3.31(a) we fix $a = 0.0$ and plot the difference between the maximum and minimum achieved by h_e as a function of the parameters P_{ee} and Γ_e. Here white represents a 0 mV difference and purple (or black) a 50 mV difference. We find that oscillations in h_e (represented by the color (or dark) regions in Figure 3.31(a)) extend over a broad range of parameter values beginning near $P_{ee} = 250.0$ and $\Gamma_e = 1.3 \times 10^{-3}$. These regions of oscillatory activity in h_e illustrate the parameter values at which the dimensionless ODEs "seize." We note that Figure 3.31(a) is identical to Figure

3.15(a) except in color. We reproduce the figure here for comparison with Figure 3.31(b) in which we show the results of a similar computation with the gain $a = -1.96$. The color scheme is identical to that in Figure 3.31(a). We note that oscillations develop at smaller values of P_{ee} and Γ_e. We find, but do not show, that *no* seizure-like oscillations occur when we fix the gain $a = -2.4$. Thus we conclude that the linear feedback controller with gain $a = -2.4$ eliminates seizures in the hyper-excited ($P_{ee} \gg 11.0$) model cortex and does not induce seizures in the model cortex with typical excitation ($P_{ee} \approx 11.0$).

3.7.2 Differential controller

We have shown in Section 3.7.1 how we can use a feedback controller linear in h_e to halt seizures in the model cortex. Although successful in the model, the linear controller would fail in practice. To prevent tissue damage a controller should inject charge balanced currents (e.g., biphasic pulses [99]) into the cortex. The linear controller we discuss in Section 3.7.1 violates this important restriction. Instead, with $a = -1.96$, say, the active controller establishes a constant voltage across the cortical tissue. We show an example of this in Figure 3.27. For 1 s $< t <$ 3 s, the controller maintains h_e at -51 mV and therefore establishes a constant voltage of $a\tilde{h}_e = (-1.96) \times (-51$ mV $) = 100$ mV across the cortical tissue. This constant voltage requires a constant — not a charged balanced — continuous, current. In practice, the constant current produced by the linear controller would create unacceptable damage to cortical tissue [99].

To implement a controller that avoids damaging cortical tissue, we consider a differential controller. In [94], the authors apply a differential controller to a population of neurons interacting through global coupling. They find that, once initiated, the controller rapidly suppresses synchronous activity and decays to the noise level. We note that in Figure 3 of [94] the controller value appears to oscillate around zero and is suggestive of a charge balanced intervention.

To apply a differential controller to (3.9), we set (3.9a) to:

$$\frac{\partial \tilde{h}_e[t]}{\partial \tilde{t}} = 1 - \tilde{h}_e[t] + \Gamma_e\big(h_e^0 - \tilde{h}_e[t]\big)\tilde{I}_{ee}[t] + \Gamma_i\big(h_i^0 - \tilde{h}_e[t]\big)\tilde{I}_{ie}[t] + b(\tilde{h}_e[t] - \tilde{h}_e[t-\tau]). \tag{3.11}$$

Here we explicitly state the time dependence in square brackets following each variable. The last term on the right hand side of (3.11) represents the controller; b denotes the controller gain, and τ the delay time. By introducing the differential controller, we change the system of ODEs in (3.9) into a system of delay differential equations (DDEs.) One may compute bifurcation diagrams for the DDEs (see, for example [100]) but we will not do so here. Instead we compute numerical solutions and response diagrams to the DDEs and show how the differential controller affects the

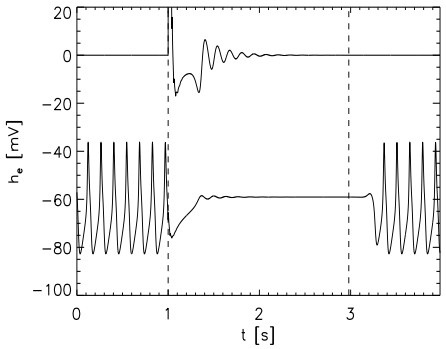

Figure 3.32: Numerical solution to the dimensionless DDEs with the applied differential controller. We set parameters to the pathological values $P_{ee} = 548.066$, $\Gamma_e = 0.80 \times 10^{-3}$, and the controller gain $b = -10.0$ for 1 s $< t <$ 3 s, and $b = 0.0$ otherwise. We plot the model results for dimensional h_e as a function of dimensional time t in the lower curve. We plot the dimensional value of the differential controller in the upper curve. At $t = 1$ s (indicated by the left vertical dashed line) the active controller rapidly terminates the oscillations in h_e. At $t = 3$ s (indicated by the right vertical dashed line) the controller becomes inactive and oscillations soon return.

dynamics. We will show that the differential controller can stop the model dynamics from seizing with minimal net intervention.

We start by computing a numerical solution to (3.9) with (3.9a) replaced by (3.11). We fix the model parameters to the typical values except for P_{ee} and Γ_e which we set to the pathological values: $P_{ee} = 548.066$ and $\Gamma_e = 0.80 \times 10^{-3}$. We fix the delay time of the controller $\tau = 20$ ms and vary the gain b as follows: for 1 s $< t <$ 3 s we set $b = -10.0$; otherwise $b = 0.0$. We compute the numerical solution using a fourth order Runge-Kutta method with time step of 0.4 ms and show the results in Figure 3.32. We plot in the lower curve the model results for the dimensional h_e, and in the upper curve the value of the controller (i.e., the last term on the right hand side of (3.11).) For $t < 1$ s, the controller is inactive and the model "seizes." At $t = 1$ s we activate the differential controller and its voltage quickly increases to a maximum value of 190 mV (outside of the range shown in this figure.) The controller halts the seizure and, within one second, h_e approaches a fixed point. Soon afterward, the applied voltage delivered by the controller approaches zero, but continues to act weakly on the dynamics. Upon deactivating the controller at $t = 3$ s, h_e drifts from the steady value and becomes entrained in the limit cycle behavior characteristic of the seizure-after-release effect.

We have shown in Figure 3.32 that the differential controller with gain $b = -10.0$ can halt seizures in the model cortex. We now consider response diagrams for the controlled dynamics with different values of the gain b. To compute each response diagram, we fix the parameters at the typical values except for $P_{ee} = 548.066$ (the pathological value) and Γ_e chosen from the range $0.3 \times 10^{-3} < \Gamma_e < 1.3 \times 10^{-3}$. For each value of Γ_e we solve the dimensionless DDEs using a fourth order Runge-Kutta method with time step of 0.4 ms and total time of 1600 ms. We then compute

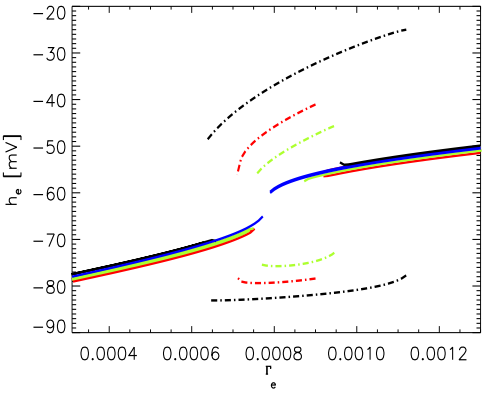

Figure 3.33: Response diagrams for the uncontrolled and differential controlled dynamics with pathological hyper-excitation ($P_{ee} = 548.066$). The parameter Γ_e is varied and the stable fixed points (solid curves) and stable limit cycles (dot-dash curves) are shown. We plot the uncontrolled dynamics in black and the controlled dynamics in color where: red $b = -2.5$, light green $b = -5.0$, and blue $b = -10.0$. The amplitudes of oscillation are largest for $b = 0.0$ and decrease for $b = -2.5$ and $b = -5.0$. We find no oscillation for $b = -10.0$. The curves of fixed points nearly overlap.

the maximum and minimum achieved by h_e during the last 400 ms of the solution. If the dynamics approach a fixed point, then the maximum and minimum of h_e are equal. Otherwise, (e.g., if the dynamics enter a limit cycle) then the maximum and minimum are unequal. We repeat this computation for different values Γ_e that deviate from the current value by 0.01×10^{-3}. We note that the response diagram is similar to the bifurcation diagrams shown in Section 3.7.1. An important difference is that, in the response diagrams, we can only show stable (not unstable) fixed points and limit cycles.

We show the response diagrams in Figure 3.33. We plot in black the response diagram for the uncontrolled ($b = 0.0$) dynamics. Where the maximum and minimum of h_e are equal, we plot black solid curves; otherwise we plot dot-dash curves. Here we find two curves of stable fixed points (the black, solid curves) and two curves of stable oscillations (the black, dot-dash curves largest and smallest in h_e.) The stable oscillations occur for $0.65 \times 10^{-3} < \Gamma_e < 1.1 \times 10^{-3}$. We note the similarity between the black curves shown in this response diagram and the stable fixed points and limit cycles shown in Figure 3.12(a). As we decrease the gain b to -2.5 (the red curves) and -5.0 (the light green curves) we find that the stable oscillations — represented by the dot-dash lines — decrease in amplitude, and that the branches of stable fixed points extend over more of Γ_e. In the figure we have vertically offset the curves of stable fixed points to allow visual comparison; these curves are nearly identical in h_e throughout the regions of overlap in Γ_e. At $b = -10.0$ (the blue curves) we find no stable oscillations in the dynamics; we only find two curves of stable fixed points. We conclude that the differential controller with delay time $\tau = 20$ ms and gain $b = -10.0$ can prevent seizure-like oscillations in the model cortex with pathological hyper-excitation ($P_{ee} = 548.066$).

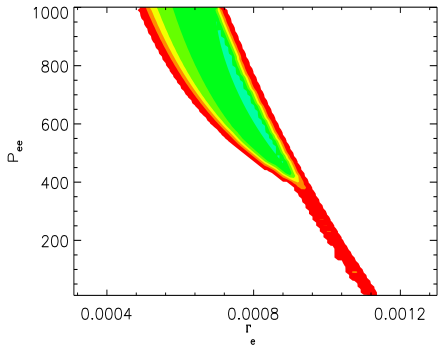

Figure 3.34: The difference between the maximum and minimum achieved by (the dimensional) h_e in solutions of the dimensionless DDEs for parameters P_{ee} and Γ_e. For the differential controller the delay time $\tau = 20$ ms and gain $b = -5.0$. The difference is plotted in a linear color (gray) scale with white representing a 0 mV difference and purple (black) representing a 50 mV difference. The stable "seizure" oscillations of h_e broaden as P_{ee} is increased.

To show that the differential controller is robust to changes in the model parameters P_{ee} and Γ_e, we compute two numerical solutions to the dimensionless DDEs over the parameters $11.0 < P_{ee} < 1000.0$ and $0.11 \times 10^{-3} < \Gamma_e < 1.4 \times 10^{-3}$. In the first solution, we fix the delay time of the differential controller $\tau = 20$ ms and the gain $b = -5.0$. We then follow the same procedure and implement the same color scale as we used to create Figures 3.31(a) and 3.31(b). We have shown the uncontrolled dynamics ($b = 0.0$) in Figure 3.31(a), and found that oscillatory activity (denoted by the color (or dark) regions) extends over a wide range of parameter space. In Figure 3.34 we show the results for the controlled dynamics with gain $b = -5.0$. We find that oscillations remain over the same region of parameter space, although with lower amplitude. For $b = -10.0$, we find no oscillations in h_e for any values of P_{ee} and Γ_e.

We have shown that the differential controller, like the linear controller, can halt seizures in the model cortex over a wide range of parameter values. The differential controller provides two important improvements to the linear controller. First, the applied voltage delivered by the differential controller quickly approaches zero. After h_e achieves the stable value (near -60 mV in Figure 3.32) the controller may remain active with only minimal effect on the tissue. Second, the applied voltage delivered by the differential controller fluctuates around zero. For the results shown in Figure 3.32, the net voltage applied by the controller is 14 mV. This voltage is much smaller — and much less damaging to cortical tissue — than that delivered by the linear controller. Here we have only considered a cursory exploration of the differential controller parameters (delay time τ and gain b.) A more detailed analysis may reveal a set of optimal parameters that further improve the differential controller over the linear controller.

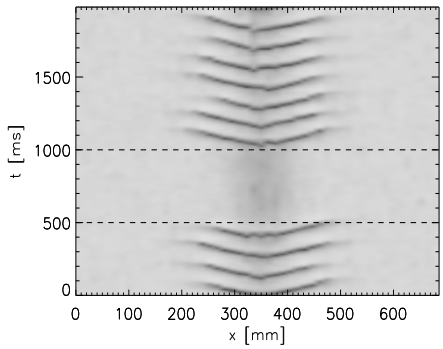

Figure 3.35: Numerical solution to the controlled dimensionless SPDEs with parameters: $\Gamma_e = 0.87 \times 10^{-3}$, $\alpha = 0.001$, and P_{ee} and b both Gaussian functions in space, each with an extremum at $x = 350$ mm and a full width at half the extremum of 46 mm. The boundary conditions are in periodic in space. Space (in mm) and time (in ms) are plotted along the horizontal and vertical axes, respectively. The value of h_e is plotted in linear greyscale with $h_e = -100$ mV in white and $h_e = 0.0$ mV in black. For $t < 500$ ms, waves in h_e travel outward from the region of hyper-excitation near $x = 350$ mm. At $t = 500$ ms (indicated by a horizontal dashed line,) we activate the differential controller — we set the minimum of the gain $b_0 = -10.0$ and $\tau = 20$ ms. The traveling waves in h_e cease until we deactivate the controller at $t = 1000$ ms (indicated by a horizontal dashed line.)

3.7.3 Control of stochastic partial differential equations

We have shown in Sections 3.7.1 - 3.7.2 how two different controllers can terminate seizure-like oscillations of the model equations (3.9). We chose this system of ODEs as a simplification of the complete mathematical model (3.1). In this section we include the spatial dependence and stochastic input of the model and apply the differential controller (described in Section 3.7.2) to the complete system of SPDEs.

To compute a numerical solution to (3.1) we fix all of the parameters at the typical values except for Γ_e and P_{ee}. We set $\Gamma_e = 0.8 \times 10^{-3}$ uniform in space, and P_{ee} Gaussian in space with a maximum of 548.066 at $x = 350$ mm, a full width at half maximum of 46 mm, and a minimum of 11.0. We choose this Gaussian profile for P_{ee} to construct a region of hyper-excitation localized in space; we think of this region as the epileptogenic zone in the model. We apply the differential controller to (3.1a) and set the controller delay time to $\tau = 20$ ms and the gain b to be Gaussian in space with a minimum b_0 at $x = 350$ mm, a full width at half minimum of 46 mm, and a maximum of $b = 0.0$. We vary the minimum of the gain b_0 as follows: $b_0 = -10.0$ for 500 ms $< t <$ 1000 ms, and $b_0 = 0.0$ otherwise. We note that the controller is only active for 500 ms $< t <$ 1000 ms. We compute numerical solutions to (3.1) using the Euler-Maruyama algorithm with fixed steps in space and time, 14 mm and 0.1 ms, respectively, and boundary conditions periodic in space [78].

We show the results in Figure 3.35. We plot the (dimensional) value of h_e in linear gray scale, with white

representing -100 mV and black representing 0.0 mV, as a function of (dimensional) space and time. For $t < 500$ ms, we find that waves — represented by the dark ridges — emanate from the region of hyper-excitation at $x = 350$ mm. These waves travel outward to less excited ($P_{ee} \approx 11.0$) spatial regions and there decay. We showed in Section 3.6 that the speed and temporal frequency of these waves agree with observed ECoG data recorded from four human subjects during seizure. At $t = 500$ ms, we activate the controller. Almost immediately, the traveling wave solutions cease and h_e fluctuates around a stable value at each point in space. During the time interval of active control, the mean and standard deviation of h_e at $x = 350$ mm are -70 mV and 2 mV, respectively. At $t = 1000$ ms, we deactivate the controller and the traveling waves solutions reappear.

We conclude that the differential controller can abort seizures in the complete system of SPDEs (3.1). Here we only consider one instance of the dimensionless SPDEs, with P_{ee} and b both Gaussian in space. We find that the controller halts the traveling waves in h_e characteristic of a seizure. Like the controlled dimensionless ODEs, the controlled dimensionless SPDEs exhibit the seizure-after-release effect. Upon deactivation of the controller at $t = 1000$ ms, the traveling wave solutions develop. To avoid this effect, we suggest that a more effective controller would manipulate an additional model parameter (e.g., increase Γ_e or decrease P_{ee}) before returning to the uncontrolled $b = 0.0$ state.

3.7.4 Discussion

In this section we explored two methods for controlling the large amplitude, stable "seizure" oscillations in h_e. In Section 3.7.1 we applied a linear feedback controller to the model. We showed that with a gain of $a = -2.4$ the controller prevented seizures in the hyper-excited cortex ($P_{ee} \gg 11.0$) and did not induce seizures in the typical cortex ($P_{ee} \approx 11.0$.) Unfortunately, the linear controller fails in one important aspect of practical importance: the linear controller establishes a large net voltage across the cortex. To correct for this, we applied a differential controller to the model in Section 3.7.2. We showed that the differential controller can also halt seizures in the hyper-excited cortex and establishes only a small net voltage across the cortex. Finally, in Section 3.5 we applied the differential controller to an example of the SPDEs. We showed that the controller can abort the traveling waves of excitation characteristic of seizures in the complete model.

In our discussions of Figures 3.27 and 3.32 we noted that upon cessation of the linear and differential controllers seizures soon develop. Therefore, the controller must continually act on the system to prevent the seizure from occurring. Such a controller would require a large power source. Moreover, prolonged voltage control, even at low voltages, may damage the cortex [99]. To prevent (not just temporarily halt) a seizure, the controller must affect another model parameter. We showed in Section 3.3 that seizures occur in the model after a change in two parameters: P_{ee} and Γ_e.

A successful strategy employing linear feedback control would allow the controller to also effect Γ_e. To prevent a seizure, this new controller would first activate the voltage feedback controller and then slowly decrease Γ_e until the dynamics reach a safe range outside of the subHopf/fold cycle bifurcation. This controller operating on h_e and Γ_e would avoid the seizure-after-release effect.

These results lead us to propose an implantable seizure control device acting via two mechanisms. Immediately after seizure initiation, a voltage controller activates and temporarily halts the seizure. A chemical controller then activates and injects a drug either systemically or locally, into the brain. After the drugs take effect — perhaps a few minutes later — the voltage controller may be shut off without inducing a seizure. We suggest that the effect of the voltage controller is an immediate arrest of the seizure, while the effect of the second, chemical controller is prevention of seizure-after-release.

Using the model as a guide, we may propose the type of drugs to be injected by the chemical controller. For example, benzodiazepines (BZ) act to enhance the action of GABA at $GABA_A$ receptors (see Section 4.4 of [58] and note the change of notation.) In the model system, BZ may effect the *dimensionless* parameter Γ_e through the *dimensional* parameter G_i — the mean peak amplitude of the postsynaptic potential induced by a single presynaptic spike from an inhibitory neuron at the synapses of a cortical neuron; see Table 3.4 and Table 1 of [61]. An improved understanding of how drugs (such as BZ) relate to the model parameters may reveal how drugs affect the brain and allow the development of new therapies.

We have not considered several important practical issues in developing BES methods. First, to apply responsive cortical BES one must detect a seizure. An optimal seizure detection algorithm is an important and unresolved research topic [101, 102]. Second, the dimensionless ODEs are not an exact model of human cortical electrical activity. Finding an adequate controller for the model is, of course, not enough to justify clinical experiments. By changing the model parameters, one may develop a mesoscale model for electrical activity in, say, rat cortex where model results may be more readily tested. Finally, we have not considered whether the electrical stimulation induced by the two controllers will damage cortical tissue. To do so approximately, we assume: a uniform cortical conductivity of 0.15 S/m [103], a cortical thickness of 5 mm, an applied voltage of 100 mV, and a pulse duration — here, half the oscillation period — of 0.1 s. Using these assumptions, we calculate an estimate of the charge per phase injected by the controller of $7.5\,\mu$C. If we further assume that the area of the stimulation electrode is 1 cm^2 (large enough to cover a broad epileptogenic zone,) then the charge density — defined as the charge per phase divided by the electrode surface area — is $7.5\,\mu$C / cm^2. This combination of charge per phase and charge density satisfies stimulation induced safety limits (see Figure 9.1 of [99] and [104].) To confirm this result a more detailed analysis, perhaps involving multiple stimulation electrodes and a model of the human brain, is required [105].

Many exciting prospects exist for future epilepsy treatments. As seizure detection and localization algorithms improve, therapies may become more localized in both space and time. Similarly, as brain models improve, more effective and robust therapies may be developed. In time, mathematical models may aid in developing an implanted microprocessor that would detect cortical seizures and deliver electrical impulses and drug therapies to specific brain regions. In the next section, we describe other parameter changes that both induce and prevent seizure-like oscillations in the mathematical model.

3.8 Additional routes to seizure

In Section 3.6 we compared f_0 and v determined from observed data in Section 3.2 and simulated data in Sections 3.3-3.5. We found that, in general, the results for f_0 and v agree. Having validated the mathematical model in this way, we now consider other parameter changes that result in seizure-like oscillations in the model dynamics. To do so, we follow the procedure in Section 3.4 and compute numerical solutions to a simplified model: the dimensionless ODEs. In Section 3.4 we computed numerical solutions to the dimensionless ODEs and showed that seizures result from changes in two model parameters: an increase in P_{ee} and a decrease in Γ_e. We considered changes in these two parameters because both affect the excitation of the model cortex. In what follows, we now consider whether other parameter changes can result in seizure-like oscillations in h_e. To do so, we keep P_{ee} increased to nearly 50 times its typical value ($P_{ee} = 548.066$.) Therefore, the excitatory cell populations still receive strong, subcortical excitatory input; we call this model cortex "hyper-excited." We then vary those parameters affecting connectivity between cell populations (i.e, within and between the excitatory and inhibitory populations.) To examine all types of connectivity, we relax several assumptions made in Sections 3.3 and 3.5. In those sections, we assumed that connections between neuronal populations were independent of the postsynaptic population. For example, in Section 3.4, we defined the parameter Γ_e as the influence of excitatory input on both excitatory and inhibitory postsynaptic cell populations. A change in Γ_e, therefore, affected excitatory and inhibitory populations equally. To allow more general connectivity changes, we replace Γ_e with two parameters: Γ_{ee} and Γ_{ei}. The new parameter Γ_{ee} defines the influence of excitatory input on postsynaptic excitatory populations, and the new parameter Γ_{ei} defines the influence of excitatory input on postsynaptic inhibitory populations. We perform similar changes to three other model parameters (Γ_i, N_e^β, and N_i^β) that effect connectivity between neuronal populations. We define the eight new parameters and list the typical values in the second and fifth columns of Table 3.7, respectively.

Having established the validity of the model and defined the eight new parameters, we now determine which parameter changes result in seizure-like oscillations in the dynamics. To do so, we fix seven of the new parameters at

the typical values, change one parameter by a small amount, and compute a numerical solution to the dimensionless ODEs. We compute the numerical solutions here, and in what follows, using a fourth-order Runge-Kutta method with time step of 0.4 ms. We find that the variable h_e — the dimensional observable variable we compare to the ECoG data — either approaches a steady state value, or undergoes large amplitude oscillations. If h_e approaches a steady state value, we change the same parameter by a small amount and compute another numerical solution to the dimensionless ODEs. We continue this procedure until the parameter becomes implausible (e.g., negative) or h_e undergoes oscillations. If a small change in the parameter results in oscillations in h_e, then we say that this parameter induces a seizure in the model. In the last column of Table 3.7, we list the percentage change in each parameter necessary to induce seizure-like oscillations in h_e.

We illustrate the results of this analysis in Figure 3.36. In this figure, we show a schematic of the mathematical model similar to Figure 3.10. The eight rectangular boxes represent the 8 model (dimensionless) variables ($\tilde{h}_e$, $\tilde{h}_i$, $\tilde{I}_{ee}$, $\tilde{I}_{ei}$, $\tilde{I}_{ie}$, $\tilde{I}_{ii}$, $\tilde{\phi}_e$, and $\tilde{\phi}_i$) we define in Table 3.3. We again note that the dimensional variable h_e is related to the dimensionless variable $\tilde{h}_e$ by a simple scaling: $h_e = -70 \text{ mV} \times \tilde{h}_e$. The arrows represent connections between the variables, and between the variables and subcortical inputs (P_{ee}, P_{ei}, P_{ie}, and P_{ii} at the bottom of the figure.) Because we have increased P_{ee} by nearly 500%, we color its connection to $\tilde{I}_{ee}$ in gold. To make the model "seize" we change the parameters listed in the second column of Table 3.7 one at a time. We label the connections affected by each of these parameters in the figure. For example, to alter the strength of connection from $\tilde{h}_e$ to $\tilde{I}_{ee}$ we change the parameter N_{ee}^{β}. We find that seizure-like oscillations result in $\tilde{h}_e$ (or h_e) when we decrease N_{ee}^{β} by 28%. We indicate that a decrease in N_{ee}^{β} results in a seizure by coloring this connection and label green. We find that the model dynamics "seize" as we increase or decrease each of the eight parameters. We indicate the direction of change in Figure 3.36; we find that seizure-like oscillations results in h_e when we increase the strength of the connections colored in red or decrease the strength of the connections colored in green. We note that seizures result in the model from an increased connectivity between the two cell populations (i.e., between the excitatory and inhibitory populations,) and a decreased connectivity within each population (i.e., within the excitatory population or within the inhibitory population.)

So far we have discussed how to make the model "seize" by changing the *dimensionless* parameters listed in the second column of Table 3.7. We now discuss the relationship between these parameter changes in the model and physiological changes in the cortex. To do so, we first define each dimensionless parameter in terms of the *dimensional* quantities listed in Table 3.4. We list these definitions in the third column of Table 3.7. We note that the four parameters N_{ee}^{β}, N_{ei}^{β}, N_{ie}^{β}, and N_{ii}^{β} have no dimensional counterparts; each of these parameters represents a true dimensionless quantity: the mean number of synapses.

The dimensional definitions of Γ_{ee}, Γ_{ei}, Γ_{ie}, and Γ_{ii} are more complicated. Each contains four new quantities: G_{jk},

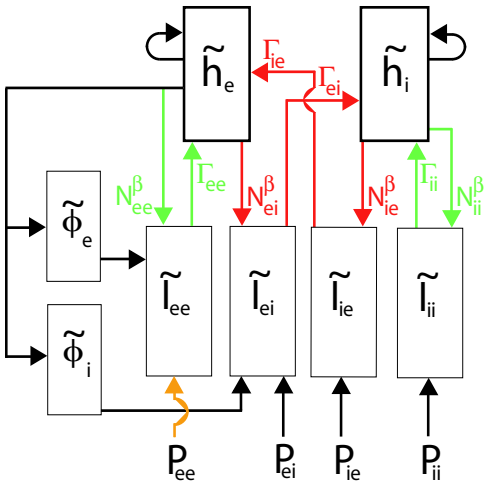

Figure 3.36: A schematic representation of the connections between the 8 (dimensionless) variables ($\tilde{h}_e$, $\tilde{h}_i$, $\tilde{I}_{ee}$, $\tilde{I}_{ei}$, $\tilde{I}_{ie}$, $\tilde{I}_{ii}$, $\tilde{\phi}_e$, and $\tilde{\phi}_i$) and the 4 subcortical inputs (P_{ee}, P_{ei}, P_{ie}, P_{ii}) in the model. We indicate the interactions between the variables using arrows and label the eight connections that affect the connectivity within and between the excitatory and inhibitory cell populations. We have increased P_{ee} by 500%; we denote this increase with the gold arrow. To induce seizures in the hyper-excited model dynamics, we may increase the strength of any single one of the red connections or decrease the strength of any single one of the green connections by the amounts shown in Table 3.7.

γ_{jk}, h_{jk}^{rev}, and h_k^{rest}; where $j = \{e,i\}$ and $k = \{e,i\}$; as well as $S^{\max}$ and the exponential $\exp(1)$. Here too we assume that the parameters depend on the postsynaptic neuron. For example, we define the neurotransmitter rate constants γ_{jk} with two subscripts. The first (j) defines the presynaptic neuron and the second (k) defines the postsynaptic neuron. Other researchers who investigate the dimensionless SPDEs model do not make this assumption [61]. We allow this parameter (as well as the parameters G_{jk}, N_{jk}^{β}, h_k^{rest}, and h_{jk}^{rev}) dependence on the postsynaptic neuron to explore more specific behavior in the model. We also assume that the cell resting potential h_k^{rest} depends only on the postsynaptic neuron k. A change in a dimensionless parameter can result from a change in any of the dimensional parameters of which it is comprised. For example, to decrease the dimensionless parameter Γ_{ee} and induce seizure-like oscillations in the model dynamics, we can: decrease G_{ee} or $S^{\max}$, or increase γ_{ee} or the difference $\mid h_{ee}^{\text{rev}} - h_e^{\text{rest}} \mid$. We list these dimensional quantities, their definitions, and the direction of change necessary to produce seizing dynamics in the model in Table 3.8. We include the parameters N_{ee}^{β}, N_{ei}^{β}, N_{ie}^{β}, and N_{ii}^{β} in this table, although these parameters are dimensionless.

We illustrate the changes in the dimensional quantities listed in Table 3.8 in Figure 3.37. We show in this figure a cartoon representation of the local connections between the two cell populations. (By local connections we mean connections established within a small spatial neighborhood, not long-range, corticocortical connections.) We draw the excitatory and inhibitory populations as rectangles on the left and right of Figure 3.37, respectively. The popu-

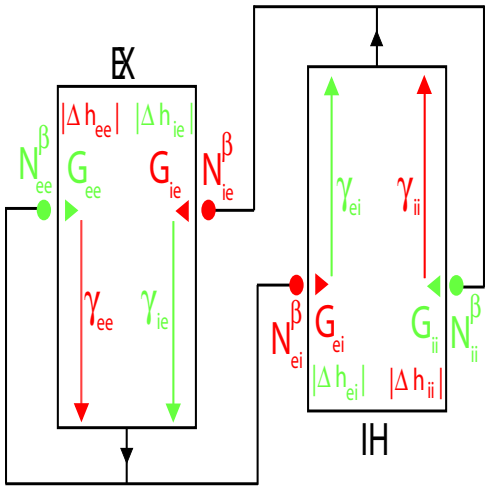

Figure 3.37: A cartoon of two interconnected neuronal populations (excitatory — EX — on the left and inhibitory — IH — on the right) and 16 physiological parameters. The filled circles denote synapses (N_{jk}^{β}), the colored triangles denote peak amplitudes of the postsynaptic potentials (G_{jk}), and the vertical colored arrows denote the rate constants (γ_{jk}). We also indicate the voltage difference between the reversal and resting potential by the label $|\,\Delta h_{jk}\,|$. To induce seizure-like oscillations in the model dynamics, we must either increase the red parameters or decrease the green parameters.

lations establish feedback and reciprocal synaptic connections. We draw these connections leaving the bottom of the excitatory population and the top of the inhibitory population. We illustrate the number and strength of the synapses formed by each connection with a filled circle labeled N_{jk}^{β} and a filled triangle labeled G_{jk}, respectively. Inside the rectangular label for each population we show the rate constants γ_{jk} with vertical arrows and the voltage differences $|\,h_{jk}^{\rm rev} - h_{k}^{\rm rest}\,| \equiv |\,\Delta h_{jk}\,|$ in text. The rate constants incorporate the time course of somatically recorded postsynaptic spike activity in a neuron due to the combined effects of passive dendritic cable delays and neurotransmitter kinetics, such as excitatory AMPA and inhibitory GABA [63]. The voltage differences scale the synaptic input by the reciprocal of the magnitude difference between the reversal and resting potentials. We color the labels for N_{jk}^{β}, G_{jk}, and γ_{jk}, and the text $|\,\Delta h_{jk}\,|$ to indicate changes in each quantity that result in seizing dynamics. To induce a seizure in the model dynamics we may increase the red-colored dimensional parameters or decrease the green-colored dimensional parameters.

3.8.1 Discussion

We suggest two methods for inducing seizure-like oscillations in the dimensionless ODEs. First, we may increase the (dimensionless) strength of connections between the excitatory and inhibitory cell populations (the inter-population connectivity.) We illustrate these connections in Figure 3.36 with red lines. Second, we may decrease the

(dimensionless) strength of connections within the excitatory cell population or within the inhibitory cell population (the intra-population connectivity.) We illustrate these connections with green lines in Figure 3.36. We conclude that strong interactions between the excitatory and inhibitory cell populations result in seizure-like oscillations in the model dynamics.

To allow an easier comparison of the model results with observational data, we define each dimensionless parameter in terms of its dimensional components. We list these definitions in the third column of Table 3.7. To allow more general types of connectivity than what we considered in Section 3.4 we assume that the parameters depend upon the postsynaptic cell population (i.e., the values differ for synapses terminating on an excitatory or inhibitory postsynaptic cell.) We illustrate the results for the dimensional parameters in Figure 3.37. We find that seizure-like oscillations can result from both increases (shown in red) or decreases (shown in green) in the model parameters. In words, to induce a seizure in the model dynamics, we may increase the number of synapses or the strength of each synapse from excitatory to inhibitory or inhibitory to excitatory populations. Or we may decrease the number of synapses or the strength of each synapse from excitatory to excitatory or inhibitory to inhibitory populations. Or we may increase the rate at which excitatory (inhibitory) input travels from dendrite to soma in excitatory (inhibitory) populations. Or we may decrease the rate at which excitatory (inhibitory) input travels from dendrite to soma in inhibitory (excitatory) populations. Or we may increase the difference between the reversal potential associated with excitatory synaptic activity on excitatory cells and the excitatory cell rest potential. Or we may increase the difference between the reversal potential associated with inhibitory synaptic activity on inhibitory cells and the inhibitory cell rest potential. Or we may decrease the difference between the reversal potential associated with excitatory synaptic activity on inhibitory cells and the inhibitory cell rest potential. Or we may decrease the difference between the reversal potential associated with inhibitory synaptic activity on excitatory cells and the excitatory cell rest potential. We summarize these results in Table 3.8.

To verify these model results one might perform the following experiment. First, choose the parameter of interest and identify a pharmacological agent to manipulate the parameter in cortex. For example, in [57] the authors associate increased propofol (an anesthetic) concentration with a reduction in the dimensional model parameter γ_i — the neurotransmitter rate constant. Then, administer the pharmacological agent to the subject (increasing the concentration with time, say) and record the resulting ECoG data. Finally, compare these observational data with the model results calculated for changing values of the parameter of interest.

Here we are interested in parameter changes that may result in a seizure. The experiment proposed above — administering a pharmacological agent to induce a seizure in a human subject — is risky. Instead, to gain what insight we can, we consider briefly what evidence already exists in the literature for the influence of pharmacological agents

or pathological mechanisms on seizure propagation. In doing so we shall attempt, perhaps naively and on purely theoretical grounds, to connect these agents or mechanisms with the foregoing discussion of our mathematical model. The value of such an undertaking at this early stage of model development is in clarifying thoughts about the action of agents or mechanisms and their relationship to our model. In what follows we compare the model predictions determined here with two pathological mechanisms thought to induce seizures: disinhibition and enhanced excitatory and inhibitory synaptic transmission.

In the disinhibition model, decreased inhibitory drive results in hyper-excitability of the tissue (for a critical review, see [106].) One mechanism by which disinhibition may result is known as the dormant basket cell hypothesis (dbch). In the dbch, seizures result from inactive inhibitory interneurons (e.g., basket cells in CA1 hippocampal slices from rat [107].) These inhibitory interneurons are not themselves impaired; instead, the inhibitory interneurons are disconnected from their excitatory afferents. Without excitation, the inhibitory interneurons become dormant and cease to inhibit excitatory neurons. An appropriate input to the resulting disinhibited (and thus hyper-excited) network induces a seizure.

Although our mathematical model describes cortical seizure propagation — *not* hippocampal seizure genesis — we compare the dbch with the model as an example and as a starting point. To relate the dbch and our model, we interpret the hypothesis to affect a model parameter: we associate the dormancy with a *decrease* in N_{ei}^{β} — the number of excitatory synapses received by inhibitory cells. Yet we have shown that an *increase* in N_{ei}^{β} (all else held constant) produces seizure-like oscillations in the model dynamics. Therefore we find that, when we interpret the dbch as a decrease in the parameter N_{ei}^{β}, the resulting dynamics of the dimensionless SPDEs do not seize.

We do not mean to suggest that the dbch is incorrect, just that it seems our model does not support the dbch as an explanation of cortical seizure propagation. This may be because the rules of hippocampal seizure genesis do not apply to cortical seizure propagation, and vice-versa. We have only shown that if we interpret the dbch as a decrease in N_{ei}^{β} the model dynamics exhibit no seizure-like oscillations. In determining this result, we have made two important assumptions about the dimensionless ODEs model. First, we set the parameter P_{ee} to 50 times its typical value (to "hyper-excite" the model cortex.) Second, we associate the dbch with a decrease in parameter N_{ei}^{β}. Of course, both assumptions may be incorrect. Moreover, the dimensionless ODEs model (and the complete dimensionless SPDEs model) provides only a crude approximation to the true dynamics of the seizing cortex. Although simple, we find the model useful in making our assumptions explicit.

As a second mechanism for the induction of seizures, we consider an enhancement of excitatory and inhibitory synaptic connections. To produce such an enhancement researchers administer the proconvulsant 4-aminopyridine (4-AP) to the tissue of interest. The effect of 4-AP is to enhance both excitatory and inhibitory synaptic transmission,

perhaps by enhanced neurotransmitter release at the presynaptic cells [108]. The result is an increased connectivity within the cell network. We relate these physiological changes to changes in the model parameters that increase the network connectivity, namely: an increase in G_{jk} — the mean peak amplitude of the postsynaptic potential induced by a presynaptic population j on postsynaptic population k — or N_{jk}^{β} — the number of local synapses from presynaptic population j to postsynaptic population k. We have found in model simulations that seizures result from increased inter-population connectivity (i.e., increases in G_{ei}, G_{ie}, N_{ei}^{β}, and N_{ie}^{β}) and decreased intra-population connectivity (i.e., decreases in G_{ee}, G_{ii}, N_{ee}^{β}, and N_{ii}^{β}.) This would be supported by the 4-AP model if 4-AP acts to increase inter-population connectivity more strongly than intra-population connectivity.

We again note the limitations of the model predictions. First, the model (although mathematically quite involved) provides only a crude approximation to the true dynamics of the seizing cortex. Second, we assume a 500% increase in the parameter P_{ee} (to "hyper-excite" the model cortex.) Third, we assume a relationship between pharmacological agent 4-AP and model parameters G_{jk} and N_{jk}^{β}. A more robust analysis may prove or disprove these relationships, and perhaps suggest new parameters required in the model.

We have shown in Section 3.8 how to induce seizure-like oscillations in the dimensionless ODEs and, in this subsection, how these model results compare to other proposed seizure mechanisms. We conclude by suggesting how the analysis in Section 3.8 applies to epilepsy treatments. We note that to *prevent* a seizure from occurring in the model dynamics, we may decrease the strength of the red connections (the inter-population connectivity) or increase the strength of the green connections (the intra-population connectivity) shown in Figure 3.36. These changes correspond to a decrease in the red (dimensional) parameters or an increase in the green (dimensional) parameters of Figure 3.37.

We find that changes in many dimensional parameters (G_{jk}, N_{jk}^{β}, γ_{jk}, h_{jk}^{rest}, and h_{jk}^{rest}) may prevent seizures in the model dynamics. This result may be useful in the development of antiseizure medications to which patients do not develop tolerances. For example, we might develop treatments that target different physiological parameters (and different pathways in Figure 3.37) so as not to exploit and perhaps desensitize any single pathway in particular.

To suggest how analysis of the dimensionless SPDEs model may relate to experimental results, we consider benzodiazepines (BZ). BZ are an important class of anticonvulsant drugs that act to enhance the action of GABA at GABA_{A} receptors. We follow [63] and assume that the effect of BZ are to increase the model parameters G_{ie} or G_{ii} — the mean peak IPSP induced on excitatory and inhibitory postsynaptic cells, respectively. We have shown in Section 3.8 that an increase of G_{ie} *induces* seizure-like oscillations in the model dynamics. The observed anticonvulsant effects of BZ would be consistent with the model if it acts to increase G_{ii} rather than G_{ie}. We again note that to determine this result we make important assumptions (e.g., a 500% increase in P_{ee}) about the crude mathematical model. Analysis of the relationships between anticonvulsant medications and model parameters may eventually suggest how these drugs

produce their therapeutic effects.

Symbol	Definition	Description
$\tilde{h}_{e,i}$	$h_{e,i}/h^{\text{rest}}$	Population mean soma dimensionless electric potential
$\tilde{I}_{ee,ie}$	$I_{ee,ie}\gamma_e/(G_e \exp(1) S^{\max})$	Total $e \to e$, $i \to e$ input to excitatory synapses
$\tilde{I}_{ei,ii}$	$I_{ei,ii}\gamma_i/(G_i \exp(1) S^{\max})$	Total $e \to i$, $i \to i$ input to inhibitory synapses
$\tilde{\phi}_{e,i}$	$\phi_{e,i}/S^{\max}$	Long range (corticocortical) input to e,i populations
$\tilde{t}$	t/τ	Dimensionless time
$\tilde{x}$	$x/(\tau\tilde{v})$	Dimensionless space

Table 3.3: Dynamical variable definitions for the dimensionless SPDEs neural macrocolumn model. The dimensionless variables (left column) are defined in terms of the dimensional symbols (middle column) found in Table 1 of [61]. The variables are described in the right column. Subscripts e and i refer to excitatory and inhibitory.

Symbol	Definition	Description	Typical Value
e, i		(As subscript) excitatory, inhibitory cell populations	
$\Gamma_{e,i}$	$\frac{G_{e,i}\exp(1)S^{\max}}{\gamma_{e,i}\lvert h^{\rm rev}_{e,i}-h^{\rm rest}\rvert}$	Influence of input on the mean soma membrane values	1.42×10^{-3}, 0.0774
$h^0_{e,i}$	$h^{\rm rev}_{e,i}/h^{\rm rest}$	Dimensionless cell reversal potential	-0.643, 1.29
$T_{e,i}$	$\tau\gamma_{e,i}$	Dimensionless neurotransmitter rate constant	12.0, 2.6
$\lambda_{e,i}$	$\tau\tilde{v}\Lambda_{ee,ei}$	Dimensionless characteristic corticocortical inverse-length scale	11.2, 18.2
$P_{ee,ie}$	$p_{ee,ie}/S^{\max}$	Subcortical input to e population	11.0, 16.0
$P_{ei,ii}$	$p_{ei,ii}/S^{\max}$	Subcortical input to i population	16.0, 11.0
$N^{\alpha}_{e,i}$	—	Total number of synaptic connections from distant e populations	4000, 2000
$N^{\beta}_{e,i}$	—	Total number of local e and i synaptic connections	3034, 536
$\tilde{g}_{e,i}$	$g_{e,i}h^{\rm rest}$	Dimensionless sigmoid slope at inflection point	-19.6, -9.8
$\tilde{\theta}_{e,i}$	$\theta_{e,i}/h^{\rm rest}$	Dimensionless inflection-point for sigmoid function	0.857, 0.857

Table 3.4: Parameter values for the dimensionless SPDEs neural macrocolumn model. The dimensionless symbols (first column) are defined in terms of the dimensional variables (second column) found in Table 1 of [61]. The variables are described in the third column and typical values are shown in the fourth column.

Table 3.5: The results for f_0 and the magnitude of v (in I1 and I2) averaged over the electrodes considered for each subject (i.e., two electrodes for Subject 1, three electrodes for Subject 2, and nine electrodes for Subject 3 and Subject 4.) We label the average quantities $< f_0 >$ and $< |v| >$. To compute the uncertainty in the average, we assume the uncertainties in f_0 for each seizure are independent and random and propagate the uncertainties in the standard way.

Subject	$< f_0 >$ [Hz]	$<\mid v \mid>$ in $I1$	$<\mid v \mid>$ in $I2$
1	4.5 ± 0.1	0.5 ± 0.1	3 ± 1
2	7.1 ± 0.4	4 ± 12	2.6 ± 0.9
3	8.76 ± 0.05	2 ± 2	1.2 ± 0.4
4	8.1 ± 0.1	2.6 ± 3	4 ± 4

Table 3.6: The peak frequency f_0 and wave speed v determined for the model solutions of h_e.

Simulation	f_0	v
ODE (Figure 3.12(b))	7.5 Hz	—
PDE (Figure 3.17(b))	$\sim$ 12.0 Hz	$\sim$ 3.0 m/s
PDE (Figure 3.22)	7.5 Hz	1.2 m/s

OLD	NEW	DIMS	DEFINITION	TYPICAL	Δ
Γ_e	Γ_{ee}	$\frac{G_{ee}\exp(1)S^{\max}}{\gamma_{ee}\lvert h_{ee}^{\text{rev}}-h_e^{\text{rest}}\rvert}$	influence of **excitatory** input on the mean soma membrane values of **excitatory** neurons	1.42×10^{-3}	-12%
	Γ_{ei}	$\frac{G_{ei}\exp(1)S^{\max}}{\gamma_{ei}\lvert h_{ei}^{\text{rev}}-h_i^{\text{rest}}\rvert}$	influence of **excitatory** input on the mean soma membrane values of **inhibitory** neurons	1.42×10^{-3}	$+28\%$
Γ_i	Γ_{ie}	$\frac{G_{ie}\exp(1)S^{\max}}{\gamma_{ie}\lvert h_{ie}^{\text{rev}}-h_e^{\text{rest}}\rvert}$	influence of **inhibitory** input on the mean soma membrane values of **excitatory** neurons	0.0774	$+14\%$
	Γ_{ii}	$\frac{G_{ii}\exp(1)S^{\max}}{\gamma_{ii}\lvert h_{ii}^{\text{rev}}-h_i^{\text{rest}}\rvert}$	influence of **inhibitory** input on the mean soma membrane value of **inhibitory** neurons	0.0774	-22%
N_e^β	N_{ee}^β	—	number of local **excitatory** synapses on **excitatory** neurons	3034	-28%
	N_{ei}^β	—	number of local **excitatory** synapses on **inhibitory** neurons	3034	$+39\%$
N_i^β	N_{ie}^β	—	number of local **inhibitory** synapses on **excitatory** neurons	536	$+12\%$
	N_{ii}^β	—	number of local **inhibitory** synapses on **inhibitory** neurons	536	-19%

Table 3.7: Definitions of dimensionless parameters effecting connectivity between excitatory and inhibitory neural populations in the dimensionless ODEs. The original parameters in the first column are listed in Table 3.4. We list the symbols for the new parameters in the second column and define these parameters in terms of dimensional components from [61], and in words in the third and fourth columns, respectively. We write the typical value in the fifth column, and the percentage change in the typical parameter value necessary to induce seizure-like oscillations in the hyper-excited model cortex (i.e., $P_{ee} = 548.066$) in the last column.

PARAMETER	DEFINITION	Δ FOR SEIZURE
$G_{ei,ie}$	mean peak amplitude of the PSP induced by a single presynaptic spike from an (excitatory, inhibitory) neuron at the synapses of an (inhibitory, excitatory) postsynaptic neuron	↑
$G_{ee,ii}$	mean peak amplitude of the PSP induced by a single presynaptic spike from an (excitatory, inhibitory) neuron at the synapses of an (excitatory, inhibitory) postsynaptic neuron	↓
$N^{\beta}_{ei,ie}$	the number of local (excitatory, inhibitory) synapses on (inhibitory, excitatory) neurons	↑
$N^{\beta}_{ee,ii}$	the number of local (excitatory, inhibitory) synapses on (excitatory, inhibitory) neurons	↓
$\gamma_{ee,ii}$	the neurotransmitter rate constant for (EPSPs, IPSPs) to travel from the dendrites to the soma of an (excitatory, inhibitory) neuron	↑
$\gamma_{ei,ie}$	the neurotransmitter rate constant for (EPSPs, IPSPs) to travel from the dendrites to the soma of an (inhibitory, excitatory) neuron	↓
$\lvert h^{rev}_{ee,ii} - h^{rest}_{e,i} \rvert$	the difference between the reversal potential associated with (excitatory, inhibitory) synaptic activity on (excitatory, inhibitory) cells and the (excitatory, inhibitory) cell rest potential	↑
$\lvert h^{rev}_{ei,ie} - h^{rest}_{i,e} \rvert$	the difference between the reversal potential associated with excitatory, inhibitory) synaptic activity on (inhibitory, excitatory) cells and the (inhibitory, excitatory) cell rest potential	↓
S^{max}	the maximum value of the sigmoid transfer function that maps the soma voltage to average output spike rate	↑↓

Table 3.8: Definitions of dimensional parameters affecting connectivity between excitatory and inhibitory neural populations in the dimensionless ODEs. We define each parameter in words in the second column. We indicate the direction of change in each parameter necessary to induce seizure-like oscillations in the hyper-excited model cortex (i.e., $P_{ee} = 548.066$) in the last column. Here PSP stands for postsynaptic potential, EPSP for excitatory postsynaptic potential, and IPSP for inhibitory postsynaptic potential.

Chapter 4

Conclusion

We undertook two objectives in this thesis. First, in Chapter 2 we defined seven measures of interdependence between two time series and applied each measure to simulated data computed from the coupled Henon map and coupled Rössler oscillators in Sections 2.2 and 2.3, and to simulated data that consisted of bursts of oscillatory activity in Section 2.4. We showed that of the seven measures only $T(x|y)$ captured the appropriate coupled (and uncoupled) behavior in each case. In Section 2.5 we applied $T(x|y)$ to ECoG data recorded from three electrodes in an auditory ERP experiment, and in Section 2.6 we applied three other synchronization measures to resting EEG data collected from healthy, MCI, and AD patients.

Second, in Chapter 3 we studied a mathematical model of human cortical electrical activity recorded during seizure. We started with an analysis of ictal ECoG data collected from four human subjects, and determined two quantities of interest: f — the average frequency of maximum power during seizure, and v — the speed of voltage propagation across the cortex during seizure. We then stated a dimensionless form of a mean field model of cortical electrical activity and explored how changes in two model parameters (P_{ee} and Γ_e) affected the model dynamics. Through bifurcation analysis and numerical simulations, we showed a quantitative agreement between f and v computed from the mathematical model and observed in the ECoG data. We concluded that the mean field model, with appropriate values of P_{ee} and Γ_e, provided a crude approximation to the seizing cortex. Having shown this agreement, we then used the model to investigate methods to abort seizures in the cortex. We considered how two types of applied electric fields affected the model dynamics through changes in bifurcations. Of the two, only the differential controller could abort the seizure-like oscillation in the model dynamics with minimal negative consequences. Finally, we sought to connect the "seizing" mathematical model to cortical physiology. We identified changes in eight parameters

that resulted in seizure-like oscillations in the model dynamics. We found that increased inter-population connectivity ($e \to i$ and $i \to e$) and decreased intra-population connectivity ($e \to e$ and $i \to i$) induced seizures in the model. We then related these parameter changes to corresponding changes in cortical physiology. We concluded by comparing these results with other seizure models, and suggesting new types of medications to treat epilepsy.

We have achieved three important results. First, we introduced a new measure of synchronization in Section 2.1. We showed that this measure is more appropriate for the analysis of an ensemble of data compared to other synchronization and traditional linear measures. We then applied this measure to an ensemble of ECoG data recorded during an ERP experiment and suggested how three cortical regions may communicate. Second, we applied three well known synchronization measures to scalp EEG data recorded from three subject groups: healthy, MCI, and AD. Unlike other approaches, we did not filter the EEG data into arbitrary frequency bands (e.g., α and β.) We showed that of the five interhemispheric synchronization measures we considered, only that between the left and right occipital lobes provided a statistically significant discriminant between the healthy and AD subjects. We then suggested that AD affects coupling between the occipital lobes more strongly than between other interhemispheric regions.

We cannot verify these physiological interpretations of the synchronization results; we can only hypothesize that changes in the synchronization of EEG (or ECoG) data result from changes in cortical physiology. To test these hypotheses would require invasive, destructive procedures. Therefore, to connect the analysis of ECoG and EEG time series to changes in cortical physiology, we implement a mathematical model of human cortical electrical activity. At present such models can only approximate cortical electrical activity in states of pathological order. The final accomplishment in this dissertation was to show that a mathematical model of human cortical electrical activity in current use can approximate the seizing cortex. Having established the validity of the model, we used it to suggest new methods to abort seizures and treat epilepsy.

As measures and models of cortical electrical activity improve, the need for invasive, destructive neurological procedures may lessen. For example, to treat epilepsy future physicians might apply a suite of coupling measures to the patient's scalp EEG. They may then compare these coupling results with computer simulations of a detailed cortical model (based, perhaps, on the patient's own cortex.) This comparison could reveal the physiological changes (i.e., parameter changes in the model) associated with the patient's epilepsy and suggest specific, localized methods of treatment. This treatment may be chemical (e.g., a drug designed to counter the patient's physiological pathology) or electrical (e.g., a small stimulator placed near the patient's epileptogenic zone.) Further refinements may permit more researchers to apply mathematical models to their studies of the healthy human cortex. For example, psychologists may attempt to relate the results of an ERP experiment to the physiological source.

In the future improved measures and models will replace those discussed here. For example, an important new

measure of coupling — Granger causality — may help determine causal relationships between two EEG or ECoG time series [109]. Often these measures develop in disparate fields; the original application of Granger causality was for the analysis of financial time series. In a similar way, techniques developed to analyze and model EEG or ECoG data may find other applications; the study of detailed mathematical models of cortical activity may suggest new analysis techniques. As researchers acquire more experimental data and computing power they will develop more accurate mathematical models of human cortical electrical activity. Perhaps, in the future, these models will simulate the electrical activity of each individual neuron [11].

Bibliography

[1] J. Nolte, *The human brain : an introduction to its functional anatomy* (Mosby, St. Louis, Mo, 2002).

[2] R. D. Traub, I. Pais, A. Bibbig, F. E. N. LeBeau, E. H. Buhl, H. Garner, H. Monyer, and M. A. Whittington, J. Neurophysiol **94**, 1225 (2005).

[3] P. L. Nunez, *Neocortical Dynamics and human EEG rhythms* (Oxford University Press, New York, 1995).

[4] V. Mountcastle, Brain **120**, 701 (1997).

[5] W. Singer, Annu. Rev. Physiol **55**, 349 (1993).

[6] E. Edwards, M. Soltani, L. Y. Deouell, M. S. Berger, and R. T. Knight, J. Neurophys (In press).

[7] A. Bruns, J Neurosci Methods **137**, 321 (2004).

[8] R. N. Bracewell, *The Fourier Transform and its Applications* (McGraw Hill, Boston, 2000).

[9] R. D. Traub, R. K. Wong, R. Miles, and H. Michelson, J Neurophysiol **66**, 635 (1991).

[10] S. Murakami, T. Zhang, A. Hirose, and Y. C. Okada, J Physiol-London **544**, 237 (2002).

[11] R. B. Traub, D. Contreras, M. O. Cunningham, H. Murray, F. E. N. LeBeau, A. R. A, A. Bibbig, W. B. Wilent, M. J. Higley, and M. A. Whittington, J. Neurophysiol **93**, 2194 (2005).

[12] W. J. Freeman, Exp. Neurol. **10**, 525 (1964).

[13] H. R. Wilson and J. D. Cowan, Biophys. J. **12**, 1 (1972).

[14] A. von Stein, C. Chaing, and P. Konig, Proc. Natl. Acad. Sci. **97**, 14748 (2000).

[15] P. L. Nunez, R. Srinivasan, A. Westdorp, E. Wijesinghe, D. M. Tucker, R. B. Silberstein, and P. Cadusch, Electroenceph. clin. Neurophysiol. **103**, 499 (1997).

[16] A. von Stein and J. Sarnthein, Int. J. Psychophysiol. **38**, 301 (2000).

[17] J. S. Bendat and A. G. Piersol, *Random Data: Analysis and Measurement Procedures, Second Edition* (J. Wiley & Sons, New York, 1986).

[18] L. M. Pecora and T. L. Carroll, Phys. Rev. Lett. **64**, 821 (1990).

[19] N. Rulkov, M. Sushchik, L. Tsimring, and H. Abarbanel, Phys. Rev. E **51**, 980 (1995).

[20] M. G. Rosenblum, A. S. Pikovsky, and J. Kurths, Phys. Rev. Lett. **76**, 1804 (1996).

[21] J. Arnhold, P. Grassberger, K. Lehnertz, and C. Elger, Physica D **134**, 419 (1999).

[22] J. Bhattacharya, E. Pereda, and H. Petsche, IEEE Trans. Sys. Man. Cyb. B **33**, 85 (2003).

[23] R. M. Gulrajani, *Bioelectricity and Biomagnetism* (J. Wiley, New York, 1998).

[24] T. Schreiber, Phys Report **308**, 1 (1999).

[25] A. Delorme and S. Makeig, J. Neurosci. Meth. (in press).

[26] H. Abarbanel, R. Brown, J.Sidorowich, and L. Tsimring, Rev. Mod. Phys. **65**, 1331 (1993).

[27] T. Schreiber, Phys. Reports **308**, 1 (1999).

[28] R. Q. Quiroga, A. Kraskov, T. Kreuz, and P. Grassberger, Phys. Rev. E **65**, 041903 (2002).

[29] R. Q. Quiroga, J. Arnhold, and P. Grassberger, Phys. Rev. E **61**, 5142 (2000).

[30] M. Breakspear, Hum Brain Mapp **15**, 175 (2002).

[31] A. Wolf, J. B. Swift, H. L. Swinney, and J. A. Vastano, Physica D **16**, 285 (1985).

[32] A. N. Pavlov, O. V. Sosnovtseva, A. R. Ziganshin, N. H. Holstein-Rathlou, and E. Mosekilde, Physica A **316**, 233 (2002).

[33] K. J. Friston, Neuroimage **5**, 213 (1997).

[34] M. A. Kramer, E. Edwards, M. Soltani, M. S. Berger, R. T. Knight, and A. J. Szeri, Phys Rev E **70**, 011914 (2004).

[35] Statistics about Alzheimer's disease, 2005.

[36] D. S. Knopman, B. F. Boeve, and R. C. Petersen, Mayo Clin Proc **78**, 1290 (2003).

[37] R. L. Ernst and J. W. Hay, American Journal of Public Health **84**, 1261 (1994).

[38] R. P. Brenner, C. F. Reynolds, and R. F. Ulrich, Electroencephalogr Clin Neurophysiol **69**, 110 (1988).

[39] U. Schreiter-Gasser, T. Gasser, and P. Ziegler, Electroencephalogr Clin Neurophysiol **86**, 15 (1993).

[40] V. Jelic, P. Julin, M. Shigeta, A. Nordberg, L. Lannfelt, B. Winblad, and L. O. Wahlund, J Neurol Neurosurg Psychiatry **63**, 59 (1997).

[41] C. Besthorn, H. Sattel, C. Geiger-Kabisch, R. Zerfass, and H. Forstl, Electroencephalogr Clin Neurophysiol **95**, 84 (1995).

[42] W. S. Pritchard, D. W. Duke, K. L. Coburn, N. C. Moore, K. A. Tucker, M. W. Jann, and R. M. Hostetler, Electroencephalogr Clin Neurophysiol **91**, 118 (1994).

[43] K. O'Connor, J. C. Shaw, and C. O. Ongley, Br J Psychiatry **135**, 156 (1979).

[44] C. Besthorn, H. Forstl, C. Geiger-Kabisch, H. Sattel, T. Gasser, and U. Schreiter-Gasser, Electroencephalogr Clin Neurophysiol **90**, 242 (1994).

[45] G. Adler, S. Brassen, and A. Jajcevic, J. Neural Trans **110**, 1015 (2003).

[46] C. J. Stam, Y. van der Made, Y. A. L. Pijnenburg, and P. Scheltens, Acta Neurologica Scandinavica **2**, 90 (2003).

[47] W. J. Freeman, Int. J. of Bif. and Chaos **2**, 451 (1992).

[48] M. A. Kramer, H. E. Kirsch, and A. J. Szeri, J. R. Soc. Interface **2**, 113 (2005).

[49] M. A. Kramer, A. J. Szeri, and H. E. Kirsch, In preparation (2005).

[50] M. A. Kramer, B. A. Lopour, H. E. Kirsch, and A. J. Szeri, Submitted (2005).

[51] M. A. Dichter and G. F. Ayala, Science **237**, 157 (1987).

[52] D. J. Pinto and G. B. Ermentrout, SIAM J. App. Math **62**, 206 (2001).

[53] B. W. Connors and Y. Amitai, in *Epilepsy: Models, Mechanisms, and Concepts*, edited by P. A. Schwartkroin (Cambridge University Press, Cambridge, UK, 1993), p. 388.

[54] R. D. Chervin, P. A. Pierce, and B. W. Connors, J. Neurophysiol **60**, 1695 (1988).

[55] W. Singer and C. M. Gray, Annu. Rev. Neurosci **18**, 555 (1995).

[56] A. Bragin, I. Mody, C. L. Wilson, and J. E. Jr., J Neurosci **22**, 2012 (2002).

[57] M. L. Steyn-Ross, D. A. Steyn-Ross, J. W. Sleigh, and D. T. J. Liley, Phys. Rev. E **60**, 7299 (1999).

[58] D. T. J. Liley, P. J. Cadusch, and J. J. Wright, Neurocomputing **26-27**, 795 (1999).

[59] M. L. Steyn-Ross, D. A. Steyn-Ross, J. W. Sleigh, and L. C. Wilcocks, Phys. Rev. E **64**, 011917 (2001).

[60] D. A. Steyn-Ross, M. L. Steyn-Ross, L. C. Wilcocks, and J. W. Sleigh, Phys. Rev. E **64**, 011918 (2001).

[61] M. L. Steyn-Ross, D. A. Steyn-Ross, J. W. Sleigh, and D. R. Whiting, Phys. Rev. E **68**, 021902 (2003).

[62] I. Bojak and D. T. J. Liley, Phys Rev E **71**, 041902 (2005).

[63] D. T. J. Liley, P. J. Cadusch, and M. P. Dafilis, Network: Comput. Neural Syst. **13**, 67 (2002).

[64] W. J. Freeman, *Mass Action in the Nervous System* (Academic Press, New York, 1975).

[65] V. K. Jirsa and H. Haken, Phys. Rev. Lett. **77**, 960 (1996).

[66] P. A. Robinson, C. J. Rennie, and J. J. Wright, Phys. Rev. E **56**, 826 (1997).

[67] *Neocortical dynamics and human EEG rhythms*, edited by P. L. Nunez (Oxford University Press, New York, 1995).

[68] E. Doedel, R. Paffenroth, A. Champneys, T. Fairgrieve, Y. A. Kuznetsov, B. Sandstede, and X.Wang, AUTO 2000: Continuation and bifurcation software for ordinary differential equations (with HomCont), http://sourceforge.net/projects/auto2000/, 2000.

[69] *Electroencephalography: Basic Principles, Clinical Applications, and Related Fields*, edited by E. Niedermeyer and F. L. DaSilva (Lippincott Williams and Wilkins, New York, 1999).

[70] J. S. Ebersole and S. V. Pacia, Epilepsia **37**, 386 (1996).

[71] S. S. Spencer, P. Guimaraes, A. Katz, J. Kim, and D. Spencer, Epilepsia **33**, 537 (1992).

[72] K. Morimoto, M. Fahnestock, and R. J. Racine, Prog Neurobiol. **73**, 1 (2004).

[73] R. D. Traub, M. A. Whittington, E. H. Buhl, A. B. F. E. N. LeBeau, S. Boyd, H. Cross, and T. Baldeweg, Epilepsia **42**, 153 (2001).

[74] W. J. Freeman, Int. J. Bifurcat. Chaos **2**, 451 (1992).

[75] F. L. da Silva, W. Blanes, S. N. Kalitzin, J. Parra, P. Suffczynski, and D. N. Velis, Epilepsia **44**, 72 (2003).

[76] E. M. Izhikevich, SIAM Review **43**, 315 (2001).

[77] *Introduction to applied nonlinear dynamical systems and chaos*, edited by S. Wiggins (Springer, New York, 2003).

[78] D. J. Higham, SIAM Review **43**, 525 (2001).

[79] M. C. Cross and P. C. Hohenberg, Rev. Mod. Phys **65**, 851 (1993).

[80] E. Knobloch, Phys Rev A **34**, 1538 (1989).

[81] A. D. Wit, D. Lima, G. Dewel, and P. Borckmans, Phys. Rev. E **54**, 261 (1996).

[82] L. Yang, M. Dolnik, A. M. Zhabotinsky, and I. R. Epstein, J. Chem. Phys. **117**, 7259 (2002).

[83] V. K. Jirsa and J. A. S. Kelso, Phys. Rev. E **62**, 8462 (2000).

[84] P. A. Robinson, C. J. Rennie, and D. L. Rowe, Phys. Rev. E **65**, 041924 (2002).

[85] Epilepsy: An Introduction, 2005.

[86] R. P. Lesser, S. H. Kim, L. Beyderman, D. L. Miglioretti, W. R. S. Webber, M. Bare, B. Cysyk, G. Krauss, and B. Gordon, Neurology **53**, 2073 (1999).

[87] G. K. Motamedi, R. P. Lesser, D. L. Miglioretti, Y. Mizuno-Matsumoto, B. Gordon, W. R. S. Webber, D. C. Jackson, J. P. Sepkuty, and N. E. Crone, Epilepsia **43**, 836 (2002).

[88] E. H. Kossoff, E. K. Ritzl, J. M. Politsky, A. M. Murro, J. R. Smith, R. B. Duckrow, D. D. Spencer, and G. K. Bergey, Epilepsia **45**, 1560 (2004).

[89] M. Kinoshita, A. Ikeda, R. Matsumoto, T. Begum, K. Usui, J. Yamamoto, M. Matsuhashi, M. Takayama, N. Mikuni, J. Takahashi, S. Miyamoto, and H. Shibasaki, Epliepsia **45**, 787 (2004).

[90] S. A. Chkhenkeli, M. Sramka, G. S. Lortkipanidze, T. N. Rakviashvili, E. S. Bregvadze, G. E. Magalashvili, T. S. Gagoshidze, and I. S. Chkhenkeli, Clin Neurol Neurosurg **106**, 318 (2004).

[91] B. J. Gluckman, E. J. Neel, T. I. Netoff, W. L. Ditto, M. L. Spano, and S. J. Schiff, J Neurophysiol **76**, 4202 (1996).

[92] B. J. Gluckman, H. Nguyen, S. L. Weinstein, and S. J. Schiff, J Neurosci **21**, 590 (2001).

[93] P. A. Tass, Prog Theor Phys Supp **139**, 301 (2000).

[94] M. Rosenblum and A. Pikovsky, Phys. Rev. E **70**, 041904 (2004).

[95] G. Chen, J. L. Moiola, and H. O. Wang, Internat. J. Bifur. Chaos **10**, 511 (2000).

[96] C. Y. Chan and C. Nicholson, J. Physiol **371**, 89 (1986).

[97] D. Tranchina and C. Nicholson, Biophys J **50**, 1139 (1986).

[98] M. Golubisky and W. F. Langford, J Diff Eq **41**, 375 (1980).

[99] W. F. Agnew, D. B. McCreery, T. G. H. Yuen, and L. A. Bullara, in *Neural Prostheses: Fundamental Studies*, edited by W. F. Agnew and D. B. McCreery (Prentice Hall, Englewood Cliffs, New Jersey, 1990), Chap. 9, pp. 226–252.

[100] K. Engelborghs, T. Luzyanina, and G. Samaey, Technical Report TW-330 (2001).

[101] M. L. V. Quyen, V. Navarro, J. Martinerie, M. Baulac, and F. J. Varela, Epilepsia **44**, 30 (2003).

[102] K. K. Jerger, S. L. Weinstein, T. Sauer, and S. J. Schiff, Clin Neurophysiol **116**, 545 (2005).

[103] T. C. Ferree and M. T. Clay, IEEE Trans Biomed Eng **21**, 629 (2002).

[104] B. Gordon, R. P. Lesser, N. E. Rance, J. H. Jr, R. Webber, S. Uematsu, and R. S. Fisher, Electroencephalogr Clin Neurophysiol **75**, 371 (1990).

[105] S. S. Nathan, S. R. Sinha, B. Gordon, R. P. Lesser, and N. V. Thakor, Electroencephalogr Clin Neurophysiol **86**, 183 (1993).

[106] C. Bernard, M. Esclapez, J. Hirsch, and Y. Ben-Ari, Epilepsy Res **32**, 93 (1998).

[107] J. W. Bekenstein and E. W. Lothman, Science **259**, 97 (1993).

[108] P. A. Rutecki, F. J. Lebeda, and D. Johnston, J Neurophysiol **57**, 1911 (1987).

[109] M. Kaminski, M. Ding, W. A. Truccolo, and S. L. Bressler, Biol Cybern **85**, 145 (2001).